Title

Data Optimization for Identification of Lithium Ion Battery Electrochemical Parameters

Author

Lai, Qingzhi

Publication Date

2021

Data Optimization for Identification of Lithium Ion Battery Electrochemical Parameters

By

QINGZHI LAI
DISSERTATION

Submitted in partial satisfaction of the requirements for the degree of

DOCTOR OF PHILOSOPHY

in

Mechanical and Aerospace Engineering

in the

OFFICE OF GRADUATE STUDIES

of the

UNIVERSITY OF CALIFORNIA

DAVIS

Approved:

Xinfan Lin, Chair

Jae Wan Park

Scott Moura

Committee in Charge

2022

Abstract

Estimation of model parameters is a critical topic in battery modeling research, as the accuracy of parameters determines the efficacy of the widely used model-based battery engineering. The measurement-based approaches aim at measuring the battery physical parameters using advanced experiment and instrumentation techniques, but the associated complexity, time, and cost make it undesirable in many cases. Therefore, the data-based identification approach, which only uses easily available input and output measurement data, has been widely adopted due to its convenience and noninvasiveness. As the quality of data has significant impact on the estimation accuracy, data optimization, or optimal experiment design, is often utilized to improve and guarantee the accuracy of estimation. The common practice of data optimization aims at designing input excitation by maximizing a certain conventional criterion, e.g. Fisher information which measures the information content of the data and relates to the variance of the estimation error. However, such approach suffers from fundamental limitations, including inability to explicitly address estimation bias and system uncertainties in measurement, model, and parameter, which severely restrict the applicability and effectiveness of the method in practice.

To overcome the existing limitations, new criteria and a novel framework are proposed in this dissertation for estimation error quantification and data optimization. A generic formula is first derived for quantifying the estimation error subject to sensor, model, and parameter uncertainties for the commonly used least-squares algorithm. Based on the formula, data structures, represented in terms of parameter sensitivity, which could minimize the estimation errors caused by each type of uncertainty are identified. These data structures are then employed as new criteria to supplement the Fisher information and formulate a novel data optimization framework. In order to facilitate the solution of the formulated data optimization problem, this dissertation also explores new methods for efficient computation of parameter sensitivity, which is a key for representing the data structures and enabling data optimization. Efforts have been made to derive the analytic expressions of the sensitivity of battery electrochemical parameters by leveraging reasonable assumptions and model reformulation and simplification techniques. The proposed methodology is applied to estimating the electrochemical parameters of a single particle lithium-ion battery model in simulation and experiments, showing excellent estimation and voltage prediction accuracy compared with the traditional approach.

To all those who believed in me.

Contents

List of Figures

List of Tables

ACKNOWLEDGMENTS

I would like to express my great appreciation to my advisor Professor Xinfan Lin for his great help, guidance, and financial support throughout my Ph.D. degree, without which this work might not have been completed. His abilities to learn new and many things along with his time management skills have inspired me throughout the course of the completion of this work. He has been helping me improve in all aspects. It has been quite a learning experience working with him.

I also would like to thank fellow graduate students at Professor Lin's research lab, including Sidharth Jangra, Jackson Blake, Rui Huang, Vincent Chung, Mengzhu Gao, Nicolas Michel, Anish Kumar Sinha, Jonathan Dorsey and Russell Hawkins. It was a pleasure working with you all and learning from your skills and abilities. I wish to acknowledge the help and guidance from my dissertation committee members. The assistance provided by Professor Jae Won Park and Associate Professor Scott Moura is significant in finishing this work. My special thanks are extended to the LG Energy Solution company and its employees, namely Dr. Won Tae Joe, Dr. Hyoung Jun Ahn, Mr. Geumbee Kim, Mr. YoungJin Kim and others, for all the financial and technical support for my research. I also wish to thank all my friends for all wonderful experience and memories.

Finally, I would like to greatly thank my parents Sihong Lai and Aisheng Ruan for their endless support and love, my wife Na Ma for her encouragement to pursue the doctoral degree and help, and my sisters Shuyu Lai and Nengmei Lai for their constant help.

Chapter 1

Introduction

Lithium-ion battery is an electrochemical energy storage device with high energy and power density, long lifetime, and minimal self-discharge rate among many other advantages [1, 2, 3], and has hence been widely used in many applications including consumer electronics and electrified transportation [4, 5, 6, 3]. To guarantee and improve the safety and performance of batteries, model-based simulation, design, estimation, diagnostics, and management have been studied extensively to understand the underlying physical dynamics and optimize battery behavior [7, 8]. Identification/estimation of model parameters is a critical topic in modeling research, as the accuracy of parameters determines the fidelity of the model and the efficacy of model-based battery engineering [9, 10]. Estimation is challenging, especially for models with complicated structure and a large parameter set, e.g. the electrochemical first principle models [11, 12, 13, 14].

1.1 Background of parameter identification for Li-ion battery

Existing methods for parameter estimation can be categorized as measurement-based approaches and data-based system identification approaches, both of which are extensively studied [15, 16, 17]. The measurement-based approaches aim at measuring the battery physical parameters using advanced experiment and instrumentation techniques. For example, the galvanostatic intermittent titration technique (GITT) can be used to measure the open circuit potential of battery electrodes in either half cell or three-electrode full cell configurations to determine the solid-phase diffusivity [18]. Scanning electron microscope (SEM) can be utilized to analyze the average electrode particle size using image analysis software such as ImageJ. X-ray spectroscopy can be used to analyse elemental constituents of the active material [19]. Focused ion beam milling with SEM can be used to investigate the porous microstructure and determine porosity [20]. Recently, a comprehensive study was presented in [15], which managed to use the collection of above techniques to determine the parameter set of a full-order battery electrochemical model, i.e. the pseudo-2D (P2D) Doyle-Fuller-Newman (DFN) model. However, such approach suffers from major drawbacks as it involves advanced equipment, destructive and invasive procedures (e.g. post-mortem analysis), specialized skills, and lengthy data analysis process. The associated complexity, time, and cost often make it unaffordable or undesirable in many circumstances. In addition, the fidelity of the model obtained in this way may still not be satisfactory in practice. For example, some parameters need to be treated as input (current)-dependent and hand tuned in order to make the model prediction match with the experimental data over a range of input current magnitude [15].

The data-based approaches, on the other hand, seek to determine the parameter values using system identification techniques. The basic procedure is to find the parameter values that best fit an input-output dataset, e.g. current and voltage, using a certain algorithm [21, 22, 23]. This approach is widely adopted in many research due to its convenience [24, 25, 26], as the input and output data can be easily measured in a non-invasive manner without specialized equipment and procedures. Most existing works proposed to use data generated by heuristic/empirical input sequences for estimation, e.g. constant current [27, 28], pulses [21, 29], sinusoidal current [30], and dynamic drive cycles [11, 31]. While these data may work well for battery models with simple structure and few parameters, e.g. the equivalent circuit model [32, 33, 34], they may not contain sufficient information, measured by parameter sensitivity or the Fisher information metric, about the parameters to be estimated and yield adequate accuracy for more complicated electrochemical models [11, 16, 35]. As the quality of data plays an important role in determining the accuracy of the estimation results[36, 37, 35], efforts have been made to enhance the quality of data used for estimation. For example, some recent works have started exploring design or selection of the input excitation profile to increase the (Fisher) information content of the data and hence improve the estimation accuracy [30, 16].

1.2 Challenges in current research

Despite significant progress and promising outcomes, there are still several major obstacles that remain to be addressed, which are all related to the data (input excitation) used for estimation.

First, the data are not yet fully optimized with respect to the conventional criterion. Most existing works focused on optimizing the input excitation subject to certain imposed patterns. For example, in [30], the double-sinusoidal current pattern is considered, and the coefficients of the sine wave, including the frequency, amplitude, and phase angle, are optimized; In [38], the Constant Current (CC)-Constant Voltage (CV) profile is optimized in terms of the current and voltage limits; In [16], combinations of current patterns from a pre-defined library, including pulses, sine waves, and drive cycles, are selected to formulate the optimal profile. The profile obtained in this manner, however, is only optimal within the specific pattern considered, but not necessarily the ultimate global optimum. It is of great interest to find the ultimate optimal profile not subject to any pre-set pattern, and explore the fundamental signatures/features of the optimal data for estimating different parameters. The main difficulty of direct optimization lies in the complexity of computing the sensitivity and the sensitivity-based metrics, e.g. Fisher information, and their Jacobians iteratively over the optimization process. This is especially true for the first-principle electrochemical models [16, 39, 13]. The common approach of sensitivity calculation is to solve the sensitivity differential equations (SDEs), which is obtained by taking the partial derivative of the original model equations to the target variables [40, 16]. Due to lack of analytic solution under generic input, SDEs are typically solved through numerical simulation together with the original model equations. The associated computational load is often intractable for optimization, since most algorithms need to solve the equations iteratively over a large search space to find the optimum [16]. The computational complexity also poses great challenge to data selection/mining for real-time estimation [41, 42], which is subject to stringent constraint on computational power, memory, and time.

Second, the criterion used for optimization suffers from several fundamental deficiencies. Specifically, the ”gold standard” most commonly used is the Fisher information, which is a standard metric for optimal experiment design [43, 44, 45]. However, such metric suffers from several fundamental deficiencies. First, Fisher information is theoretically only related to the variance of estimation error under the assumption of no estimation bias. By inverting the Fisher information, the Cramér-Rao bound of the estimate can be obtained, which indicates the best achievable variance of the estimation error for an unbiased estimator [46, 47, 48]. This is a highly restrictive assumption as in practice estimation bias is not only inevitable, but also often more critical than variance [49], as the commonly presented uncertainties, including those in measurement, model, and model parameters, would induce significant bias in the estimation results. Besides, the Fisher information (FI)/Cramér-Rao bound-based approach only looks to minimize the error variance caused by measurement variance, but neglects other types of commonly presented constant and varying uncertainties in measurement, model, and parameter. In fact, there is not even a systematic way to quantify the estimation error under these uncertainties, let alone reducing/eradicating the error. In addition, the Cramér-Rao bound only gives the best achievable variance in theory with no guarantee that it can be attained in practice (especially for nonlinear systems). All these limitations severely undermine the effectiveness of the conventional data optimization approach, and hence the obtained optimal input profile often only achieves minimal or even no improvement in the estimation results.

1.3 Research objective

The main goal of this dissertation is to create a new data optimization framework for improving the parameter estimation accuracy of the lithium-ion battery cell. This framework is formulated based on analytic expressions for computing and analyzing the sensitivity of battery electrochemical parameters, and new criteria and methodology for estimation error quantification and data optimization.

First, a method for deriving the sensitivity expression of generic battery electrochemical parameters is introduced based on reasonable assumptions and model simplification and reduction techniques. The derived analytic sensitivity expression lays the foundation for subsequent sensitivity analysis and data optimization. It will be shown that for most electrochemical parameters, their sensitivity is composed by a non-dynamic component, which is mainly related to the instantaneous input current, and a semi-linear dynamic component, which also depends on the history of current [39]. To capture the dynamics of sensitivity, we propose to derive a transfer function from current input to the sensitivity, i.e. the sensitivity transfer function (STF). This frequency-domain approach leverages the single particle assumption, linearization, Laplace transform, and Padé approximation. The method is applied to derive the sensitivity for several critical parameters including the solid and electrolyte phase lithium diffusion coefficient D_s and D_e, volume fraction of the electrode active material ε_s, electrode porosity ε_e, separator porosity $\varepsilon_{e,sep}$, and reaction rate constant k. Second, in-depth understanding on the features of parameter sensitivity and sensitive data is obtained from the derived expressions. For example, the STFs are used to analyze the frequency spectrum of dynamic sensitivity and the bandwidth of sensitive data for different parameters, which provide useful insights on data (input) optimization/selection for estimating these parameters. Third, the derived sensitivity based on SPM is compared with the exact numerical simulation based on the P2D model for verification. It is shown that the SPM-based sensitivity matches reasonably well with that of the P2D model within adequate range of operating conditions, demonstrating the validity of the derived analytic expressions.

Second, in order to overcome the fundamental limitations of the conventional data optimization approach, new criteria and method for estimation error quantification and data optimization are established. A formula is first derived to quantify the estimation error caused by measurement, model, and parameter uncertainties for the least-squares algorithm, which is the most commonly used method for parameter estimation. It is interesting to find that Fisher information is only part of the equation, and there are other desirable data structures related to sensitivity that would contribute to error reduction. Based on these findings, new criteria and problem formulations are defined to perform data optimization for improving estimation accuracy. Solving the new problems requires fast and efficient computation and optimization of parameter sensitivity, which is enabled by the previously developed analytical sensitivity computation techniques. The new approach has been applied to the parameter estimation of a reduced order battery electrochemical model, i.e. the single particle model with electrolyte dynamics (SPMe) [13], which has been widely used in battery control and diagnostics research. The estimation results are validated by simulation and experiments under different scenarios, showing significant improvement in accuracy compared with the traditional FI-based approach and other baselines.

1.4 Dissertation organization

The dissertation is organized according to the following structure. Chapter 2 illustrates the methodology to derive the analytic expressions for the sensitivity of battery electrochemical parameters along with the underlying assumptions and model reformulation and simplification techniques. Chapter 3 introduces the new criteria and a novel approach for data optimization and estimation error quantification. The new approach is applied to estimating single parameters of a lithium-ion battery electrochemical model in simulation and experiments to demonstrate its effectiveness. Chapter 4 illustrates the application of the new data optimization framework to identification of the full battery model parameter set, and demonstrates the improvements over the traditional Fisher-information-based approach and other baselines. Finally, Chapter 5 summarizes the main contributions of this dissertation and provides recommendations for future work.

Chapter 2

Analytical Derivation and Analysis of Parameter Sensitivity for Battery Electrochemical Dynamics

The goal of this chapter is to derive the analytic expressions for the sensitivity of battery electrochemical parameters based on reasonable assumptions and model simplification and reduction techniques. The analytical expression is the key to enable theoretic sensitivity analysis under generic current input, tractable offline data optimization, and efficient online sensitivity computation.

2.1 Pseudo-2D electrochemical battery model and single particle simplification

The pseudo-2D (P2D), or the Doyle-Fuller-Newman (DFN) model, is one of the most commonly used electrochemical battery models in practice, formulated based on the theory of porous electrode and concentrated solution [50]. The model provides a microscopic description of the electrochemical processes inside the battery, such as the lithium diffusion and reaction kinetics, and establishes the relationship between internal states, external current input, and voltage output. Due to the computational complexity of solving the coupled partial differential equations (PDEs) in the P2D model, extensive research has been devoted to exploring model reduction/simplification. The single particle model with electrolyte dynamics (SPMe) is a popular reduced order model, especially for real-time control applications[51, 52]. The SPMe is derived under the assumption of uniform reaction current density and solid phase lithium concentration across the battery electrode, so that a single particle can be used to represent the whole electrode, as shown in Fig. 2.1. The model is capable of capturing the electrochemical processes occurring in the anode, separator and cathode regions including the diffusion of lithium ions in the active material and the electrolyte, and the intercalation/deintercalation of lithium ion into/from the electrode particle. The explicit structure of SPMe makes it feasible to derive the analytic sensitivity of the battery electrochemical parameters, which is the objective of this chapter. In this section, a brief overview of the P2D and SPMe models is presented.

2.1.1 Solid-phase lithium diffusion

Based on the Fick's second law, the dynamics of lithium diffusion in an electrode particle is described in spherical coordinate by Eqn. (2.1), with the boundary conditions given in Eqn. (2.2) and Eqn. (2.3). The equation predicts how diffusion causes the solid-phase lithium concentration c_s to change under external current over time along the radius direction of a particle. The subscript i denotes the positive electrode (cathode) when $i = p$ or negative electrode (anode) when $i = n$.

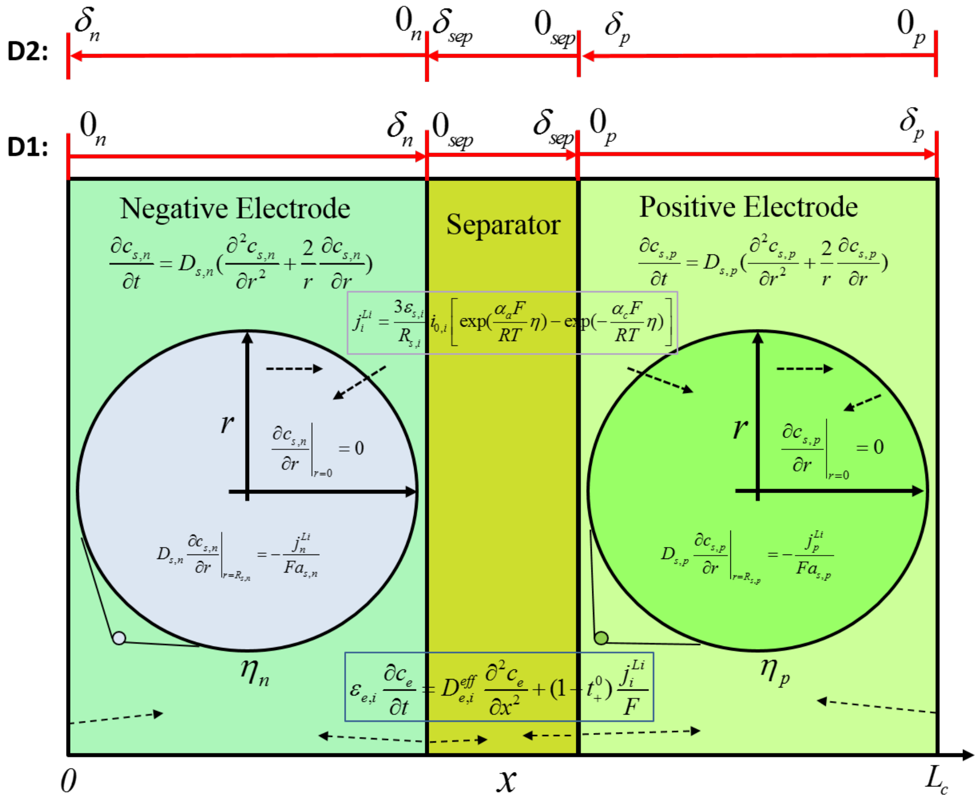

Figure 2.1: Schematic of single particle model with electrolyte dynamics

$$\frac{\partial c_{s,i}}{\partial t} = D_{s,i}\left(\frac{\partial^2 c_{s,i}}{\partial r^2} + \frac{2}{r}\frac{\partial c_{s,i}}{\partial r}\right) \tag{2.1}$$

$$\left.\frac{\partial c_{s,i}}{\partial r}\right|_{r=0} = 0 \tag{2.2}$$

$$D_{s,i}\left.\frac{\partial c_{s,i}}{\partial r}\right|_{r=R_{s,i}} = -\frac{j_i^{Li}}{a_{s,i}F} \tag{2.3}$$

In the above equations, D_s is the solid-phase diffusion coefficient, r is the radial coordinate, R_s is the electrode particle radius, a_s is the specific interfacial area ($a_s = \frac{3\varepsilon_s}{R_s}$), ε_s is the active material volume fraction, F is the Faraday constant, and j_i^{Li} is the intercalation/deintercalation current density. The sign for deintercalation current is positive while that for intercalation current is negative. Under the single particle assumption, j_i^{Li} is assumed to be uniform along the electrode thickness (x) direction, and can be computed as the average current over the electrode thickness,

$$j_i^{Li} = \pm \frac{I}{A\delta_i}, \tag{2.4}$$

where I is the current, A is the electrode area, and δ is the thickness of the region in battery.

Padé approximation is then used to simplify the PDE by deriving a transfer function from I to the lithium concentration at the particle surface c_{se} [53]. First, Laplace transform is applied to convert Eqn. (2.1) to an ODE of c_s with respect to the radial coordinate r in the frequency domain, yielding

$$D_{s,i} \frac{d^2 C_{s,i}(s)}{dr^2} + \frac{2D_{s,i}}{r} \frac{dC_{s,i}(s)}{dr} - sC_{s,i}(s) = 0. \tag{2.5}$$

Then by solving Eqn. (2.5) at the particle surface ($r = R_s$) under the specified boundary conditions, a transcendental transfer function for surface concentration c_{se} is obtained as

$$\frac{C_{se,i}}{I}(s) = -\frac{\left(e^{2R_{s,i}\sqrt{\frac{s}{D_{s,i}}}} - 1\right) \frac{R_{s,i}^2}{3A\delta_i F \varepsilon_{s,i} D_{s,i}}}{1 + R_{s,i}\sqrt{\frac{s}{D_{s,i}}} + e^{2R_{s,i}\sqrt{\frac{s}{D_{s,i}}}}\left(R_{s,i}\sqrt{\frac{s}{D_{s,i}}} - 1\right)}. \tag{2.6}$$

Finally, Padé approximation is applied to simplify the transcendental transfer function to a rational transfer function, of which the coefficients are determined by moment matching [53]. In this work, a 3rd order Padé approximation is adopted,

$$c_{se,i}(s) \approx -\left[\frac{7R_{s,i}^4 s^2 + 420 D_{s,i} R_{s,i}^2 s + 3465 D_{s,i}^2}{F\varepsilon_{s,i} s (R_{s,i}^4 s^2 + 189 D_{s,i} R_{s,i}^2 s + 3465 D_{s,i}^2)}\right] \cdot \frac{I(s)}{A\delta_i}, \tag{2.7}$$

which matches up to 3rd order moment of Eqn. (2.6). The surface concentration c_{se} affects the battery terminal voltage through the open circuit potential, $U(c_{se})$, which is typically a nonlinear function of c_{se} depending on the battery chemistry.

For real-time application, the rational transfer function in Eqn. (2.7) can be implemented in time domain in state space representation to compute the evolution of c_{se} over time driven by the input current I. Eqn. (2.7) will be used to derive the sensitivity transfer function of D_s and ε_s subsequently.

2.1.2 Liquid-phase lithium diffusion

Electrolyte is the medium in which the lithium ions migrate between the cathode and the anode through the separator. The lithium ion concentrations in the electrolyte, c_e, are governed by two physical processes, namely the diffusion caused by the concentration gradient, and the generation or consumption of lithium ion flow (current) j_i^{Li} by the intercalation/deintercalation reaction (except in the separator). Therefore, the dynamics can be described by the Fick's second law in the Cartesian coordinate plus a source term featuring j_i^{Li},

$$\begin{aligned} \text{Anode}: \ \varepsilon_{e,n}\frac{\partial c_e}{\partial t} &= D_{e,n}^{eff}\frac{\partial^2 c_e}{\partial x^2} + (1-t_+^0)\frac{j_n^{Li}}{F}, \ (0 \le x \le \delta_n) \\ \text{Separator}: \ \varepsilon_{e,sep}\frac{\partial c_e}{\partial t} &= D_{e,sep}^{eff}\frac{\partial^2 c_e}{\partial x^2}, \ (\delta_n < x \le \delta_n + \delta_{sep}) \\ \text{Cathode}: \ \varepsilon_{e,p}\frac{\partial c_e}{\partial t} &= D_{e,p}^{eff}\frac{\partial^2 c_e}{\partial x^2} + (1-t_+^0)\frac{j_p^{Li}}{F}, \ (\delta_n + \delta_{sep} < x \le L_c) \end{aligned} \tag{2.8}$$

with boundary conditions

$$\begin{aligned} & c_e\big|_{x=\delta_n^-} = c_e\big|_{x=\delta_n^+}, \qquad c_e\big|_{x=(\delta_n+\delta_{sep})^-} = c_e\big|_{x=(\delta_n+\delta_{sep})^+}, \\ & D_{e,n}^{eff}\left.\frac{\partial c_e}{\partial x}\right|_{x=0} = 0, \qquad D_{e,p}^{eff}\left.\frac{\partial c_e}{\partial x}\right|_{x=L_c} = 0, \\ & D_{e,n}^{eff}\left.\frac{\partial c_e}{\partial x}\right|_{x=\delta_n^-} = D_{e,sep}^{eff}\left.\frac{\partial c_e}{\partial x}\right|_{x=\delta_n^+}, \\ & D_{e,sep}^{eff}\left.\frac{\partial c_e}{\partial x}\right|_{x=(\delta_n+\delta_{sep})^-} = D_{e,p}^{eff}\left.\frac{\partial c_e}{\partial x}\right|_{x=(\delta_n+\delta_{sep})^+}, \end{aligned} \tag{2.9}$$

where ε_e is the porosity, D_e^{eff} is the effective diffusion coefficient of electrolyte ($D_e^{eff} = D_e\varepsilon_e^{1.5}$), D_e is the electrolyte diffusion coefficient, t_+^0 is the transference number, and L_c is the total thickness of the three regions in battery ($L_c = \delta_n + \delta_{sep} + \delta_p$). The subscript sep denotes the separator region, and the superscripts ’-’ and ’+’ of δ stands for the left and right boundary of the interface respectively. Similar to the solid-phase lithium diffusion, single particle assumption and Padé approximation can be used to derive the transfer function from current to the lithium concentration in the electrolyte c_e. By applying Laplace transform to Eqn. (2.8) and solving for $c_e(x, s)$ under the uniform j_i^{Li}assumption in Eqn. (2.4), following transcendental transfer functions can be obtained for the three regions respectively,

$$\begin{aligned} c_{e,n}(s) &= C_1 e^{\sqrt{\frac{s}{D_e^{0.5}}}x} + C_2 e^{-\sqrt{\frac{s}{D_e^{0.5}}}x} + \frac{(1-t_+^0)I(s)}{A\delta_n F\varepsilon_{e,n}s} \\ c_{e,sep}(s) &= C_3 e^{\sqrt{\frac{s}{D_e^{0.5}}}x} + C_4 e^{-\sqrt{\frac{s}{D_e^{0.5}}}x} \\ c_{e,p}(s) &= C_5 e^{\sqrt{\frac{s}{D_e^{0.5}}}x} + C_6 e^{-\sqrt{\frac{s}{D_e^{0.5}}}x} - \frac{(1-t_+^0)I(s)}{A\delta_p F\varepsilon_{e,p}s}. \end{aligned} \tag{2.10}$$

The coefficients C_1, C_2, C_3, C_4, C_5 and C_6 can be obtained by matching the 6 boundary conditions in Eqn. (2.9). Of particular interest are the transfer functions evaluated at the two terminals, namely $x = 0_n$ and $x = \delta_p$ under the coordinate defined as ‘D1’ in Fig. 2.1, which will be subsequently used for determining the battery terminal voltage. Padé approximation is then applied to simplify the transcendental transfer functions to low order rational ones. In this paper, the 1st order Padé approximation is adopted since it is sufficient to match the original transcendental transfer function over a wide frequency range as shown later. During the derivation, the same porosity ε_e value is assumed for the cathode and anode regions and a different one for the separator $\varepsilon_{e,sep}$, which is valid for most lithium ion batteries according to literature [14, 16]. Compared with most prior works which assumed the same ε_e in all 3 regions [54], the assumption in this paper is more generic and reasonable but significantly complicates the Padé approximation process and the expression of the resultant coefficients.

It is found that the complexity of the coefficient expressions depends on how the direction of the x coordinates is defined. Under the coordinate defined as ‘D1’ in Fig. 2.1, a simpler form of the Padé-approximated transfer function can be obtained at $x = \delta_p$ but that at $x = 0_n$ is overwhelmingly complicated. On the other hand, by defining the x-direction in a symmetric but opposite way as shown by ‘D2’ in Fig. 2.1, a simple transfer function can be obtained at $x = \delta_n$ with a complicated one at $x = 0_p$. Therefore, the best approach is to employ these two different coordinate directions to derive the two transfer functions respectively. In addition, due to the difficulty of deriving the Padé-approximated transfer function by keeping the electrode and separator thickness, namely δ_p, δ_n and δ_{sep}, as generic symbols, we need to apply their numerical values during derivation. For example, by taking $\delta_p = 10 \times 10^{-5} m$, $\delta_n = 10 \times 10^{-5} m$, and $\delta_{sep} = 2.5 \times 10^{-5} m$ as in [55], the obtained 1st order transfer function for the electrolyte lithium concentration at the electrode boundaries is

$$C_{e,i}(s) \approx (\pm) \frac{\frac{\varepsilon_e^{1.5} + 4\varepsilon_{e,sep}^{1.5}}{8 \times 10^4 D_e \varepsilon_e^{1.5} \varepsilon_{e,sep}^{1.5}} \cdot \frac{(1-t_+^0)}{AF}}{1 + \frac{\varepsilon_e^2 \varepsilon_{e,sep} + 24\varepsilon_e^3 + 320\varepsilon_{e,sep}^3 + 160\varepsilon_e^{1.5}\varepsilon_{e,sep}^{1.5}}{1.92 \times 10^{10} (4 D_e \varepsilon_e^{0.5} \varepsilon_{e,sep}^3 + D_e \varepsilon_e^2 \varepsilon_{e,sep}^{1.5})} \cdot s} \cdot \ I(s), \tag{2.11}$$

which applies to both anode ($x = 0_n$ in ‘D1’ in Fig. 2.1) and cathode ($x = \delta_p$) since both the porosity and thickness of the two electrodes are identical under the given parameter set.

The electrolyte potential ϕ_e can be obtained based on the Ohm’s law and the electrical effect of the lithium ion concentration variation as [50, 56]

$$i_e = -\kappa^{eff} \frac{\partial \phi_e}{\partial x} + \frac{2\kappa^{eff} RT(1 - t_+^0)}{F} (1 + \gamma) \frac{\partial ln c_e}{\partial x} \tag{2.12}$$

$$\frac{\partial i_e}{\partial x} = j_i^{Li} \tag{2.13}$$

where i_e is the current density in the electrolyte, κ^{eff} is the effective electrolyte conductivity ($\kappa^{eff} = \kappa \varepsilon_e^{1.5}$), κ is the conductivity of electrolyte, R is the universal gas constant, T is the temperature, and γ is the activity coefficient. The current density i_e can be easily obtained by integrating the constant j_i^{Li} over x as in Eqn. (2.13). Then by solving Eqn. (2.12) using the obtained j_i^{Li}, the electrolyte potential difference between the two terminals can be computed as

$$\Delta\phi_e = \phi_e(L_p) - \phi_e(0^-) = \phi_{e,p} - \phi_{e,n} = \Delta\phi_{e,con} + \Delta\phi_{e,\Omega}, \tag{2.14}$$

which includes a lithium concentration polarization term,

$$\Delta\phi_{e,con} = \frac{2RT(1-t_+^0)}{F}(1+\gamma)ln\left(\frac{c_{e,p}}{c_{e,n}}\right), \tag{2.15}$$

and an Ohmic polarization term,

$$\begin{aligned}\Delta\phi_{e,\Omega} &= \int_{0^-}^{\delta_n} \frac{I}{A\kappa_n^{eff}\delta_n} x dx + \int_{0^{sep}}^{\delta_{sep}} \frac{I}{A\kappa_{sep}^{eff}} dx + \int_{0^+}^{\delta_p} \frac{I}{A\kappa_p^{eff}\delta_p} x dx \\ &= \frac{I(\delta_p+\delta_n)}{2A\kappa\varepsilon_e^{1.5}} + \frac{I\delta_{sep}}{A\kappa\varepsilon_{e,sep}^{1.5}}.\end{aligned} \tag{2.16}$$

In Eqn. (2.15), $c_{e,p}$ and $c_{e,n}$ can be calculated by using the time domain state space representation of the transfer function in Eqn. (2.11).

Eqn. (2.11), (2.15) and (2.16) will be used to analytically derive the sensitivity of the electrolyte lithium diffusion coefficient D_e, porosity ε_e and ε_{sep} subsequently.

2.1.3 Lithium intercalation/deintercalation

The lithium intercalation/deintercalation reaction at the electrode particle surface, i.e. the insertion/removal of lithium ions into/from the particle, is driven by the overpotential

$$\eta_i = \phi_{s,i} - \phi_{e,i} - U_i(c_{se,i}) - R_{f,i}\frac{j_i^{Li}}{a_{s,i}}, \tag{2.17}$$

which is the surplus of the electrode potential ϕ_s over the electrolyte potential ϕ_e, open circuit potential U that depends on the surface concentration c_{se}, and the Ohmic potential drop over the solid-electrolyte-interphase (SEI) film resistance R_f. The overpotential governs the reaction current density j_i^{Li} based on the Butler-Volmer Equation,

$$j_i^{Li} = a_{s,i} i_{0,i} \left[exp(\frac{\alpha_a F}{RT}\eta_i) - exp(-\frac{\alpha_c F}{RT}\eta_i) \right], \tag{2.18}$$

where α_a and α_c are the anodic and cathodic charge transfer coefficients respectively. The exchange current $i_{0,i}$ takes the form

$$i_{0,i} = F k_i (c_e)^{\alpha_a} (c_{s,i}^{max} - c_{se,i})^{\alpha_a} (c_{se,i})^{\alpha_c}, \tag{2.19}$$

with k being the reaction rate constant and c_s^{max} being the maximum concentration of the electrode material.

In SPMe, since j_i^{Li} has been obtained based on the single particle assumption in Eqn. (2.4), the overpotential η_i can be calculated by inverting Eqn. (2.18) as

$$\eta_i = \frac{RT}{\alpha F} ln(\xi_i + \sqrt{\xi_i^2 + 1}), \tag{2.20}$$

where

$$\xi_i = \frac{j_i^{Li}}{2 a_{s,i} i_{0,i}}. \tag{2.21}$$

Eqn. (2.20) and Eqn. (2.21) will be used to analytically derive the sensitivity for ε_s and k.

2.1.4 Battery terminal voltage

The output of the model, i.e. the battery terminal voltage, is the solid-phase potential difference between the boundaries of the cathode and anode plus the voltage drop over a resistance R_c, which includes the resistance of current collectors and all wiring,

$$V = \phi_s(L) - \phi_s(0^-) - R_c \frac{I}{A} = \phi_{s,p} - \phi_{s,n} - R_c \frac{I}{A}. \tag{2.22}$$

According to Eqn. (2.17), $\phi_{s,i}$ can be calculated as

$$\phi_{s,i} = \eta_i + \phi_{e,i} + U_i(c_{se,i}) + R_{f,i}\frac{j_i^{Li}}{a_{s,i}}. \tag{2.23}$$

Therefore, by combining Eqn. (2.22) and Eqn. (2.23), the battery terminal voltage is obtained as,

$$\begin{aligned} V = \phi_{s,p} - \phi_{s,n} = &(U_p - U_n) + (\phi_{e,p} - \phi_{e,n}) + (\eta_p - \eta_n) \\ &- \left(R_c\frac{I}{A} + \frac{IR_{f,p}}{A\delta_p a_{s,p}} + \frac{IR_{f,n}}{A\delta_n a_{s,n}} \right). \end{aligned} \tag{2.24}$$

By lumping all Ohmic resistance into R_Ω, and decomposing $\phi_{e,p} - \phi_{e,n}$ into $\Delta\phi_{e,con}$ and $\Delta\phi_{e,\Omega}$ according to Eqn. (2.14), Eqn. (2.24) can be rewritten as

$$V = U_p(c_{se,p}) - U_n(c_{se,n}) + \Delta\phi_{e,con}(c_e) + \eta_p(c_{se,p}) - \eta_n(c_{se,n}) - IR_\Omega, \tag{2.25}$$

where

$$R_\Omega = \frac{R_c}{A} + \frac{R_{f,p}}{A\delta_p a_{s,p}} + \frac{R_{f,n}}{A\delta_n a_{s,n}} + \frac{(\delta_p + \delta_n)}{2A\kappa\varepsilon_e^{1.5}} + \frac{\delta_{sep}}{A\kappa\varepsilon_{e,sep}^{1.5}}. \tag{2.26}$$

In Eqn. (2.25), c_{se}, $\Delta\phi_{e,con}$, and η have been obtained in the previous sub-models. It is seen that the terminal voltage can be decomposed into 4 parts, which are related to the open circuit potential U, electrolyte concentration polarization potential $\Delta\phi_{e,con}$, overpotential η, and lumped ohmic resistance R_Ω respectively.

2.2 Methodology and procedures for deriving parameter sensitivity

The output (voltage) sensitivity of a generic battery parameter θ, $\frac{\partial V}{\partial \theta}$, can be obtained by applying the chain rule of differentiation to the voltage equation in Eqn. (2.25),

$$\begin{aligned} \frac{\partial V}{\partial \theta} &= \frac{\partial U(c_{se})}{\partial \theta} + \frac{\partial \Delta\phi_{e,con}(c_e)}{\partial \theta} + \frac{\partial \eta(c_{se}, a_s)}{\partial \theta} - \frac{\partial R_\Omega}{\partial \theta} I \\ &= \frac{\partial U(c_{se})}{\partial c_{se}} \frac{\partial c_{se}}{\partial \theta} + \frac{\partial \Delta\phi_{e,con}(c_e)}{\partial c_e} \frac{\partial c_e}{\partial \theta} + \left(\frac{\partial \eta}{\partial c_{se}} \frac{\partial c_{se}}{\partial \theta} + \frac{\partial \eta}{\partial a_s} \frac{\partial a_s}{\partial \theta} \right) - \frac{\partial R_\Omega}{\partial \theta} I. \end{aligned} \tag{2.27}$$

Among all the terms in Eqn. (2.27), $\frac{\partial R_\Omega}{\partial \theta} I$ is referred to as the linear non-dynamic term as it is related to the linear ohmic resistance R_Ω and not subject to system dynamics, e.g. lithium ion diffusion; $\frac{\partial \eta}{\partial a_s} \frac{\partial a_s}{\partial \theta}$ is the nonlinear non-dynamic term as it is related to the nonlinear overpotential η and not subject to system dynamics; $\frac{\partial U(c_{se})}{\partial c_{se}} \frac{\partial c_{se}}{\partial \theta}$, $\frac{\partial \Delta\phi_{e,con}(c_e)}{\partial c_e} \frac{\partial c_e}{\partial \theta}$ and $\frac{\partial \eta}{\partial c_{se}} \frac{\partial c_{se}}{\partial \theta}$ are the semi-linear dynamic terms, as they depend on both the sensitivity of certain dynamic states, i.e. $\frac{\partial c_{se}}{\partial \theta}$ or $\frac{\partial c_e}{\partial \theta}$, which are governed by the linear diffusion dynamics, and a certain nonlinear coefficient, i.e. $\frac{\partial U(c_{se})}{\partial c_{se}}$, $\frac{\partial \Delta\phi_{e,con}(c_e)}{\partial c_e}$ or $\frac{\partial \eta}{\partial c_{se}}$.

Different procedures need to be applied to derive the dynamic and non-dynamic terms of sensitivity, as summarized in the flowchart shown in Fig. 2.2. The derivation of non-dynamic terms is straightforward, which only involves directly taking the partial derivative to θ to obtain the sensitivity as a function of the input current. The derivation of dynamic terms is more complicated since the state sensitivity, $\frac{\partial c_{se}}{\partial \theta}$ and $\frac{\partial c_e}{\partial \theta}$, depends on the diffusion dynamics of c_{se} or c_e and will evolve over time even under constant input current. To characterize the dynamics of the state sensitivity in an analytic and compact manner, we apply frequency-domain techniques to derive a transfer function from input current I to the state sensitivity, which is referred to as the sensitivity transfer function (STF). Specifically, by performing the Laplace transform, the linear governing PDE of the state dynamics is converted to a frequency domain ODE. The ODE is then solved along with the boundary conditions to obtain a transfer function from current to the state, which is typically transcendental. Padé approximation is then used to simplify the transcendental transfer function to a low order rational transfer function to facilitate the derivation of sensitivity and implementation in time domain. The above steps have already been performed in Section 2.1. It is noted that the obtained transfer function is analytical as the coefficients are explicitly dependent on the physical parameter θ. Therefore, by taking the partial derivative of the transfer function to θ, the STF from current I to $\frac{\partial c}{\partial \theta}$ is obtained. The STF can be converted to time domain, e.g. via state space representation, to compute the evolution of the state sensitivity over time, which can then be multiplied by the nonlinear coefficient to calculate the dynamic terms of the voltage sensitivity. Finally, the (total) voltage sensitivity can be obtained by combining the dynamic terms and the non-dynamic terms.

2.3 Derivation of sensitivity for specific parameters

In this section, the formulated methodology is applied to derive the sensitivity of specific battery electrochemical parameters, including the solid phase diffusion coefficient D_s, volume fraction of the electrode active material ε_s, reaction rate constant k, porosity ε_e and $\varepsilon_{e,sep}$, and electrolyte diffusion coefficient D_e. These parameters have major impacts on battery electrochemical behaviors and key performance indexes including state of charge (SOC), state of health (SOH), and state of power (SOP). The proposed methodology can be applied

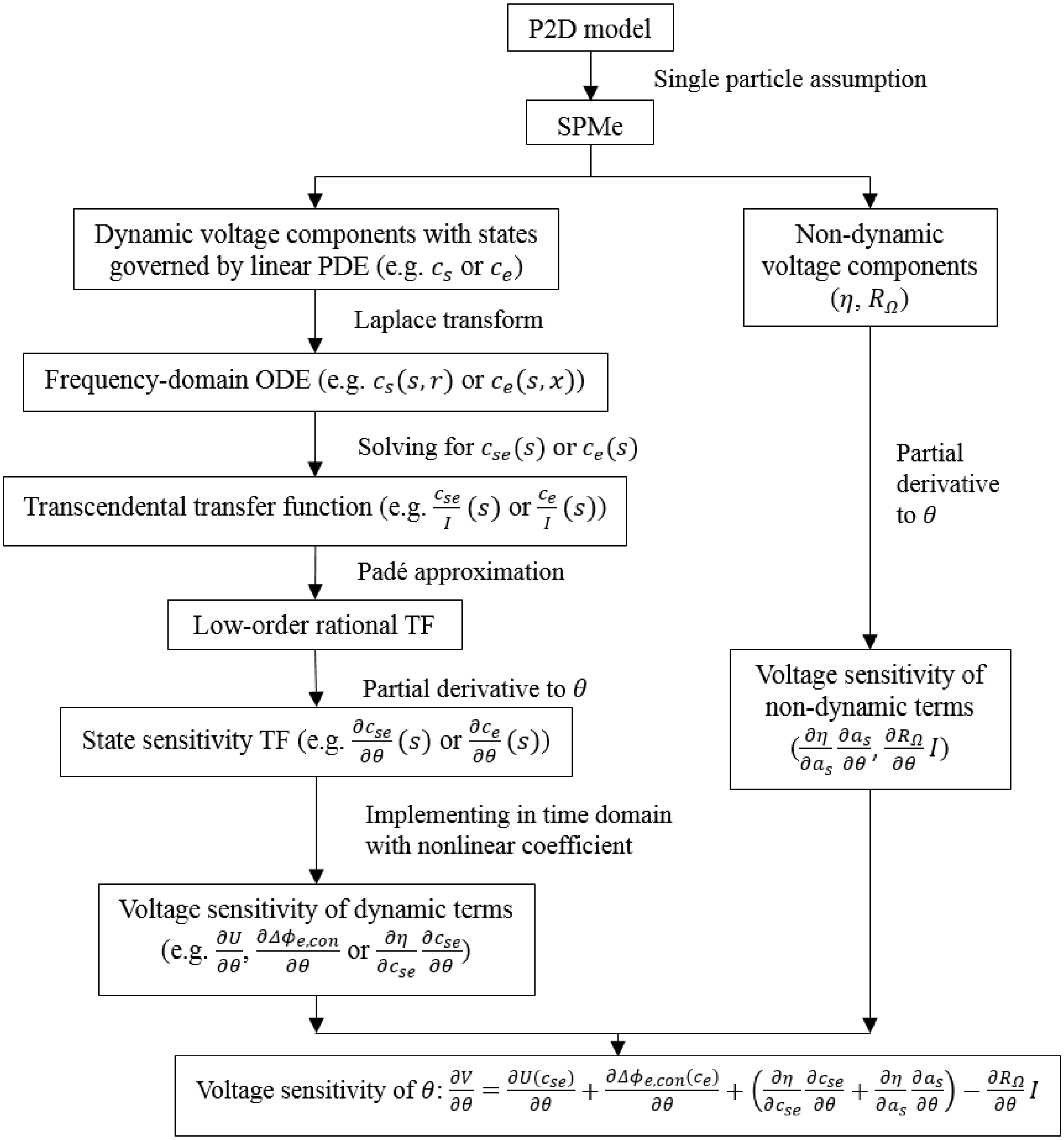

Figure 2.2: Flowchart of parameter sensitivity derivation

to other parameters without loss of generality.

2.3.1 Sensitivity of solid phase diffusion coefficient D_s

The solid phase diffusion coefficient D_s affects the particle surface lithium concentration c_{se} and hence the battery terminal voltage V through the open circuit potential U and overpotential η, according to Eqn. (2.7) and Eqn. (2.25). Therefore, by applying the chain rule of differentiation, the sensitivity of D_s can be obtained as

$$\frac{\partial V}{\partial D_s} = \left(\frac{\partial U}{\partial c_{se}} + \frac{\partial \eta}{\partial c_{se}}\right) \cdot \frac{\partial c_{se}}{\partial D_s}, \tag{2.28}$$

where $\frac{\partial U}{\partial c_{se}}$ is the slope of the open circuit potential (OCP). The second term, $\frac{\partial \eta}{\partial c_{se}}\frac{\partial c_{se}}{\partial D_s}$, represents the impact of D_s on the exchange current density i_0 which affects the overpotential through the particle surface concentration c_{se}, where $\frac{\partial \eta}{\partial c_{se}}$ can be obtained as

$$\frac{\partial \eta}{\partial c_{se}} = \frac{RT}{2\alpha F} \cdot \frac{1}{\sqrt{1+\xi^{-2}}}[c_e c_{se}(c_s^{max} - c_{se})]^{-1}(c_e c_s^{max} - 2c_e c_{se}). \tag{2.29}$$

The key step then is to derive the expression for $\frac{\partial c_{se}}{\partial D_s}$. Since lithium diffusion is a dynamic process, the impact of D_s on c_{se} will change over time and needs to be captured with a dynamic model. This can be achieved by using the analytical transfer function from I to c_{se} obtained in Eqn. (2.7). By taking the partial derivative of Eqn. (2.7) to D_s, a sensitivity transfer function (STF) for $\frac{\partial c_{se}}{\partial D_s}$ can be obtained as

$$\frac{\partial C_{se}}{\partial D_s}(s) = \frac{21R_s^2(43R_s^4 s^2 + 1980 D_s R_s^2 s + 38115 D_s^2)}{F\varepsilon_s A\delta(R_s^4 s^2 + 189 D_s R_s^2 s + 3465 D_s^2)^2} \cdot I(s). \tag{2.30}$$

The coefficients in Eqn. (2.30) are in the form of symbolic battery parameters, which are easily adaptable to different battery chemistries. The derived STF can be conveniently used for both frequency domain and time domain analysis.

In frequency domain, the dynamic nature of $\frac{\partial c_{se}}{\partial D_s}$ can be studied based on the Bode plot of the sensitivity transfer function. Fig. 2.3 shows the Bode plot of the normalized sensitivity $\frac{\partial c_{se}}{\partial D_s} D_s$ for the cathode of the battery using parameters in [55]. The blue solid line represents the frequency response of the analytic STF and the red line shows that of the sensitivity obtained based on the transcendental transfer function in Eqn. (2.6). The two matches very well at low frequency (up to around 0.1 Hz), as the moment matching to determine the Padé approximation coefficients is performed at s=0. The fidelity is considered as adequate since the sensitivity starts to decay rapidly beyond 0.1 Hz. According to the plot, $\frac{\partial c_{se,p}}{\partial D_{s,p}}$ is sensitive to low frequency current input, as the magnitude is constant in low frequency range and drops quickly after the break frequency at between 0.01 and 0.1 Hz. This observation is consistent with the well-known battery Electrochemical Impedance Spectroscopy (EIS) results [57], which attribute the low frequency tail of the Nyquist plot to solid-phase diffusion. Furthermore, the theoretic value of the break frequency between the low-frequency sensitive range and high-frequency insensitive range for D_s can be estimated from the Bode plot and Eqn. (2.30). The magnitude plot can be approximated by two line segments as shown in Fig. 2.3. The low-frequency segment 'L1' is found by taking the magnitude of the frequency response to $\omega = 0$,

$$|G_1(j\omega)| = \lim_{\omega \to 0} \left| \frac{\frac{\partial C_{se}}{\partial D_s} \cdot D_s}{I}(j\omega) \right| = \frac{R_s^2}{15F\varepsilon_s A\delta D_s}. \tag{2.31}$$

The high-frequency segment 'L2' can be obtained by taking the frequency response to $\omega = \infty$,

$$|G_2(j\omega)| = \lim_{\omega \to \infty} \left| \frac{\frac{\partial C_{se}}{\partial D_s} \cdot D_s}{I}(j\omega) \right| = \frac{903D_s}{F\varepsilon_s A\delta R_s^2\omega^2}. \tag{2.32}$$

The break frequency ω_b is the intersection of the two segments, obtained by equating Eqn.

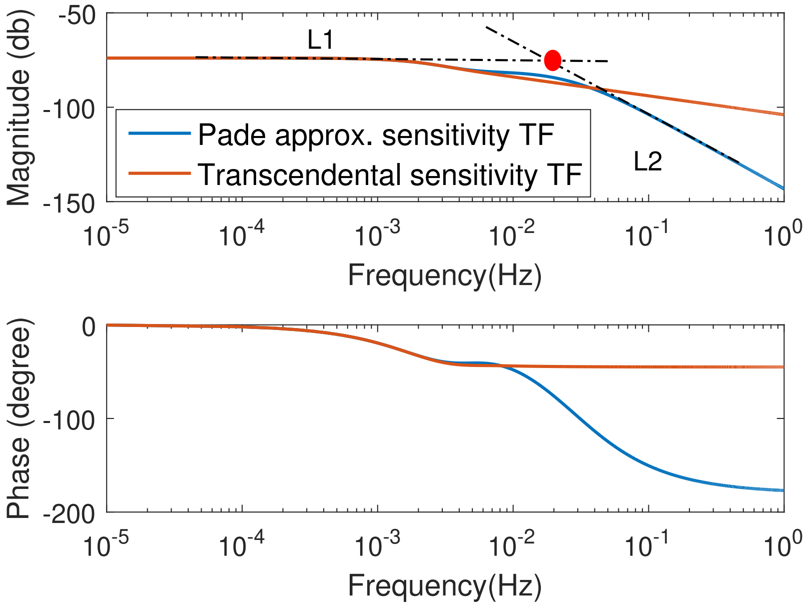

Figure 2.3: Bode plot of normalized sensitivity transfer function of $\frac{\partial c_{se,p}}{\partial D_{s,p}}$

(2.31) with (2.32),

$$\omega_b = \frac{116 D_s}{R_s^2}. \tag{2.33}$$

This result indicates that the sensitive frequency range of the diffusion coefficient depends on D_s and the particle radius R_s. Interestingly, it has been found in EIS study that there is a transition frequency in the low-frequency tail portion of the Nyquist plot, which indicates the transition from semi-infinite diffusion to finite-space diffusion [58]. The transition frequency takes a similar form as Eqn. (2.33) [58, 59], indicating possible correlation between the two which remains to be identified. These analytical results provide useful insights for experiment/input design to optimize the estimation of D_s.

The sensitivity transfer function can be easily converted to state space representation in time domain, e.g. through the canonical form as

$$\begin{bmatrix} \dot{x_1} \\ \dot{x_2} \\ \dot{x_3} \\ \dot{x_4} \end{bmatrix} = \begin{bmatrix} 0 & 1 & 0 & 0 \\ 0 & 0 & 1 & 0 \\ 0 & 0 & 0 & 1 \\ -\frac{12006225 D_s^4}{R_s^8} & -\frac{1309770 D_s^3}{R_s^6} & -\frac{42651 D_s^2}{R_s^4} & -\frac{378 D_s}{R_s^2} \end{bmatrix} \begin{bmatrix} x_1 \\ x_2 \\ x_3 \\ x_4 \end{bmatrix} + \begin{bmatrix} 0 \\ 0 \\ 0 \\ 1 \end{bmatrix} I \tag{2.34}$$

$$\frac{\partial c_{se}(t)}{\partial D_s} = \frac{21}{F \varepsilon_s A \delta R_s^6} \begin{bmatrix} 38115 D_s^2 & 1980 D_s R_s^2 & 43 R_s^4 & 0 \end{bmatrix} \begin{bmatrix} x_1 \\ x_2 \\ x_3 \\ x_4 \end{bmatrix}. \tag{2.35}$$

The formula can be used to compute the sensitivity of D_s under any current input $I(t)$ in real time efficiently. We will compare the results of the analytic derivation based on SPMe with numerical simulation of the sensitivity differential equations (SDE) based on the original full-order P2D model in Section 2.4 for verification.

2.3.2 Sensitivity of active material volume fraction ε_s

According to Eqn. (2.25), the active material volume fraction ε_s affects V through the lumped Ohmic resistance, open circuit potential U, and the overpotential η. Hence the sensitivity is obtained by applying the chain rule of differentiation as

$$\frac{\partial V}{\partial \varepsilon_s} = \frac{\partial R_\Omega}{\partial \varepsilon_s} I + \frac{\partial \eta}{\partial a_s} \frac{\partial a_s}{\partial \varepsilon_s} + \left(\frac{\partial \eta}{\partial c_{se}} + \frac{\partial U}{\partial c_{se}} \right) \cdot \frac{\partial c_{se}}{\partial \varepsilon_s}, \tag{2.36}$$

which consists of four terms. The first term, $\frac{\partial R_\Omega}{\partial \varepsilon_s} I$, is the linear non-dynamic term which reflects the impact of ε_s on the resistance of SEI. It can be obtained by differentiating Eqn.

(2.26) to ε_s as

$$\frac{\partial R_\Omega}{\partial \varepsilon_s} = \frac{-R_f R_s}{3A\delta\varepsilon_s^2}. \tag{2.37}$$

The second term, $\frac{\partial \eta}{\partial a_s}\frac{\partial a_s}{\partial \varepsilon_s}$, is the nonlinear non-dynamic terms that can be derived by differentiating Eqn. (2.20) to ε_s and substituting j^{Li} with I based on Eqn. (2.4),

$$\frac{\partial \eta}{\partial a_s}\frac{\partial a_s}{\partial \varepsilon_s} = \frac{-RT}{\alpha F \varepsilon_s} \cdot \frac{\text{sign}(I)}{\sqrt{1+\frac{1}{\xi^2}}} = \frac{-RT}{\alpha F \varepsilon_s} \cdot \frac{\text{sign}(I)}{\sqrt{1+\left(\frac{6\varepsilon_s i_0 A\delta}{IR_s}\right)^2}}. \tag{2.38}$$

It is seen that $\frac{\partial \eta}{\partial a_s}\frac{\partial a_s}{\partial \varepsilon_s}$ is a nonlinear function of current I, and changes instantaneously with current. The remaining two terms are the semi-linear dynamic terms of the ε_s sensitivity. Specifically, the third term $\frac{\partial \eta}{\partial c_{se}}\frac{\partial c_{se}}{\partial \varepsilon_s}$ represents the impact of ε_s on the exchange current density i_0 which affects the overpotential through the particle surface concentration c_{se}, where the nonlinear coefficient $\frac{\partial \eta}{\partial c_{se}}$ has been obtained in Eqn. (2.29). The fourth term, $\frac{\partial U}{\partial c_{se}}\frac{\partial c_{se}}{\partial \varepsilon_s}$ accounts for the impact of ε_s on open circuit potential (OCP) through the particle surface concentration c_{se}.

The state sensitivity $\frac{\partial c_{se}}{\partial \varepsilon_s}$ can be derived using the same method for deriving $\frac{\partial c_{se}}{\partial D_s}$. Specifically, by taking the partial derivative of c_{se} to ε_s in Eqn. (2.7), the sensitivity transfer function of $\frac{\partial c_{se}}{\partial \varepsilon_s}$ can be obtained as

$$\frac{\partial C_{se}}{\partial \varepsilon_s}(s) = \left[\frac{7R_s^4 s^2 + 420 D_s R_s^2 s + 3465 D_s^2}{Fs(R_s^4 s^2 + 189 D_s R_s^2 s + 3465 D_s^2)}\right] \cdot \frac{I(s)}{{\varepsilon_s}^2 A\delta}. \tag{2.39}$$

For frequency domain analysis, the Bode plot of the normalized sensitivity, $\frac{\partial C_{se,p}}{\partial \varepsilon_{s,p}}(s) \cdot \varepsilon_{s,p}$, is shown in Fig. 2.4. Similar to the normalized $\frac{\partial C_{se,p}}{\partial D_{s,p}}(s)$ in Fig. 2.3, the analytic STF derived based on the 3rd order Padé approximation matches well with the sensitivity of the original transcendental transfer function, especially in the frequency range below 0.1

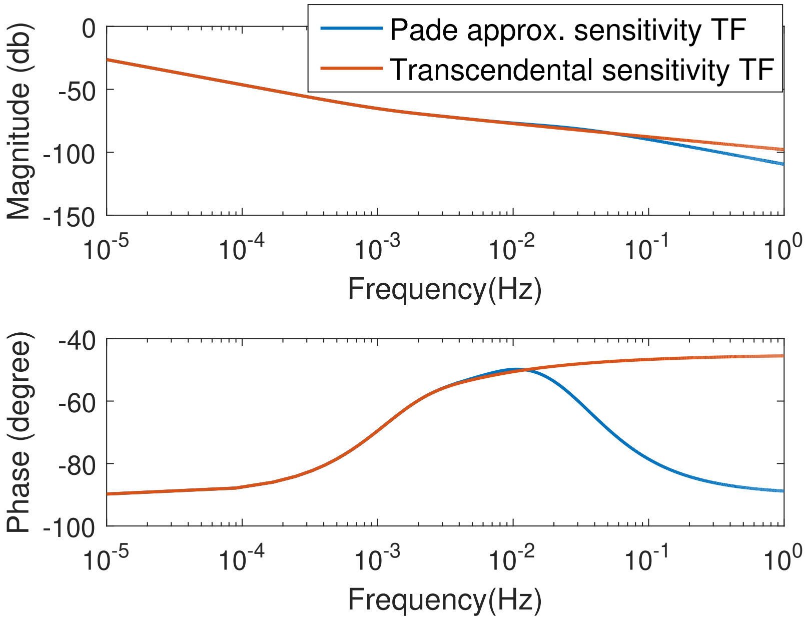

Figure 2.4: Bode plot of normalized sensitivity transfer function of $\frac{\partial c_{se,p}}{\partial \varepsilon_{s,p}}$

Hz. The mismatch beyond that frequency is less of a concern due to the low magnitude. It is interesting to note that the frequency response of $\frac{\partial c_{se}}{\partial \varepsilon_s}$ is fundamentally different from that of $\frac{\partial c_{se}}{\partial D_s}$. Instead of remaining constant in low frequency range and rolling off after the break frequency, $\frac{\partial c_{se}}{\partial \varepsilon_s}$ shows a monotonically decreasing trend over the whole frequency range due to the fact that $\frac{\partial C_{se}}{\partial \varepsilon_s}(s)$ contains a pole at s = 0 according to Eqn. (2.39). This observation reveals the distinctive dynamic nature of the sensitivity of different parameters and demonstrates the necessity of studying them respectively. The implication of different sensitivity dynamics will be analyzed in the subsequent simulation section in detail.

2.3.3 Sensitivity of reaction rate constant k

Reaction rate constant k affects the terminal voltage V solely through the over-potential η, and hence the sensitivity is obtained by differentiating Eqn. (2.25) to k,

$$\frac{\partial V(t)}{\partial k} = \frac{\partial \eta(t)}{\partial k}, \tag{2.40}$$

which is a nonlinear non-dynamic term

$$\frac{\partial \eta}{\partial k} = \frac{\partial \eta}{\partial \xi} \cdot \left(\frac{\partial \xi}{\partial k} \right) = \frac{-RT}{\alpha F k} \cdot \frac{\text{sign}\,(I)}{\sqrt{1+\frac{1}{\xi^2}}} = \frac{-RT}{\alpha F k} \cdot \frac{\text{sign}(I)}{\sqrt{1+\left(\frac{6\varepsilon_s i_0 A \delta}{I R_s}\right)^2}}. \tag{2.41}$$

It is noted that the normalized sensitivity of $\frac{\partial \eta(t)}{\partial k}$ is essentially the same as the normalized $\frac{\partial \eta(t)}{\partial a_s}\frac{\partial a_s}{\partial \varepsilon_s}$, and hence their behavior is similar.

2.3.4 Sensitivity of electrolyte diffusion coefficient D_e

According to Eqn. (2.8), the electrolyte diffusion coefficient D_e governs the evolution of the electrolyte concentration c_e. The c_e gradient induces potential difference across the electrodes, which affects the battery terminal voltage. Therefore, by applying the chain rule of differentiation to Eqn. (2.25), the sensitivity of D_e takes the form of a semi-linear dynamic term,

$$\begin{aligned} \frac{\partial V}{\partial D_e} &= \frac{\partial \Delta \phi_{e,con}}{\partial D_e} = \frac{\partial \Delta \phi_{e,con}}{\partial c_e} \frac{\partial c_e}{\partial D_e} \\ &= \frac{2RT(1-t_+^0)}{F}(1+\gamma)\left(\frac{1}{c_{e,p}} \frac{\partial c_{e,p}}{\partial D_e} - \frac{1}{c_{e,n}} \frac{\partial c_{e,n}}{\partial D_e} \right). \end{aligned} \tag{2.42}$$

For state sensitivity $\frac{\partial c_e}{\partial D_e}$, similar to $\frac{\partial c_{se}}{\partial D_s}$, we can derive a sensitivity transfer function by taking the partial derivative of Eqn. (2.11) to D_e,

$$\frac{\partial C_{e,i}}{\partial D_e}(s) = \frac{\pm \frac{\left(\varepsilon_e^{1.5} + 4\varepsilon_{e,sep}^{1.5}\right)\left(1-t_0^+\right)}{8\times 10^4 F A D_e^2 \varepsilon_e^{1.5} \varepsilon_{e,sep}^{1.5}} I(s)}{\frac{\left(\varepsilon_e^2 \varepsilon_{e,sep} + 24\varepsilon_e^3 + 320\varepsilon_{e,sep}^3 + 160\varepsilon_e^{1.5}\varepsilon_{e,sep}^{1.5}\right)^2}{3.6864\times 10^{20}\left(4D_e \varepsilon_e^{0.5}\varepsilon_{e,sep}^3 + D_e \varepsilon_e^2 \varepsilon_{e,sep}^{1.5}\right)^2} s^2 + \frac{\left(\varepsilon_e^2 \varepsilon_{e,sep} + 24\varepsilon_e^3 + 320\varepsilon_{e,sep}^3 + 160\varepsilon_e^{1.5}\varepsilon_{e,sep}^{1.5}\right)}{9.6\times 10^9\left(4D_e \varepsilon_e^{0.5}\varepsilon_{e,sep}^3 + D_e \varepsilon_e^2 \varepsilon_{e,sep}^{1.5}\right)} s + 1} \tag{2.43}$$

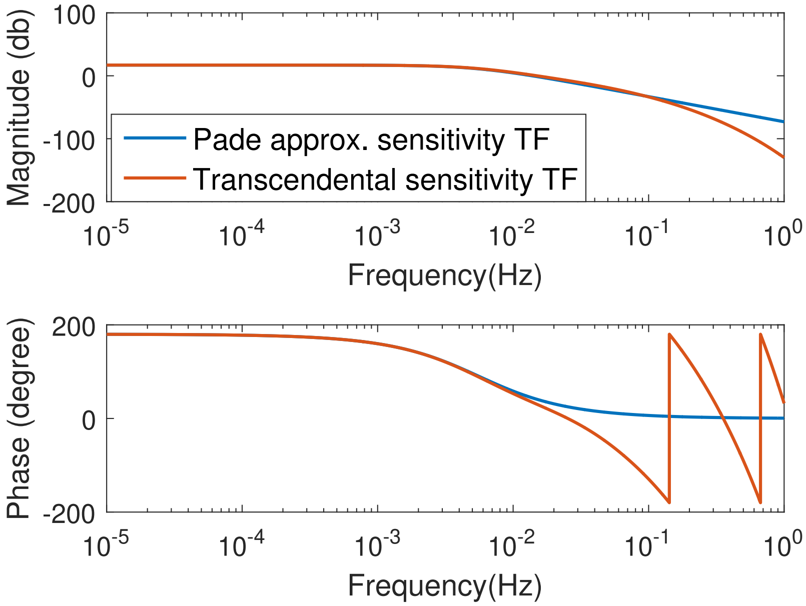

Figure 2.5: Bode plot of normalized sensitivity transfer function of $\frac{\partial c_{e,p}}{\partial D_e}$

In frequency domain, the dynamic nature of (normalized) $\frac{\partial c_e}{\partial D_e}$ can be studied based on the Bode plot shown in Fig. 2.5. The blue line stands for the frequency response of the analytic STF and the red line represents the sensitivity calculated based on the original transcendental transfer function. The two match well at low frequency up to around 0.1 Hz, after which both start to decay rapidly. It can be seen that $\frac{\partial c_e}{\partial D_e}$ is sensitive to low frequency current input, and the theoretic value of the break frequency between the low-frequency sensitive range and high-frequency insensitive range can be estimated from the STF. The sensitivity transfer function can be easily converted to state space representation in time domain to calculate the sensitivity $\frac{\partial c_e}{\partial D_e}$ under any current input I.

2.3.5 Sensitivity of porosity ε_e

According to Eqns. (2.14-2.16), the porosity ε_e affects the terminal voltage V through the electrolyte concentration polarization potential $\Delta\phi_{e,con}$ shown in Eqn. (2.15) and the ohmic polarization potential IR_Ω in Eqn. (2.25). Hence the sensitivity is obtained by applying the chain rule of differentiation to Eqn. (2.25) as

$$\frac{\partial V}{\partial \varepsilon_e} = \frac{\partial R_\Omega}{\partial \varepsilon_e} \cdot I + \frac{\partial \Delta\phi_{e,con}}{\partial c_e} \cdot \frac{\partial c_e}{\partial \varepsilon_e}, \tag{2.44}$$

which consists of two terms. The first term, $\frac{\partial R_\Omega}{\partial \varepsilon_e} \cdot I$, is the linear non-dynamic term related to the ohmic resistance of the electrolyte, which can be derived by differentiating Eqn. (2.26) to ε_e as

$$\frac{\partial R_\Omega}{\partial \varepsilon_e} = \frac{0.75(\delta_p + \delta_n)}{\kappa \varepsilon_e^{2.5} A}. \tag{2.45}$$

The second term, $\frac{\partial \Delta\phi_{e,con}}{\partial c_e} \cdot \frac{\partial c_e}{\partial \varepsilon_e}$, is the semi-linear dynamic term, which captures the impact of ε_e on $\Delta\phi_{e,con}$ through the electrolyte concentration c_e. It can be derived by applying the chain rule of differentiation to Eqn. (2.25) as

$$\frac{\partial \Delta\phi_{e,con}}{\partial c_e} \cdot \frac{\partial c_e}{\partial \varepsilon_e} = \frac{2RT(1 - t_+^0)}{F}(1+\gamma)\left(\frac{1}{c_{e,p}}\frac{\partial c_{e,p}}{\partial \varepsilon_e} - \frac{1}{c_{e,n}}\frac{\partial c_{e,n}}{\partial \varepsilon_e}\right). \tag{2.46}$$

Similar to $\frac{\partial c_e}{\partial D_e}$, the sensitivity transfer function of $\frac{\partial c_e}{\partial \varepsilon_e}$ can be obtained by taking the partial derivative of $C_e(s)$ to ε_e in Eqn. (2.11),

$$\frac{\partial C_{e,i}}{\partial \varepsilon_e}(s) = \frac{\pm\left(\frac{6\varepsilon_e^{4.5}+320\varepsilon_{e,sep}^{4.5}+76\varepsilon_e^{3}\varepsilon_{e,sep}^{1.5}+240\varepsilon_e^{1.5}\varepsilon_{e,sep}^{3}+3\varepsilon_e^{2}\varepsilon_{e,sep}^{2.5}}{3.84\times10^{14}D_e^2\varepsilon_e^3\varepsilon_{e,sep}^3\left(\varepsilon_e^{1.5}+4\varepsilon_{e,sep}^{1.5}\right)}s+\frac{3}{4\times10^4(D_e\varepsilon_e^{2.5})}\right)\frac{1-t_0^+}{FA}I(s)}{\frac{\left(\varepsilon_e^2\varepsilon_{e,sep}+24\varepsilon_e^3+320\varepsilon_{e,sep}^3+160\varepsilon_e^{1.5}\varepsilon_{e,sep}^{1.5}\right)^2}{3.6864\times10^{20}\left(4D_e\varepsilon_e^{0.5}\varepsilon_{e,sep}^3+D_e\varepsilon_e^2\varepsilon_{e,sep}^{1.5}\right)^2}s^2+\frac{\left(\varepsilon_e^2\varepsilon_{e,sep}+24\varepsilon_e^3+320\varepsilon_{e,sep}^3+160\varepsilon_e^{1.5}\varepsilon_{e,sep}^{1.5}\right)}{9.6\times10^9\left(4D_e\varepsilon_e^{0.5}\varepsilon_{e,sep}^3+D_e\varepsilon_e^2\varepsilon_{e,sep}^{1.5}\right)}s+1} \tag{2.47}$$

For frequency domain analysis, the Bode plot of (the normalized) STF of $\frac{\partial c_e}{\partial \varepsilon_e}$ is shown in Fig. 2.6. The frequency response based on the analytical 1st order Padé approximation

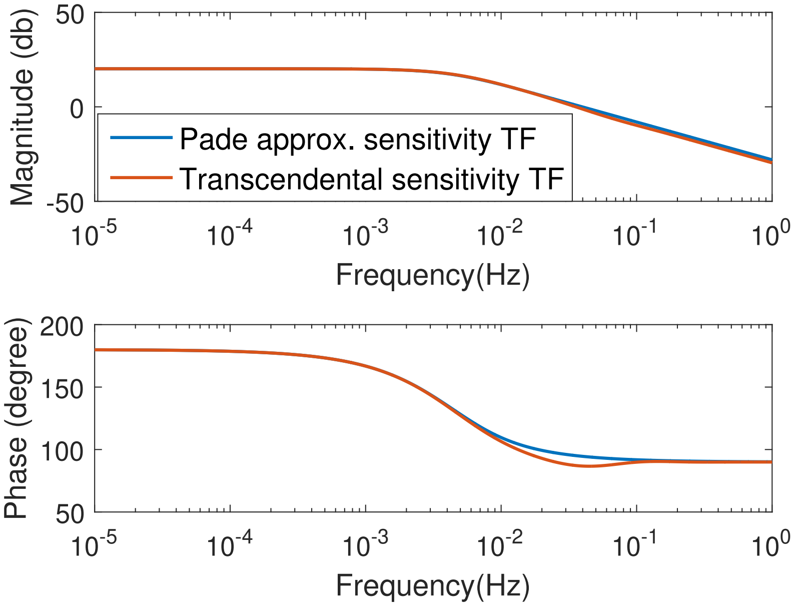

Figure 2.6: Bode plot of normalized sensitivity transfer function of $\frac{\partial c_{e,p}}{\partial \varepsilon_e}$

are in good agreement with that based on the original transcendental transfer function. It is noted that the frequency response of $\frac{\partial c_e}{\partial \varepsilon_e}$ is different from its solid-phase counterpart $\frac{\partial c_{se}}{\partial \varepsilon_s}$, i.e. the active material volume fraction. Compared with $\frac{\partial C_{se}}{\partial \varepsilon_s}(s)$ which decreases monotonically over frequency, $\frac{\partial C_e}{\partial \varepsilon_e}(s)$ remains constant in the low frequency range. This is because $\frac{\partial C_e}{\partial \varepsilon_e}$ does not contain a pole at s=0 as $\frac{\partial C_{se}}{\partial \varepsilon_s}(s)$ does. The reason is attributed to the fundamental difference between the lithium diffusion in the solid phase through a spherical particle and that in the electrolyte phase along a straight line. Specifically, the spherical diffusion is cumulative as lithium ion will accumulate in the particle over time (indicated by the pole at s=0 as an integrator), while the electrolyte diffusion is conservative as the total amount of lithium in the electrolyte remains constant. The sensitivity derivation of separator porosity $\varepsilon_{e,sep}$ is similar to that of ε_e.

2.4 Verification of analytic derivation

In this section, the derived analytic sensitivity expressions will be verified for the solid-phase diffusion coefficient D_s, active material volume fraction ε_s, reaction rate constant k, electrolyte diffusion coefficient D_e, and porosities ε_e and $\varepsilon_{e,sep}$ against the exact sensitivity obtained from numerical simulation of a full order P2D model. The verification is performed under three different types of current profiles, namely the constant-current (CC) discharging profiles, pulse profile, and a drive cycle, i.e. the Federal Urban Driving Schedule (FUDS). Under CC discharging, the battery initial SOC is set to 100%, and a constant current is applied to deplete the battery towards a final SOC of 0%.

Simulation is repeated under 1-3 C constant current with the purpose of verifying the sensitivity over the whole SOC range under different current rates. Under FUDS simulation, battery is initialized to 70% SOC and then subject to the dynamic current profile shown in Fig. 2.7a. The pulse and FUDS tests are intended to verify the dynamics of sensitivity under varying input. During the pulse current simulation shown in Fig. 2.7b, battery is initialized to 50% SOC and then cycled under alternating 1 C charging and discharging pulses, each of which lasts for 30 s and repeats over time. The model parameters used in simulation are adopted from [55], and Fig. 2.8 shows the open circuit potential (OCP) slope of the cathode, of which the parameter sensitivity will be verified.

2.4.1 Numerical simulation of exact sensitivity based on full order P2D model

The sensitivity calculated based on the derived analytical expressions will be compared with the numerical simulation based on the full order P2D model from which the SPMe was

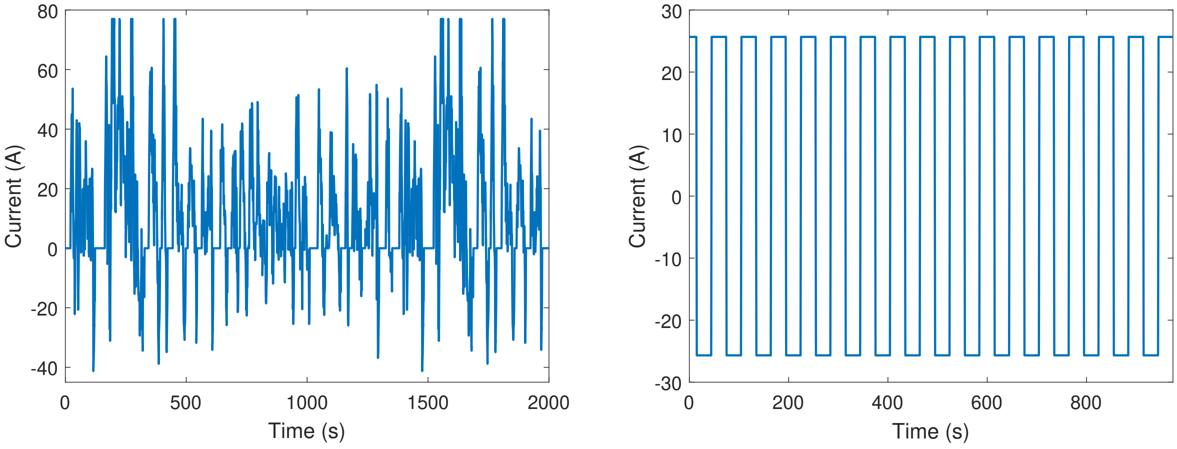

(a) (b)

Figure 2.7: (a) FUDS current profile; (b) Pulse current profile.

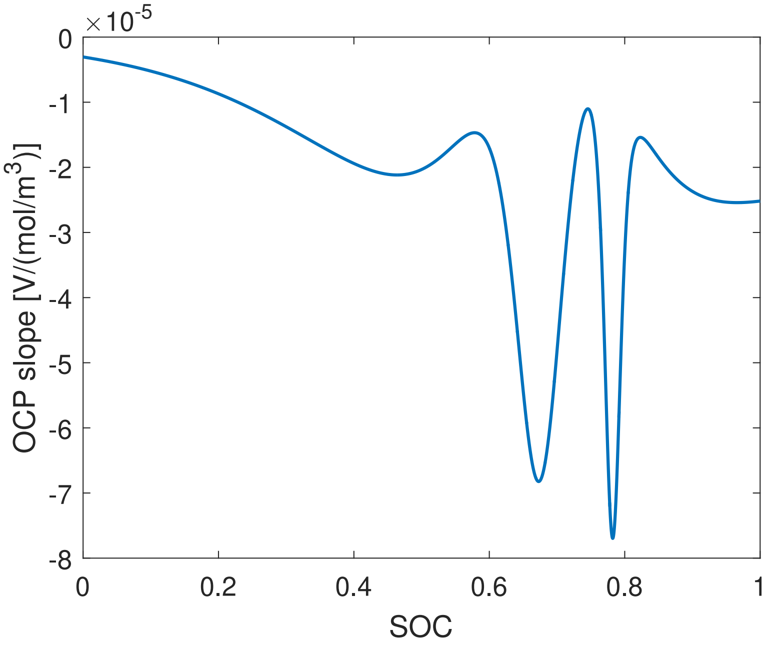

Figure 2.8: OCP slope of cathode

derived previously in this chapter. The P2D model-based simulation is performed by solving the Sensitivity Differential Algebraic Equations (SDAEs) derived from the full order model in [16, 60]. Specifically, the PDEs are first discretized spatially using the finite difference method or Padé approximation to formulate a system of continuous Differential Algebraic

Equations (DAEs),

$$\begin{aligned}\dot{\mathbf{X}} &= \mathbf{f}\left(\mathbf{X},\mathbf{Z},u,\lambda\right)\\ 0 &= \mathbf{g}\left(\mathbf{X},\mathbf{Z},u,\lambda\right)\\ y &= h\left(\mathbf{X},\mathbf{Z},u,\lambda\right)\end{aligned} \tag{2.48}$$

where $\mathbf{X} = \left[\mathbf{c_s},\mathbf{c_e}\right]^T \in \mathbb{R}^{n_\mathbf{X}}$ denotes the state variables with $\mathbf{c_s}$ and $\mathbf{c_e}$ being the spatially discretized state vectors, $\mathbf{Z} = \left[\phi_\mathbf{s},\mathbf{i_e},\phi_\mathbf{e},\mathbf{j}^{Li}\right]^T \in \mathbb{R}^{n_\mathbf{Z}}$ represents the discretized algebraic states, $u = I\left(t\right)$ is the model input, and $y = V\left(t\right)$ is the voltage output. In addition, $\lambda = \left[D_s, D_e, \varepsilon_s, \varepsilon_e, k\right] \in \mathbb{R}^{n_p}$ denotes the target parameters for sensitivity analysis.

The SDAEs can then be formulated by taking the partial derivative of Eqn. (2.48) to the target parameters λ [61],

$$\begin{aligned}\dot{\mathbf{X}}_\lambda &= \mathbf{f_X}\mathbf{X}_\lambda + \mathbf{f_z}\mathbf{Z}_\lambda + \mathbf{f}_\lambda\\ 0 &= \mathbf{g_X}\mathbf{X}_\lambda + \mathbf{g_Z}\mathbf{Z}_\lambda + \mathbf{g}_\lambda\\ y_\lambda &= h_\mathbf{X}\mathbf{X}_\lambda + h_\mathbf{Z}\mathbf{Z}_\lambda + h_\lambda\end{aligned} \tag{2.49}$$

where $\mathbf{X}_\lambda = \frac{\partial \mathbf{X}}{\partial \lambda} \in \mathbb{R}^{n_\mathbf{X} \times n_p}$, $\mathbf{Z}_\lambda = \frac{\partial \mathbf{Z}}{\partial \lambda} \in \mathbb{R}^{n_\mathbf{Z} \times n_p}$, $y_\lambda = \frac{\partial y}{\partial \lambda} \in \mathbb{R}^{n_p}$, and $\mathbf{f_X} = \frac{\partial \mathbf{f}}{\partial \mathbf{X}} \in \mathbb{R}^{n_\mathbf{X} \times n_\mathbf{X}}$, $\mathbf{f_Z} = \frac{\partial \mathbf{f}}{\partial \mathbf{Z}} \in \mathbb{R}^{n_\mathbf{X} \times n_\mathbf{Z}}$,and $\mathbf{f}_\lambda = \frac{\partial \mathbf{f}}{\partial \lambda} \in \mathbb{R}^{n_X \times n_p}$ are the Jacobian matrices of f with respect to $\mathbf{X}$, $\mathbf{Z}$, and λ respectively. Similarly, the Jacobian matrices of the functions $\mathbf{g}$ and h with respect to $\mathbf{X}$, $\mathbf{Z}$, and λ are represented by $\mathbf{g_X}$, $\mathbf{g_Z}$, $\mathbf{g}_\lambda$, $h_\mathbf{X}$, $h_\mathbf{Z}$, and h_λ respectively.

Solving the DAE system in Eqn. (2.48) and (2.49) could render the exact parameter sensitivity y_λ, but is subject to significant computation complexity as the total number of equations is typically in the order of hundreds depending on the number of discretization. A simulation platform has been developed to solve the DAE system by integrating the open source software CasADi [62], which calculates the Jacobians using automatic differentiation, and the SUNDIAL IDA solver [63], which solves the resultant DAEs and SDAEs. More details can be found in [60].

2.4.2 Verification of sensitivity for solid-phase diffusion coefficient D_s

The verification results for the cathode diffusion coefficient $D_{s,p}$ are presented in Fig. 2.9a - 2.9d. All sensitivity results have been normalized by multiplying with the nominal value of the parameter. It is seen that in all cases, the analytic derivation matches well with the P2D simulation.

Fig. 2.9a - 2.9d demonstrate the verification results under CC discharging, among which Fig. 2.9a shows the state sensitivity $\frac{\partial c_{se,p}}{\partial D_{s,p}}$ and Fig. 2.9b presents the voltage sensitivity $\frac{\partial V}{\partial D_{s,p}}$. The time duration is normalized to [0, 1] so that the 3 discharging cases can be presented over the same scale. Under CC discharging, the magnitude of $\frac{\partial c_{se,p}}{\partial D_{s,p}}$ sees significant increase for the first 250 seconds before reaching steady state. As shown in Fig. 2.9a, the analytic STF derived in Eqn. (2.30) characterizes both the transient and steady state and match the P2D simulation results very well (which is the average $\frac{\partial c_{se,p}}{\partial D_{s,p}}$ over the electrode). The resultant voltage sensitivity, $\frac{\partial V}{\partial D_{s,p}}$, is plotted in Fig. 2.9b, and shows good match between the analytic derivation and P2D simulation. The evolution of $\frac{\partial V}{\partial D_{s,p}}$ over time exhibits a "double-peak" trend, which is similar to the profile of the open circuit potential slope $\frac{\partial U_p}{\partial c_{se,p}}$ shown in Fig. 2.8, because $\frac{\partial V}{\partial D_{s,p}}$ is dominated by the product of $\frac{\partial c_{se,p}}{\partial D_{s,p}}$ and $\frac{\partial U_p}{\partial c_{se,p}}$. Some discrepancies can be observed, which are attributed to the development of c_s gradient across the electrode neglected by the single particle assumption. The discrepancies are minimal under 1 C current and increase under higher current due to more prominent concentration gradient. It is noted that such discrepancies are not seen in $\frac{\partial c_{se,p}}{\partial D_{s,p}}$ because Fig. 2.9a shows the average $\frac{\partial c_{se,p}}{\partial D_{s,p}}$ over the electrode.

Fig. 2.9c demonstrates the verification results under the pulse current, in which the sensitivity fluctuates as the current changes direction periodically. The analytic derivation matches almost perfectly with P2D simulation because the lithium concentration gradient would not build up during fast transient. Fig. 2.9d demonstrates the results under the FUDS drive cycle. It is seen that the voltage sensitivity of D_s varies significantly under real-world operation as some data segments are highly sensitive/insensitive to D_s compared to others. By correlating to the results under CC discharging, it is figured that high D_s sensitivity can be achieved under current patterns with high magnitude and adequate duration, which explains the two sensitivity peaks at around 250s and 1600s in Fig. 2.9d.

2.4.3 Sensitivity verification for active material volume fraction ε_s

The sensitivity verification results for the cathode active material volume fraction $\varepsilon_{s,p}$ are presented in Fig. 2.10a - 2.10d under the CC discharging, pulse current, and FUDS profiles respectively. It can be seen that in all these cases, the analytic results derived based on SPMe match well with those from numerical P2D simulation.

Furthermore, several interesting observations can be made. Under CC discharging, as seen in Fig. 2.10a, the magnitude of the state sensitivity $\frac{\partial c_{se,p}}{\partial \varepsilon_{s,p}}$ keeps increasing over time, as opposed to the previous $\frac{\partial c_{se}}{\partial D_s}$, which reaches a finite steady state. This is theoretically predicted by the derived sensitivity transfer function in Eqn. (2.39), which contains a pole at 0, representing the integration of current over time. The voltage sensitivity $\frac{\partial V}{\partial \varepsilon_s}$, as shown

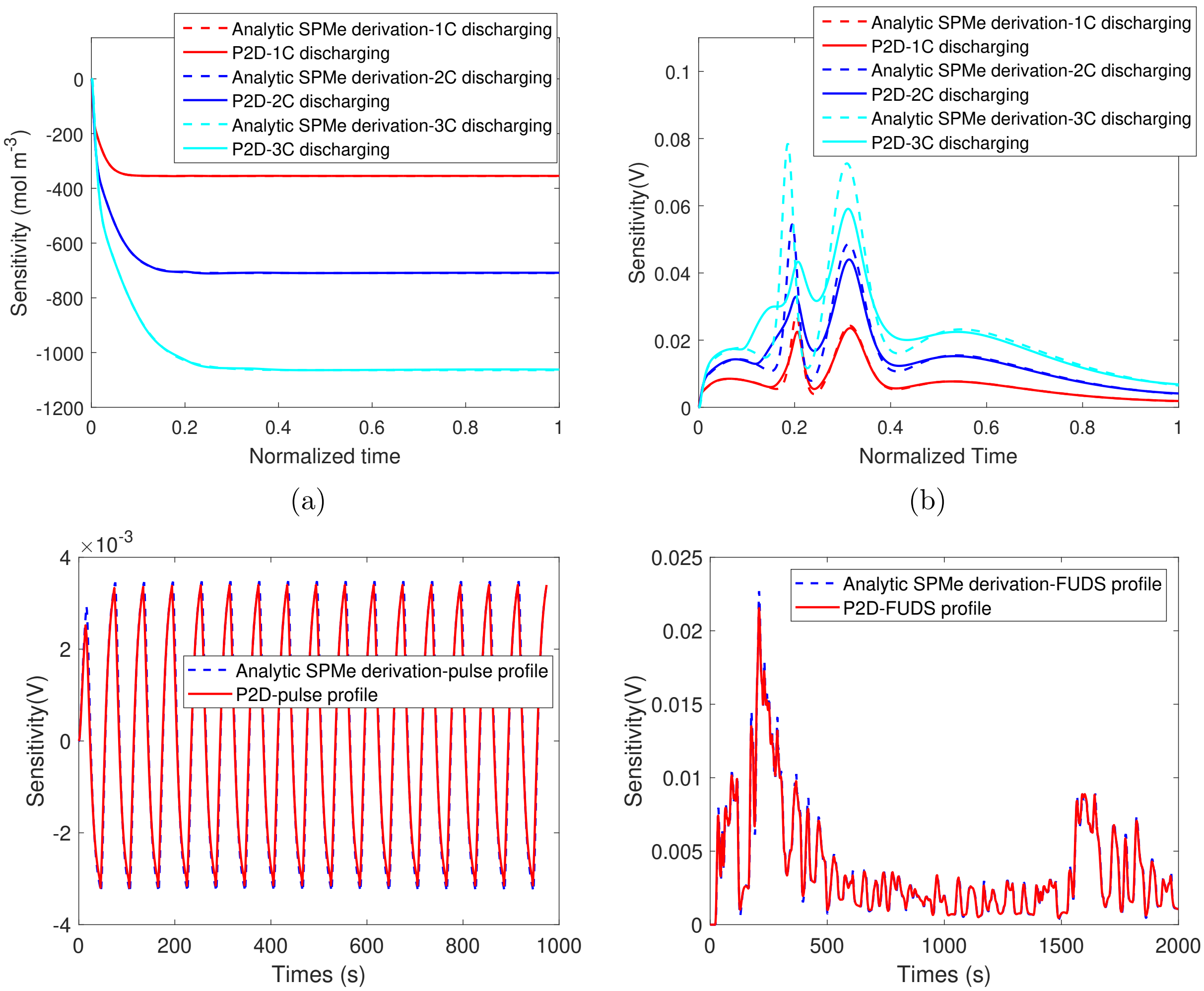

(a) (b) (c) (d)

Figure 2.9: (a) Normalized $\frac{\partial c_{se,p}}{\partial D_{s,p}}$ under CC discharging; (b) Normalized $\frac{\partial V}{\partial D_{s,p}}$ under CC discharging; (c) Normalized $\frac{\partial V}{\partial D_{s,p}}$ under pulse profile; (d) Normalized $\frac{\partial V}{\partial D_{s,p}}$ under FUDS.

in Fig. 2.10b, is dominated by the ever-increasing semi-linear dynamic term $\frac{\partial U_p}{\partial c_{se,p}} \cdot \frac{\partial c_{se,p}}{\partial \varepsilon_{s,p}}$, and hence shows the profile of the OCP slope. It is also interesting to note that the dependence of ε_s sensitivity on current magnitude is much weaker than that of D_s . The separation of the different terms of $\frac{\partial V}{\partial \varepsilon_s}$ can be observed more clearly from the pulse current simulation. As shown in Fig. 2.10c, the instantaneous jumps occurring at the periodic current switching indicates the non-dynamic terms $\frac{\partial \eta}{\partial a_{s,p}} \frac{\partial a_{s,p}}{\partial \varepsilon_{s,p}}$ and $\frac{\partial R_\Omega}{\partial \varepsilon_{s,p}}$, and the subsequent transient is dominated by the dynamic terms $(\frac{\partial U}{\partial c_{se}} + \frac{\partial \eta}{\partial c_{se}}) \cdot \frac{\partial c_{se}}{\partial \varepsilon_s}$. It is seen that the derived analytic expressions not only enable fast and efficient computation of sensitivity, but also provide theoretic insight and explanation which are unavailable from numerical simulation.

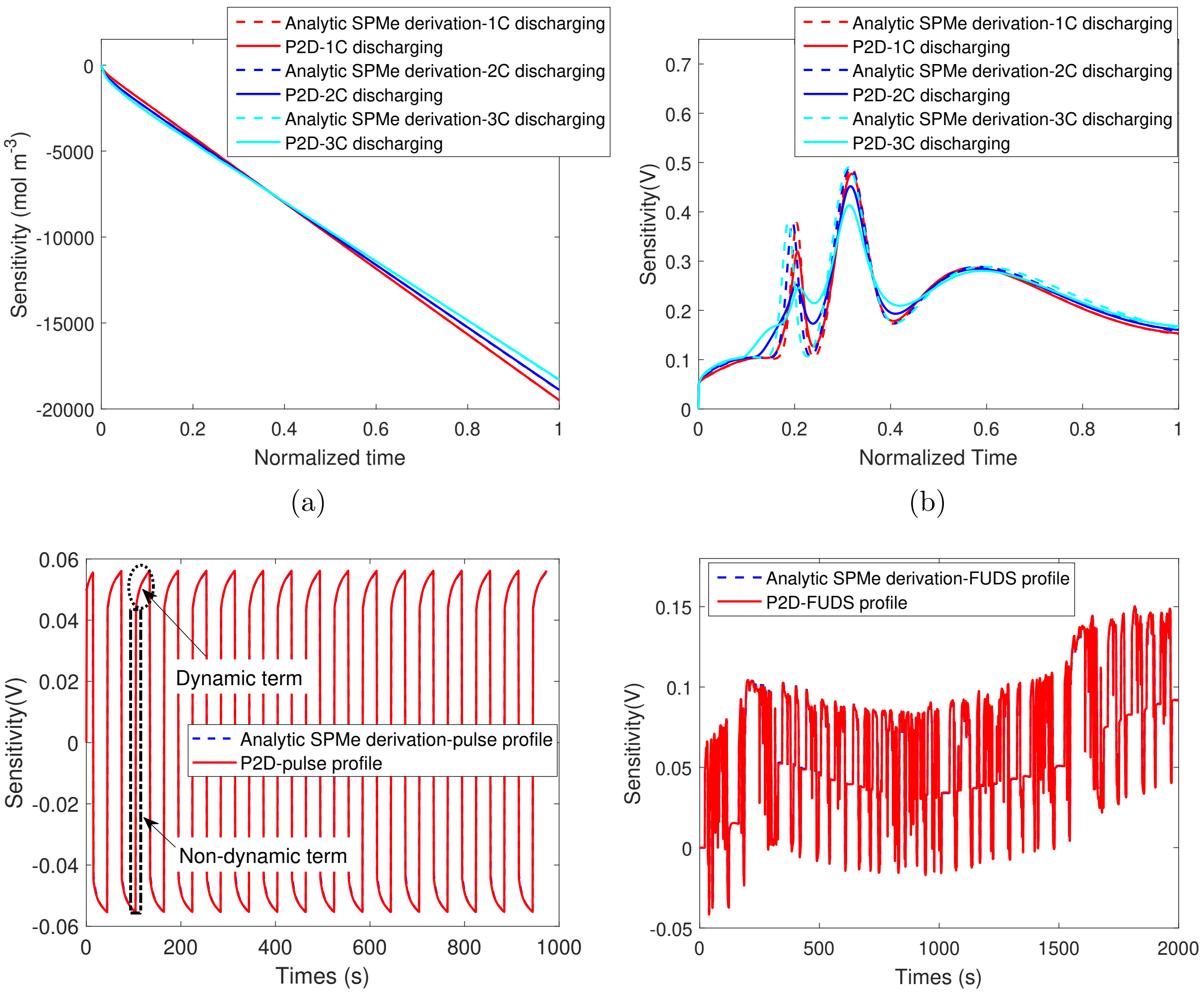

(a) (b)

(c) (d)

Figure 2.10: (a) Normalized $\frac{\partial c_{se,p}}{\partial \varepsilon_{s,p}}$ under CC discharging; (b) Normalized $\frac{\partial V}{\partial \varepsilon_{s,p}}$ under CC discharging; (c) Normalized $\frac{\partial V}{\partial \varepsilon_{s,p}}$ under pulse profile; (d) Normalized $\frac{\partial V}{\partial \varepsilon_{s,p}}$ under FUDS.

2.4.4 Verification of sensitivity for reaction rate constant k

The verification results for the reaction rate constant k are presented in Fig. 2.11a - 2.11c. It can be seen that the analytic sensitivity derived based on SPMe matches well with the P2D numerical simulation under all current profiles.

The parameter k affects the battery voltage through the overpotential η, and its sensitivity $\frac{\partial V}{\partial k}$ has been shown in Eqn. (2.41) as a nonlinear function of the input current I. Therefore, it is seen that the sensitivity of k evolves over time in similar patterns as the current variation under all profiles. In addition, the dependence of $\frac{\partial V}{\partial k}$ on lithium concentration (through the exchange current i_0) is minimal (at least under the given battery parameters considered in this paper), which makes $\frac{\partial V}{\partial k}$ remain constant over time under constant current.

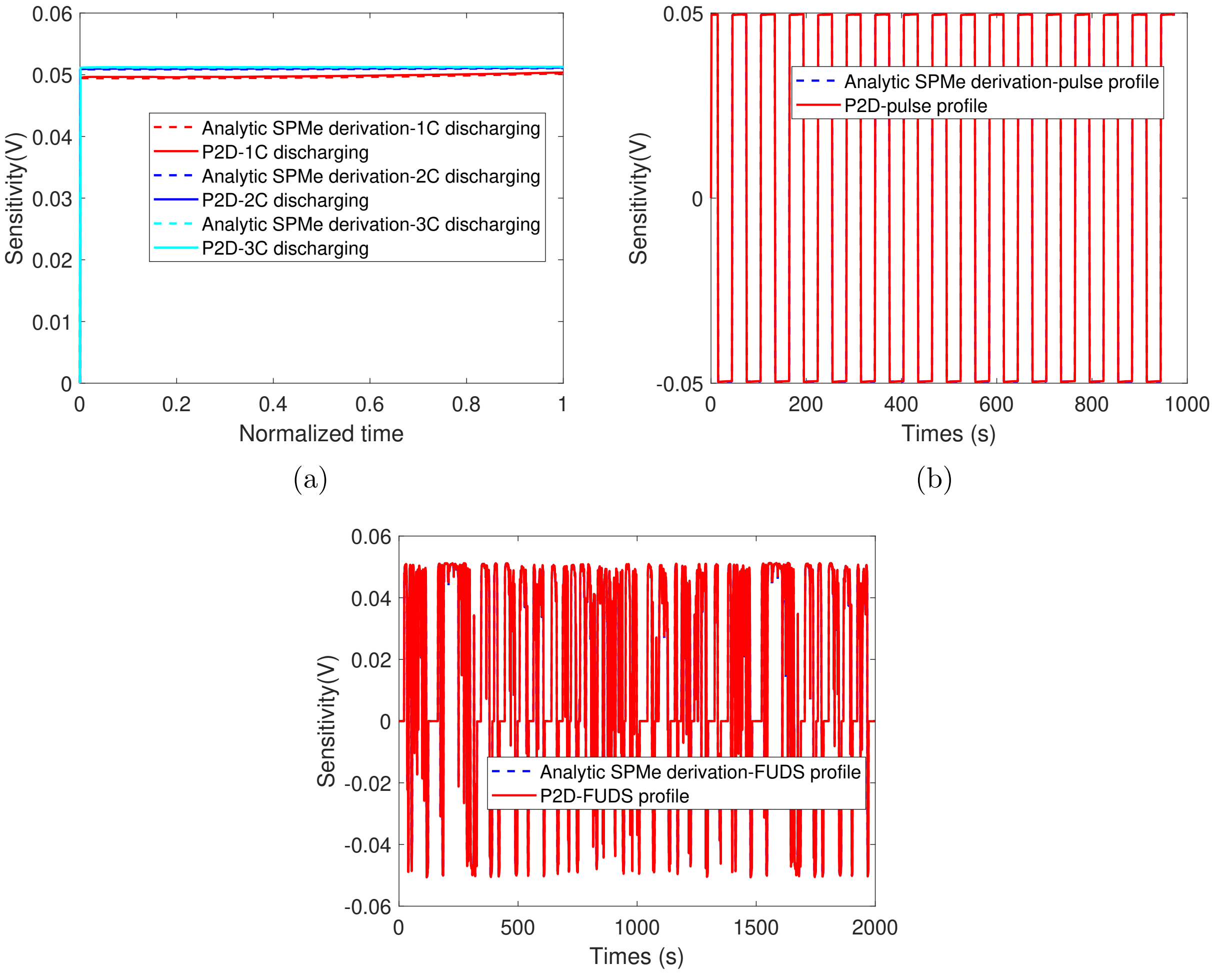

(a)

(b)

(c)

Figure 2.11: (a) Normalized $\frac{\partial V}{\partial k_p}$ under CC discharging; (b) Normalized $\frac{\partial V}{\partial k_p}$ under pulse profile; (c) Normalized $\frac{\partial V}{\partial k_p}$ under FUDS .

2.4.5 Verification of sensitivity for electrolyte diffusion coefficient D_e

The verification results for the electrolyte diffusion coefficient D_e are presented in Fig. 2.12a - 2.12d.

Fig. 2.12a shows the evolution of the state sensitivity $\frac{\partial c_{e,p}}{\partial D_e}$ under CC discharging. According to the derived STF in Eqn. (2.43), the dynamics of $\frac{\partial c_{e,p}}{\partial D_e}$ feature a stable second order transfer function. Accordingly, it is shown in Fig. 2.12a that the sensitivity reaches a constant value after the initial transient. The analytic derivation based on SPMe matches fairly well with the numerical sensitivity from P2D simulation. Fig. 2.12b compares the voltage sensitivity $\frac{\partial V}{\partial D_e}$ under CC discharging profiles. It is seen that the mismatch between the analytic results based on SPMe and those from P2D simulation becomes more prominent. Nevertheless, the analytic results derived based on SPMe could match the exact sensitivity (from P2D simulation) well under low current and capture the main trend and feature under high current. Fig. 2.12c and Fig. 2.12d demonstrate the comparison of normalized $\frac{\partial V}{\partial D_e}$ under pulse and FUDS profiles, showing similar results. Under the FUDS profile, similar to the sensitivity results of D_s in Fig. 2.9d, the two peaks of high sensitivity are achieved under high magnitude current with adequate duration.

It is noted that the derived analytic sensitivity based on SPMe for D_e (and also the subsequent ε_e) in general does not match the P2D simulation as well as the electrode parameters D_s and ε_s. There are two possible model simplification steps involving the electrolyte submodel that may have led to the deviation/errors. The first one is the single particle assumption, which neglects the non-uniform distribution of the current density j^{Li} across the electrode in Eqn. (2.8), and the second one is the Pade approximation, which reduces the transcendental transfer function of the electrolyte concentration c_e to a 1st order rational transfer function. The main source of error can be identified as the first one, i.e. single particle assumption, since it is shown in Fig. 2.5 and 2.6 that the 1st order Pade approximation matches well with the transcendental transfer function. The main reason for the larger deviation under the single particle assumption for the electrolyte submodel is that the uniform-current-density approximation affects both the source term and the boundary conditions of the electrolyte diffusion in Eqn. (2.8). In order to mitigate the deviation, other methods of model reduction can be used to simplify the original full order model without relying on the single particle assumption, such as the balanced truncation, proper orthogonal decomposition (POD), and the Galerkin method among others [64]. However, these methods are too complicated and/or non-analytical, and hence make it impossible/difficult to further derive the parameter sensitivity, suggesting an interesting topic for future research.

2.4.6 Verification of sensitivity for electrode porosity ε_e

The verification results for the electrode porosity ε_e are presented in Fig. 2.13a - 2.13d.

The state sensitivity $\frac{\partial c_{e,p}}{\partial \varepsilon_e}$ at the cathode boundary ($x = L_c$) under CC discharging is shown in Fig. 2.13a, which can be approximated well by the second order STF derived based on SPMe under low current, e.g. 1 C. The mismatch becomes prominent under higher C rates due to the aforementioned assumption and approximation of the electrolyte model. Fig. 2.13b shows similar results for the voltage sensitivity $\frac{\partial V}{\partial \varepsilon_e}$. According to Eqn. (2.36), ε_e affects the terminal voltage through two terms, i.e. the linear non-dynamic electrolyte ohmic polarization $\phi_{e,\Omega}$ and the semi-linear dynamic concentration polarization $\Delta\phi_{e,con}$. The

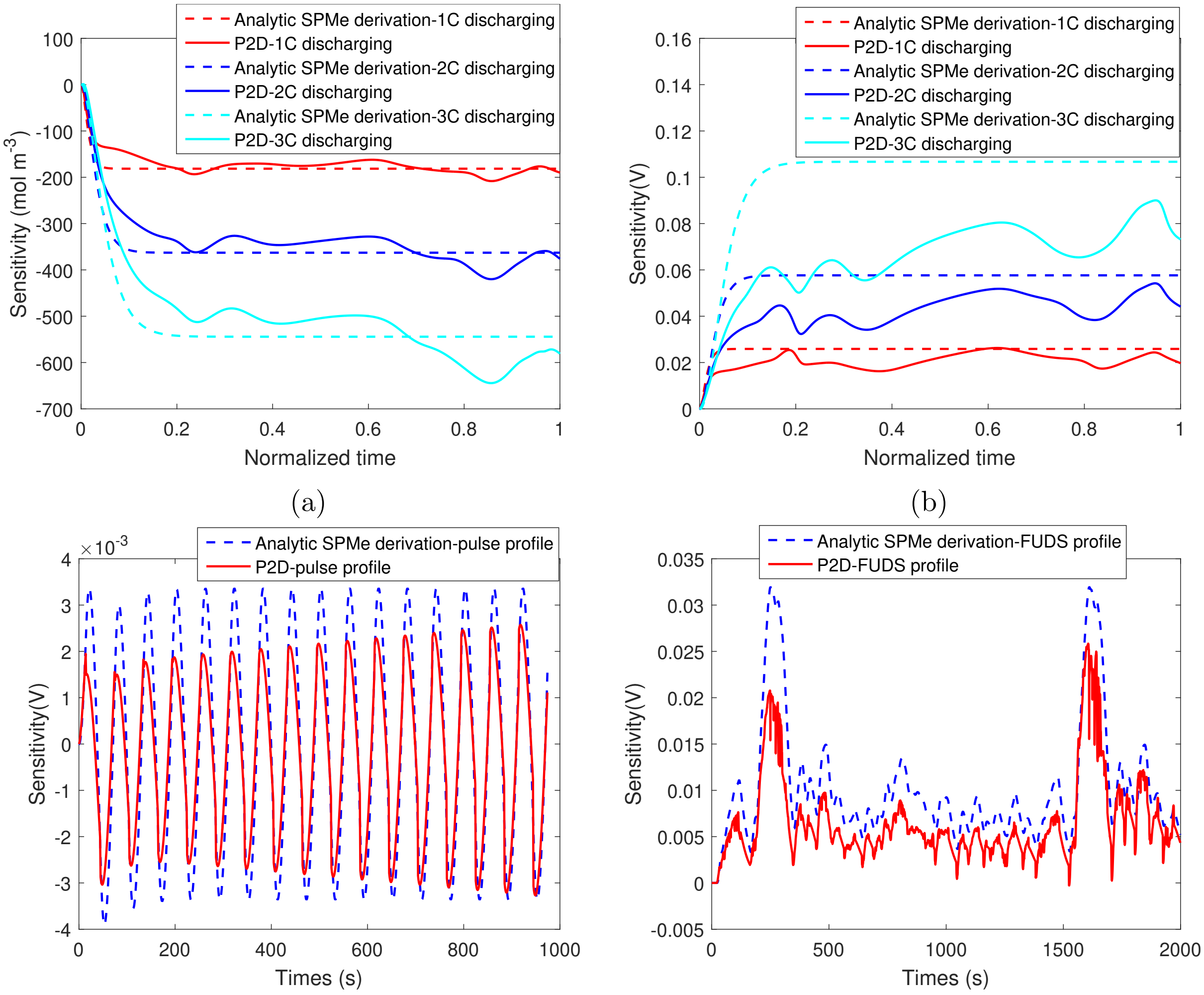

(a) (b) (c) (d)

Figure 2.12: (a) Normalized $\frac{\partial c_{e,p}}{\partial D_e}$ under CC discharging; (b) Normalized $\frac{\partial V}{\partial D_e}$ under CC discharging; (c) Normalized $\frac{\partial V}{\partial D_e}$ under pulse profile; (d) Normalized $\frac{\partial V}{\partial D_e}$ under FUDS.

effects of these two terms are clearly distinguishable under the pulse current shown in Fig. 2.13c. The instantaneous jump, which occurs every time when current switches direction, corresponds to the Ohmic polarization term, and the subsequent transient indicates the concentration polarization. The results under dynamic current profiles shown in Fig. 2.13c and Fig. 2.13d are similar to those under CC discharging, as the analytic sensitivity derived based on SPMe captures the main trend and features of the numerical sensitivity from P2D simulation while sees discrepancy especially under high current.

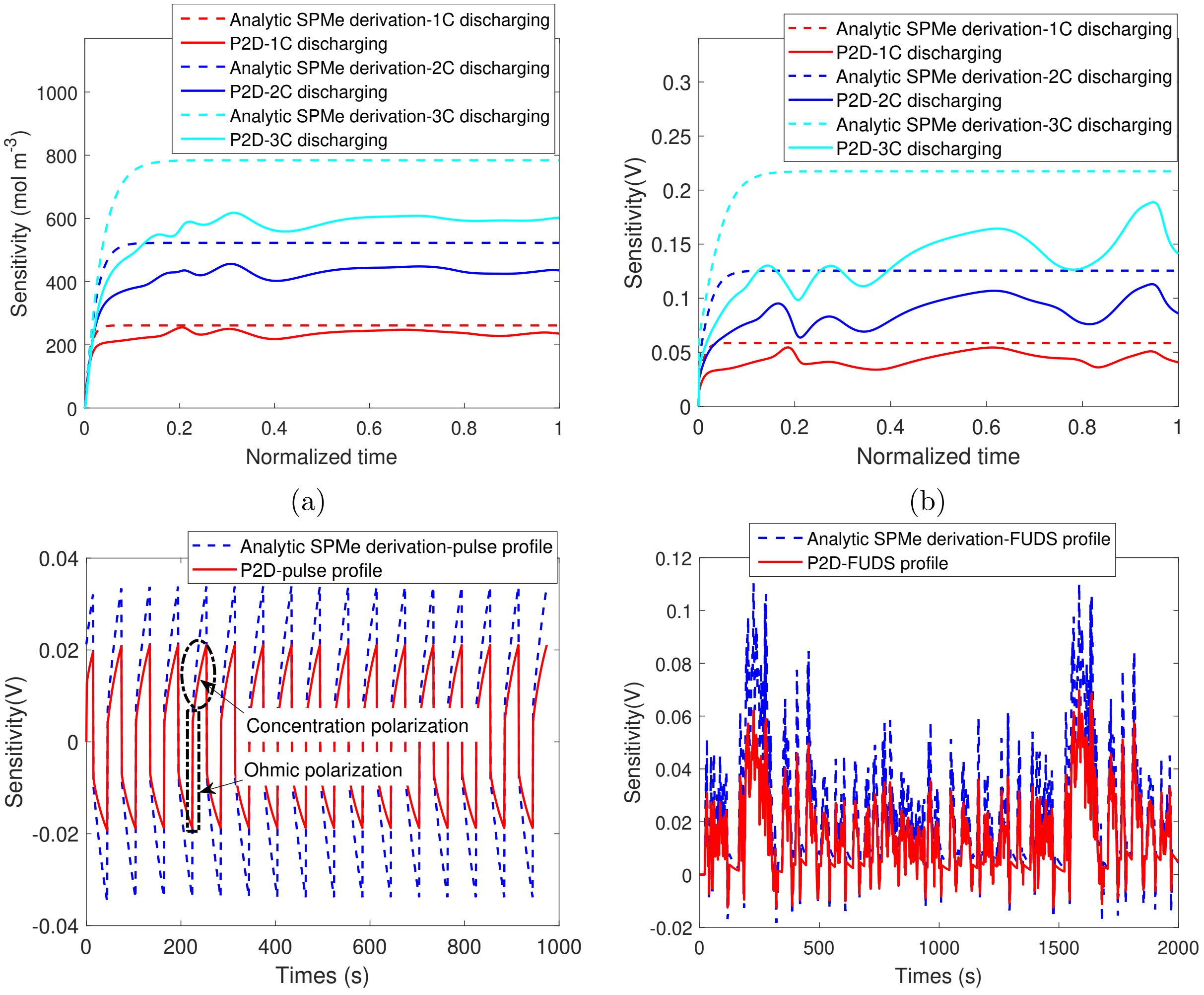

(a) (b)

(c) (d)

Figure 2.13: (a) Normalized $\frac{\partial c_{e,p}}{\partial \varepsilon_e}$ under CC discharging; (b) Normalized $\frac{\partial V}{\partial \varepsilon_e}$ under CC discharging; (c) Normalized $\frac{\partial V}{\partial \varepsilon_e}$ under pulse profile; (d) Normalized $\frac{\partial V}{\partial \varepsilon_e}$ under FUDS.

2.4.7 Verification of sensitivity for separator porosity $\varepsilon_{e,sep}$

The dynamics of the sensitivity of the separator porosity $\varepsilon_{e,sep}$ are similar to those of the electrode porosity ε_e as shown in Fig. 2.14a - 2.14d. However, it is noted that the SPMe results match the P2D simulation much better than in the case of ε_e, which can be explained by two reasons. First, the intercalation current density is zero in the separator due to the absence of intercalation reaction, and hence the electrolyte diffusion dynamics do not suffer from the uniform current density assumption. Second, the separator only accounts for a small portion of the total volume of the battery (e.g. 11% under the given parameters considered in this paper). Therefore, the lithium ion concentration gradient would not build up significantly across the separator. Meanwhile, since the volume of the separator is much smaller than that of the electrodes, the sensitivity of $\varepsilon_{e,sep}$ is also much smaller in magnitude than that of ε_e.

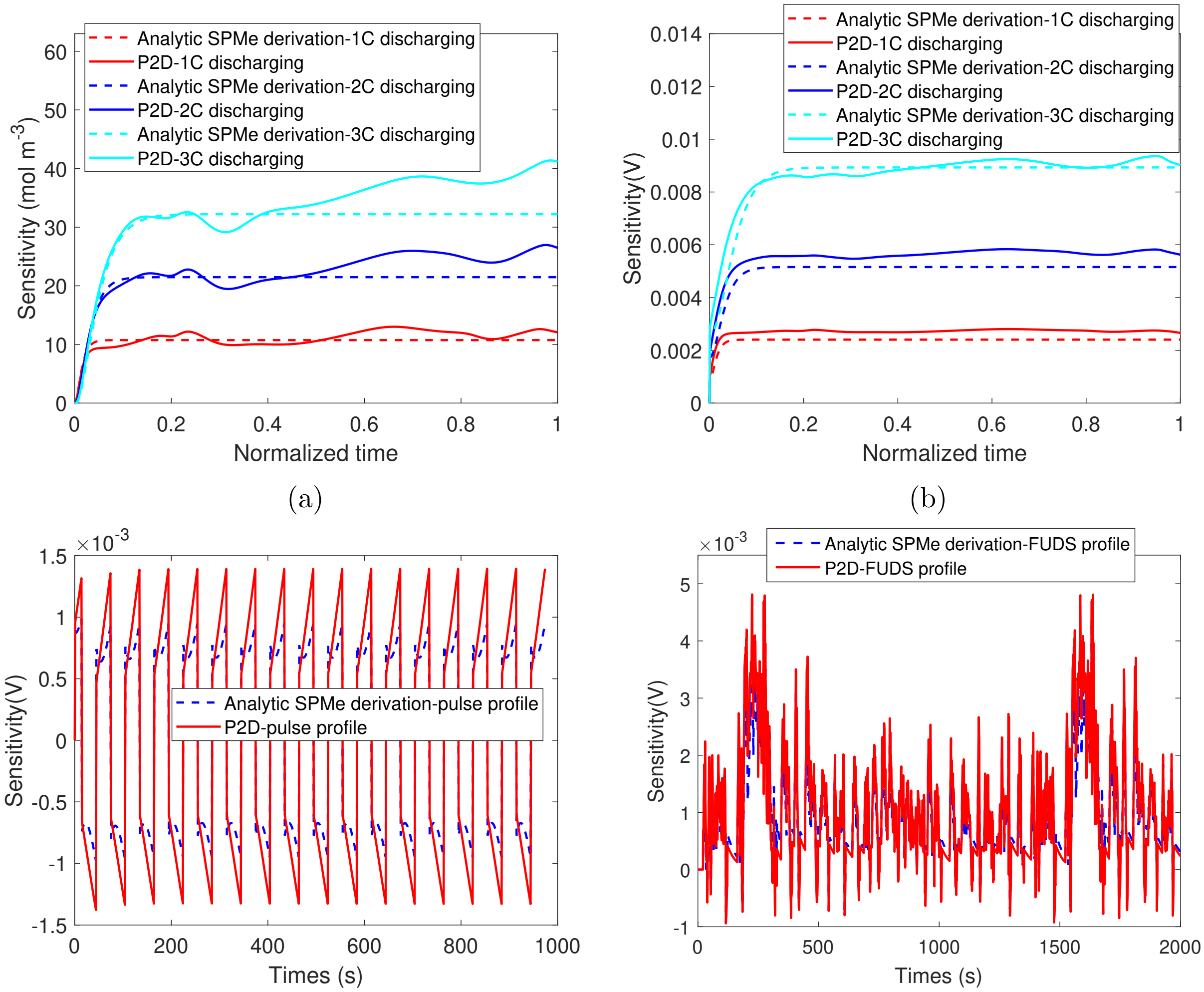

(a) (b) (c) (d)

Figure 2.14: (a) Normalized $\frac{\partial c_{e,p}}{\partial \varepsilon_{e,sep}}$ under CC discharging; (b) Normalized $\frac{\partial V}{\partial \varepsilon_{e,sep}}$ under CC discharging; (c) Normalized $\frac{\partial V}{\partial \varepsilon_{e,sep}}$ under pulse profile; (d) Normalized $\frac{\partial V}{\partial \varepsilon_{e,sep}}$ under FUDS.

Chapter 3

New Data Optimization Methodology for Parameter Estimation under Uncertainties

This chapter aims at establishing new criteria and a novel methodology for data optimization and estimation error quantification to overcome the fundamental limitations of the conventional input/experiment design approach. First, a generic formula is derived for quantifying the estimation error subject to sensor, model, and parameter uncertainties for the commonly used least-squares algorithm. Based on the formula, desirable data structures, which could minimize the errors caused by each uncertainty, are identified. These structures are then used as new criteria to formulate the novel data optimization methodology. For validation purpose, the proposed methodology, leveraging the parameter sensitivity expressions derived in Chapter 2, is applied to the single-variate estimation problem of a lithium-ion battery electrochemical model in simulation and experiments. The results show up to two orders of magnitude improvement in estimation accuracy compared with the traditional Fisher-information-based approach and other baselines.

3.1 Derivation of new formula for quantifying estimation error under uncertainties

In this section, a formula which quantifies the parameter estimation error for the least squares method is derived. To the best of our knowledge, this formula is the first one capable of systematically predicting the estimation errors caused by uncertainties in measurement, model, and parameters, which enables the identification of desirable data structures for improving estimation accuracy.

Consider a generic discrete-time dynamic system described by

$$\begin{aligned} x_k &= f_k(x_{k-1}, \boldsymbol{\theta}, u_{k-1}) \\ y_k &= g_k(x_k, \boldsymbol{\theta}, u_k), \end{aligned} \tag{3.1}$$

where $\boldsymbol{\theta} = [\theta_1, \theta_2, \ldots, \theta_n]$ are the constant model parameters, u is the input, x are the states, and y is the output. Here we consider single-input-single-output systems with scalar u and y, but the analysis can be generalized to multi input and output systems. Suppose we want to estimate one parameter θ_1 based on a sequence of N input data and the resultant output data

$$\boldsymbol{y^m} = [y_1^m, y_2^m, \ldots, y_N^m], \tag{3.2}$$

where y^m denotes the measured output value,

$$y_k^m = y_k(\boldsymbol{\theta}, u) + \mathit{\Delta} y + \delta y_k. \tag{3.3}$$

In Eqn. (3.3), y_k represents the output predicted by the model in Eqn. (3.1) based on the true parameter $\boldsymbol{\theta}$, $\mathit{\Delta} y$ stands for the constant mismatch between y_k and the true system output including both model and measurement bias, and δy_k denotes the time-varying uncertainty in model and measurement. The least-squares estimation problem is then formulated as

$$\min_{\hat{\theta}_1} J = \frac{1}{2}\sum_{k=1}^{N}\left(y_k^m(\boldsymbol{\theta}, u) - \hat{y}_k(\hat{\boldsymbol{\theta}}, u)\right)^2, \tag{3.4}$$

where $\hat{y}_k(\hat{\boldsymbol{\theta}}, u)$ is the model output based on the estimated (or assumed) parameter value $\hat{\boldsymbol{\theta}}$,

$$\hat{\boldsymbol{\theta}} = \left[\hat{\theta}_1, \hat{\theta}_2, \ldots, \hat{\theta}_n\right]. \tag{3.5}$$

It is noted that $\hat{\theta}_1$ is the estimate of the target variable by solving Eqn. (3.4), while $\hat{\theta}_2, \ldots, \hat{\theta}_n$ represent the assumed values for other parameters with uncertainty.

The estimate $\hat{\theta}_1$ can be found based on the first-order optimality condition $\frac{\partial J}{\partial \hat{\theta}_1} = 0$, as

$$\sum_{k=1}^{N} \left(y_k^m - \hat{y}_k\right) \frac{\partial\left(y_k^m - \hat{y}_k\right)}{\partial \hat{\theta}_1} = 0, \tag{3.6}$$

with

$$y_k^m - \hat{y}_k = y_k(\boldsymbol{\theta}, u_k) + \mathit{\Delta} y + \delta y_k - y_k(\hat{\boldsymbol{\theta}}, u_k). \tag{3.7}$$

By taking the first-order Taylor expansion about $\hat{\boldsymbol{\theta}}$, Eqn. (3.7) can be expanded as

$$\begin{aligned} y_k^m - \hat{y}_k &\approx \frac{\partial y_k}{\partial \boldsymbol{\theta}}(\hat{\boldsymbol{\theta}})\Delta\boldsymbol{\theta} + \mathit{\Delta} y + \delta y_k \\ &= \frac{\partial y_k}{\partial \theta_1}(\hat{\boldsymbol{\theta}})\Delta\theta_1 + \cdots + \frac{\partial y_k}{\partial \theta_n}(\hat{\boldsymbol{\theta}})\Delta\theta_n + \mathit{\Delta} y + \delta y_k, \end{aligned} \tag{3.8}$$

where $\mathit{\Delta}\theta_1 = \theta_1 - \hat{\theta}_1$ represents the estimation error in θ_1, $\mathit{\Delta}\theta_2 = \theta_2 - \hat{\theta}_2, \ldots,$ $\mathit{\Delta}\theta_n = \theta_n - \hat{\theta}_n$ denote the mismatch/uncertainty in other parameters, and $\frac{\partial y_k}{\partial \theta_i}(\hat{\boldsymbol{\theta}})$ is the output sensitivity of parameter θ_i (evaluated at $\hat{\boldsymbol{\theta}}$). Then, by taking the partial derivative of Eqn. (3.7) to $\hat{\theta}_1$, we have

$$\frac{\partial\left(y_k^m - \hat{y}_k\right)}{\partial \hat{\theta}_1} = -\frac{\partial y_k}{\partial \theta_1}(\hat{\boldsymbol{\theta}}). \tag{3.9}$$

Finally, by substituting Eqn. (3.8) and (3.9) into (3.6) and reformulating, an expression for the estimation error $\Delta\theta_1$ can be obtained as Eqn. (3.10),

$$\varDelta\theta_1 = -\frac{\left(\sum\limits_{k=1}^{N} \frac{\partial y_k}{\partial\hat{\theta}_1}\right)\varDelta y + \left(\sum\limits_{k=1}^{N} \frac{\partial y_k}{\partial\hat{\theta}_1}\delta y_k\right) + \left(\sum\limits_{k=1}^{N} \frac{\partial y_k}{\partial\hat{\theta}_2}\frac{\partial y_k}{\partial\hat{\theta}_1}\right)\varDelta\theta_2 + \cdots + \left(\sum\limits_{k=1}^{N} \frac{\partial y_k}{\partial\hat{\theta}_n}\frac{\partial y_k}{\partial\hat{\theta}_1})\right)\varDelta\theta_n}{\sum\limits_{k=1}^{N}\left(\frac{\partial y_k}{\partial\hat{\theta}_1}\right)^2} \tag{3.10}$$

where $\frac{\partial y_k}{\partial\hat{\theta}_i} = \frac{\partial y_k}{\partial\theta_i}(\hat{\boldsymbol{\theta}})$ and $i = 1, 2, \cdots, n$. Eqn. (3.10) quantifies the error induced by constant model/measurement uncertainty Δy_k, varying model/measurement uncertainty δy_k, and uncertainty in other parameters $\Delta\theta_2, \ldots, \Delta\theta_n$.

Several important insights on estimation errors can be made from Eqn. (3.10) as follows.

1. The denominator, $\sum_{k=1}^{N}\left(\frac{\partial y_k}{\partial\theta_1}\right)^2$, is essentially the Fisher information of the target variable θ_1 (simplified under i.i.d. Gaussian noise) [65, 66], which has been the predominantly used objective for data optimization [16, 67]. Eqn. (3.10) establishes the direct link between Fisher information and estimation error, and is more intuitive and applicable than the restrictive Cramér-Rao Bound interpretation. It is interesting to note that, on one hand, maximizing Fisher information could indeed reduce the estimation error by increasing the denominator; on the other, Fisher information is only part of the formula as the numerator terms also have major impacts.

2. The first term in the numerator, $\left(\sum_{k}^{N}\frac{\partial y_k}{\partial\theta_1}\right)\varDelta y$, represents the estimation error caused by constant model/measurement uncertainty Δy. It shows that such error can be eradicated by making $\sum_{k}^{N}\frac{\partial y_k}{\partial\theta_1} = 0$, i.e. zero sum of sensitivity of θ_1 over the whole data sequence. This finding indicates the fundamental data structure for improving estimation accuracy under constant model/measurement bias, which has not been es-

tablished in literature before our work. It is noted that there is a tradeoff between minimizing this term and maximizing the Fisher information (sensitivity magnitude), and both need to be considered in order to attain the best estimation accuracy. The new data optimization methodology to be demonstrated in Section 3.2 is formulated by exploiting such tradeoff. Similar tradeoff also applies to terms associated with other types of uncertainties to be discussed subsequently.

3. The second term in the numerator, $\sum_k^N \frac{\partial y_k}{\partial \theta_1} \delta y_k$, represents the estimation error caused by varying model/measurement uncertainty δy_k. This term is essentially the inner product of the sensitivity sequence vector $\frac{\partial \mathbf{y}}{\partial \theta_1} = [\frac{\partial y_1}{\partial \theta_1}, \frac{\partial y_2}{\partial \theta_1}, \ldots, \frac{\partial y_N}{\partial \theta_1}]^T$ with the uncertainty sequence vector $\delta \mathbf{y} = [\delta y_1, \delta y_2, \ldots, \delta y_N]^T$. It shows that the error can be eradicated by having $\sum_k^N \frac{\partial y_k}{\partial \theta_1} \delta y_k = 0$ or $\frac{\partial \mathbf{y}}{\partial \theta_1} \cdot \delta \mathbf{y} = 0$, i.e. making the sensitivity vector orthogonal to the uncertainty vector. This finding indicates the data structure for improving estimation accuracy under varying model/measurement uncertainty, which is also unexplored in literature.

4. The remaining terms in the numerator, $\left(\sum_k^N \frac{\partial y_k}{\partial \theta_i} \frac{\partial y_k}{\partial \theta_1}\right) \Delta\theta_i$, reflect the error caused by uncertainty in other parameters. The terms are essentially the inner product of the sensitivity vector of the target variable θ_1 with that of uncertain parameter θ_i times the amount of uncertainty $\Delta\theta_i$. The error can be eradicated by having $\sum_k^N \frac{\partial y_k}{\partial \theta_1} \frac{\partial y_k}{\partial \theta_i} = 0$ or $\frac{\partial \mathbf{y}}{\partial \theta_1} \cdot \frac{\partial \mathbf{y}}{\partial \theta_i} = 0$, i.e. making the sensitivity vector of the target parameter orthogonal to those of uncertain parameters. This finding is related to results on multivariate Cramér–Rao bound analysis in [66], which showed that data with orthogonal parameter sensitivity could reduce the error variance for joint estimation of two parameters. This

data structure is also a new one to be incorporated into data optimization.

The developed methodology in this section is also applicable to MIMO systems, in which the parameter sensitivity is driven by multiple inputs while different outputs will have different sensitivity dynamics. Specifically, for multiple-input (MI) systems, the data structures for rejecting uncertainties are the same, except that the sensitivity expression will be more complicated containing more terms with respect to multiple inputs. Therefore, the data optimization procedures will need to optimize multiple input sequences, resulting in a more complicated problem to solve. For multiple-output (MO) systems, the data structures for rejecting uncertainties need to be re-derived by reformulating the least squares cost function to incorporate multiple outputs and applying the first-order optimality condition. The derived data structures can then be used for new data optimization problem formulation.

3.2 New data optimization methodology

In this section, a new data optimization (or optimal experiment design) methodology is developed for parameter estimation with the goal of minimizing the errors caused by uncertainties in measurement, model, and parameters, based on the desirable data structures extracted from Eqn. (3.10). The methodology is built upon new problem formulations and efficient parameter sensitivity computation technique proposed in Chapter 2.

Traditionally, data optimization (or optimal experiment design) for parameter estimation is performed by maximizing the Fisher information [16, 67]. For single parameter estimation, the problem takes the form (assuming i.i.d. Gaussian noise),

$$\underset{\boldsymbol{u}}{Max}\sum_{k=1}^{N}\left(\frac{\partial y_k}{\partial \theta_1}(\boldsymbol{u},\hat{\boldsymbol{\theta}})\right)^2, \tag{3.11}$$

where the decision variables are the control input sequence $\boldsymbol{u} = [u_1, u_2, \cdots, u_N]^T$. It is noted that $\frac{\partial y_k}{\partial \theta_1}(\boldsymbol{u}, \hat{\boldsymbol{\theta}})$ denotes the sensitivity of θ_1 evaluated at certain *a priori* parameter values $\hat{\boldsymbol{\theta}}$, because sensitivity is parameter value dependent, and the exact parameter values are unknown for data optimization. As discussed previously, maximizing Fisher information could indeed reduce the error according to Eqn. (3.10), but this alone will not necessarily minimize the error as there are other desirable data structures that would contribute to error reduction as identified from the numerator of Eqn. (3.10).

For example, in the case of estimation subject to constant model/measurement bias Δy, a new optimization problem can be formulated as

$$\underset{\boldsymbol{u}}{Max} \sum_{k=1}^{N} \left(\frac{\partial y_k}{\partial \theta_1}(\boldsymbol{u}, \hat{\boldsymbol{\theta}}) \right)^2 - \alpha \left| \sum_{k=1}^{N} \frac{\partial y_k}{\partial \theta_1}(\boldsymbol{u}, \hat{\boldsymbol{\theta}}) \right|, \tag{3.12}$$

which, besides maximizing the Fisher information, adds a soft constraint to minimize the term $\left| \sum_k^N \frac{\partial y_k}{\partial \theta_1}(\boldsymbol{u}, \hat{\boldsymbol{\theta}}) \right|$ through a weight factor α. The new formulation is based on the previous analysis on Eqn. (3.10), which discovers that making $\sum_k^N \frac{\partial y_k}{\partial \theta_1} = 0$ could eradicate the estimation error caused by constant bias Δy. The problem can also be formulated as maximizing Fisher information subject to a hard constraint on $\sum_k^N \frac{\partial y_k}{\partial \theta_1} = 0$. Constant or slow-varying model/measurement bias is a common source of estimation error in practice [68], which can be caused by sensor/model drift due to change in operating condition or degradation. An example will be shown later to demonstrate that the new approach could enable far superior estimation accuracy than the Fisher-information only approach.

In the case of parameter uncertainty, e.g. in one parameter θ_2, a new optimization problem can be formulated as

$$\underset{\boldsymbol{u}}{Max} \sum_{k=1}^{N} \left(\frac{\partial y_k}{\partial \theta_1}(\boldsymbol{u}, \hat{\boldsymbol{\theta}}) \right)^2 - \alpha \left| \sum_{k=1}^{N} \frac{\partial y_k}{\partial \theta_1}(\boldsymbol{u}, \hat{\boldsymbol{\theta}}) \frac{\partial y_k}{\partial \theta_2}(\boldsymbol{u}, \hat{\boldsymbol{\theta}}) \right|, \tag{3.13}$$

by adding a soft constraint to minimize $\left|\sum_{k}^{N} \frac{\partial y}{\partial \theta_1}(\boldsymbol{u}, \hat{\boldsymbol{\theta}}) \frac{\partial y}{\partial \theta_2}(\boldsymbol{u}, \hat{\boldsymbol{\theta}})\right|$. This new formulation is based on the previous discovery that making $\sum_{k}^{N} \frac{\partial y}{\partial \theta_1} \frac{\partial y}{\partial \theta_2} = 0$ could eradicate the estimation error caused by $\Delta\theta_2$. Eqn. (3.13) can be augmented with more terms to accommodate uncertainty in more parameters. Parameter uncertainty is usually inevitable in practice [69]. On one hand, for systems with a large number of parameters, the identification procedure is typically sequential with some parameters being estimated first without knowing others [16]. On the other, it is often only of interest to estimate a subset of parameters. It will be shown that the new formulation could yield far superior results than the FI-based approach in such scenario.

Similarly, in the case of varying measurement/model uncertainty δy_k, a new problem can be formulated by adding $\sum_{k}^{N} \frac{\partial y_k}{\partial \theta_1} \delta y_k = 0$ as either hard or soft constraint. This new problem formulation is also of significant practical interest due to the inevitable model uncertainty. On one hand, no model is capable of capturing the dynamics of a system perfectly, no matter how complicated the model is. On the other, common model simplification techniques to facilitate control applications, e.g. model reduction [70] and linearization, introduce extra uncertainty. The new formulation indicates a way to address model uncertainty after characterizing it as an additive part of the model output. Specifically, if the dynamics/model of varying model/measurement uncertainty δy_k can be captured in whole or in part, for example in [71], it is possible then to design a profile that can mitigate the impact of δy_k by leveraging the sensitivity orthogonality.

Finally, for the general case of estimation subject to uncertainties in measurement, multi-parameters, and model, the data optimization problem is formulated as in Eqn. (3.14) by combining all previous cases.

$$\begin{aligned} \max_{\boldsymbol{u}} \sum_{k=1}^{N} \left(\frac{\partial y_k}{\partial \theta_1}(\boldsymbol{u}, \hat{\boldsymbol{\theta}}) \right)^2 - \alpha_1 \left| \sum_{k=1}^{N} \frac{\partial y_k}{\partial \theta_2}(\boldsymbol{u}, \hat{\boldsymbol{\theta}}) \frac{\partial y_k}{\partial \theta_1}(\boldsymbol{u}, \hat{\boldsymbol{\theta}}) \right| \cdots - \alpha_{n-1} \left| \sum_{k=1}^{N} \frac{\partial y_k}{\partial \theta_n}(\boldsymbol{u}, \hat{\boldsymbol{\theta}}) \frac{\partial y_k}{\partial \theta_1}(\boldsymbol{u}, \hat{\boldsymbol{\theta}}) \right| \\ - \alpha_n \left| \sum_{k=1}^{N} \frac{\partial y_k}{\partial \theta_1}(\boldsymbol{u}, \hat{\boldsymbol{\theta}}) \right| - \alpha_{n+1} \left| \sum_{k=1}^{N} \frac{\partial y_k}{\partial \theta_1}(\boldsymbol{u}, \hat{\boldsymbol{\theta}}) \delta y_k \right| \end{aligned} \tag{3.14}$$

The factors $\alpha_1, \cdots, \alpha_{n+1}$ are the weights for penalizing different uncertainty sources, and their values can be tuned based on estimates of the magnitude of respective uncertainties. In this chapter, the problem formulation is for single-variate estimation, which will be extended to the multivariate estimation case in the next chapter.

3.3 Simulation verification of methodology with battery electrochemical model

In this section, the application of the data optimization methodology to single-variate estimation of battery electrochemical parameters will be demonstrated. The estimation results using the optimized input current profile will be compared with those using pulses [21, 29], constant current [27, 28], and dynamic drive cycle profiles [72], which are the heuristic profiles widely adopted in the practice of battery parameter estimation. Meanwhile, comparison will also be made with the profile optimized using the FI-based approach, which is the traditional method for optimal input/experiment design [48, 16]. In this section, the studies will be performed in simulation using a single particle battery model with electrolyte dynamics (SPMe) presented in Chapter 2, with the parameters adopted from [15] for an LGM50 INR21700 battery. The target variables for estimation are the electrode (cathode) active material volume fraction ε_s, and lithium diffusion coefficient D_s, which are critical parameters related to key battery performance [73, 74]. The results under different types of uncertainties, namely constant measurement/model bias and/or parameter uncertainty will be presented.

3.3.1 Estimation of active material volume fraction ε_s

3.3.1.1 Estimating ε_s under constant model/sensor bias

The first case of demonstration is estimating ε_s subject to constant model/measurement bias. In this case, the optimal current profile is obtained by solving Eqn. (3.12) with $\theta_1 = \varepsilon_s$ and $\alpha = 1$, and the results are shown in Fig. 3.1. The initial SOC of the battery is set to 50% during optimization. For comparison, the profile optimized using the traditional FI-based approach by solving Eqn. (3.11) is also generated and shown in Fig. 3.2, of which the patterns have been explored in the literature [67]. Both optimization are performed assuming an *a priori* ε_s value that is 10% off the true value of 0.562, and subject to current constraint between -1C and +1C. It is noted that 10% deviation in ε_s translates to same amount of mismatch in battery capacity, which is significant uncertainty as the battery is only supposed to lose 20% capacity over lifetime according to the electric vehicle standard. Heuristic profiles commonly used for estimation in literature are also used for comparison, including constant current (CC) discharging at 1 C, a pulse profile (with alternating 25 s 1 C charge and discharge), and a dynamic drive cycle, i.e. Federal Urban Driving Schedule (FUDS). All profiles are of same length (30 min) and number of data points (6000) to ensure fair comparison. For data generation, each current profile is fed to the SPMe model to obtain the response voltage data, which are then injected with a constant bias of $-0.03\ V$ to emulate the measurement/model bias. Same current profiles will be used for experimental validation in Section 3.4.

The estimation results using different profiles are summarized in Tab. 3.1. The table shows that the optimal current profile obtained based on the new approach gives the best accuracy, as it achieves the minimum estimation error at 0.089%, while the error of the traditional FI-based approach is at -11.9%, which is 133 times as large. Such dramatic difference can be explained by the evolution of sensitivity $\frac{\partial y_k}{\partial \varepsilon_s}$ under the two profiles shown in Fig. 3.1(b) and 3.2(b) respectively. Specifically, under the profile obtained based on the new approach, $\frac{\partial y_k}{\partial \varepsilon_s}$ distributes nearly equally above and below 0, giving a small (normalized) $\sum_k^N \frac{\partial y_k}{\partial \varepsilon_s}$ = -3.67, while the sensitivity under the profile of the FI-based approach is mostly negative, giving a (normalized) $\sum_k^N \frac{\partial y_k}{\partial \varepsilon_s}$ = -1340. Therefore, although the sensitivity of the latter is more prominent, giving higher (Fisher) information level, the profile does not yield good accuracy when subject to uncertainty. Moreover, Tab. 3.1 also validates Eqn. (3.10) for error quantification, as the predicted estimation errors match well with the actual errors in general.

Table 3.1: Estimation results of ε_s under constant bias in simulation

Profile	Actual error	Predicted error	FI	$\sum_k^N \frac{\partial y_k}{\partial \varepsilon_s}$
New Approach	0.0890%	-0.130%	83.8	-3.67
FI Optimal	-11.9%	-14.0%	321	-1340
Pulse	19.1%	13.5%	3.38	18.7
1C CC	8.03%	7.59%	702	1930
FUDS	24.8%	18.6%	74.2	613

(a) Current profile

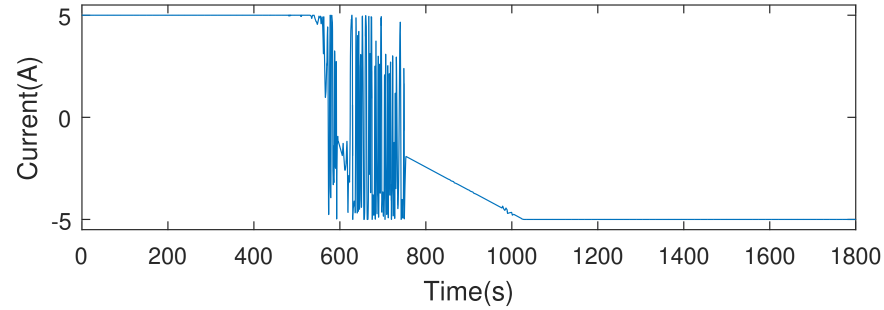

(b) Normalized ϵ_s voltage sensitivity

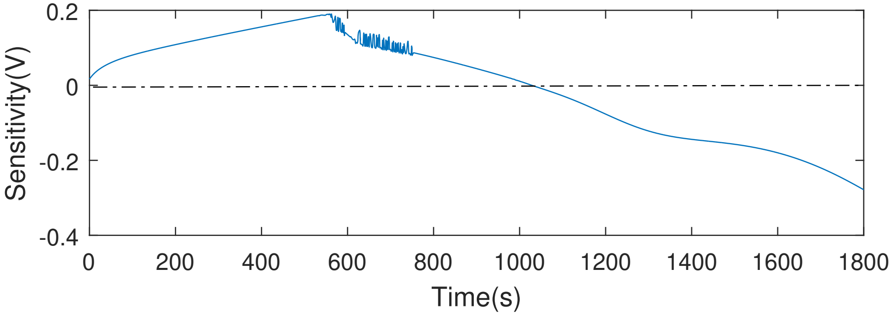

Figure 3.1: Optimized current profile for estimating ε_s subject to constant voltage bias using new approach

(a) Current profile

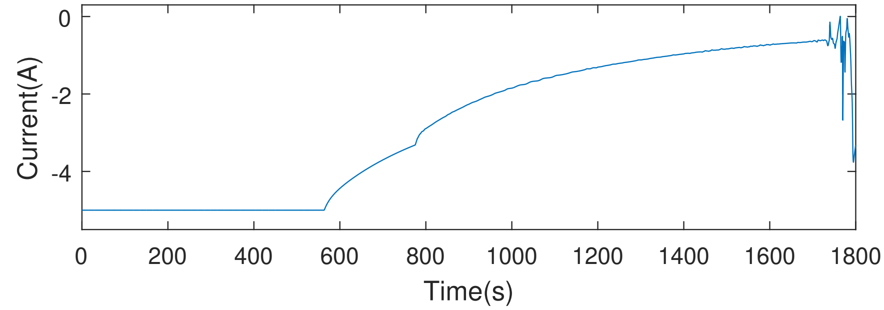

(b) Normalized ϵ_s voltage sensitivity

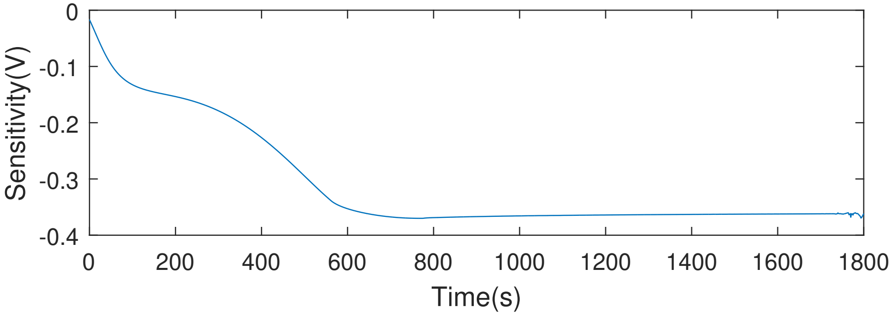

Figure 3.2: Optimized current profile for estimating ε_s using FI-based approach

3.3.1.2 Estimating ε_s under bias and parameter uncertainty

In this case, the estimation of ε_s is demonstrated, which is subject to both constant bias Δy and uncertainty in another battery parameter $\Delta\theta_2$, i.e. D_s. Data optimization using the new approach is performed by solving Eqn. (3.14) with $\theta_1 = \varepsilon_s$, $\theta_2 = D_s$, $\alpha_1 = 1$, $\alpha_n = 0.03$, and all other $\alpha = 0$. The optimal profiles obtained based on the new and FI-based approaches, along with other heuristic current profiles, are then used to generate the voltage output data in simulation. A constant -0.03 V bias is then injected to the voltage data to emulate the output bias, and during the process of estimating ε_s, the assumed value for D_s was deviated by 20% from the true value (used in simulation for data generation) to emulate the parameter uncertainty. The estimation results using different profiles are presented in Tab. 3.2, which shows that the profile designed by the new approach substantially outperforms all others. Specifically, the heuristic profiles, i.e. CC, pulse, and dynamic cycle, all yield significant estimation errors above 10%, while the FI-based approach achieves major improvement by reducing the error to around -7%. Still, our new approach manages

Table 3.2: Estimation results of ε_s under constant bias and parameter uncertainty in simulation

Profile	Actual error	Predicted error	FI	$\sum \frac{\partial y_k}{\partial \varepsilon_s}$	$\sum \frac{\partial y_k}{\partial D_s} \cdot \frac{\partial y_k}{\partial \varepsilon_s}$
New Approach	1.44%	0.46%	58.4	-128	24.8
FI Optimal	-6.93%	-8.93%	369	-1430	72.3
Pulse	17.2%	12.9%	3.29	17.8	-0.127
1C CC	12.1%	10.7%	699	1920	166
FUDS	27.7%	20.4%	74.0	610	-15.7

to yield a much smaller error at 1.44%, which is considered as highly accurate given the 20% uncertainty in D_s and the prominent constant voltage bias. The proposed approach achieves superior estimation accuracy by accommodating all 3 terms that contribute to the error during the multi-objective optimization procedures in this scenario, i.e. Fisher info, $\sum_k^N \frac{\partial y_k}{\partial \varepsilon_s}\Delta y$, and $\sum_k^N \frac{\partial y_k}{\partial D_s}\frac{\partial y_k}{\partial \varepsilon_s}\Delta \varepsilon_s$. As shown in the last 3 columns of Tab. 3.2, the new approach does not manage to optimize any individual term, but instead achieves the optimal balance among them to minimize the error. Tab. 3.2 also shows the effectiveness of Eqn. (3.10) for error quantification, since the predicted estimation errors match the actual errors pretty well under different current profiles.

3.3.2 Estimation of diffusion coefficient D_s

3.3.2.1 Estimating D_s under constant model/sensor bias

In this case, the estimation of D_s subject to constant bias Δy in voltage is shown. The procedures of data optimization, simulation data generation, and estimation are similar to those in Section 3.3.1.1, and hence not repeated. The input current profile optimized using the new approach is shown in Fig. 3.3. Estimation results using each profile are summarized in Tab. 3.3, which also shows the actual estimation error and predicted error calculated based on Eqn. (3.10).

It is seen that the optimal current profile obtained based on the new approach significantly outperforms all other profiles, as it achieves the minimum error at 0.055%, which is much better than all others, with the closest one given by the traditional FI-based profile at 27.7%, which is 503 times as large. Similar to the case of ε_s, the dramatic improvement in accuracy

Table 3.3: Estimation results of D_s under constant bias in simulation

Profile	Actual error	Predicted error	FI	$\sum_k^N \frac{\partial y_k}{\partial D_s}$
New Approach	0.0550%	0.0629%	2.98	-0.0625
FI Optimal	27.7%	23.2%	35.6	-382
Pulse	-128%	-139%	0.0600	1.22
1C CC	-44.3%	-60.5%	27.5	385
FUDS	-26687%	-11789%	0.0411	0.603

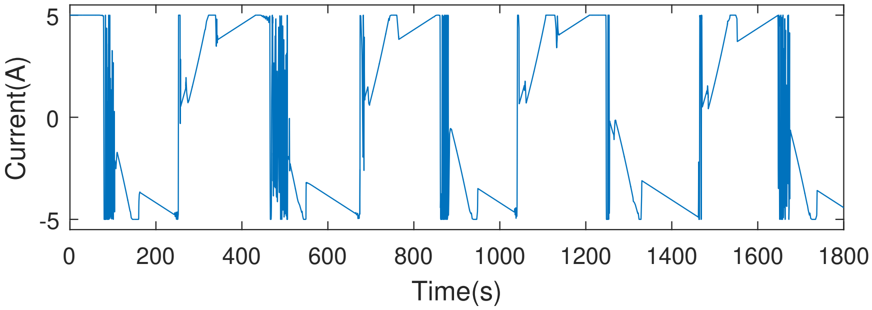
(a) Current profile

(b) Normalized D_s voltage sensitivity

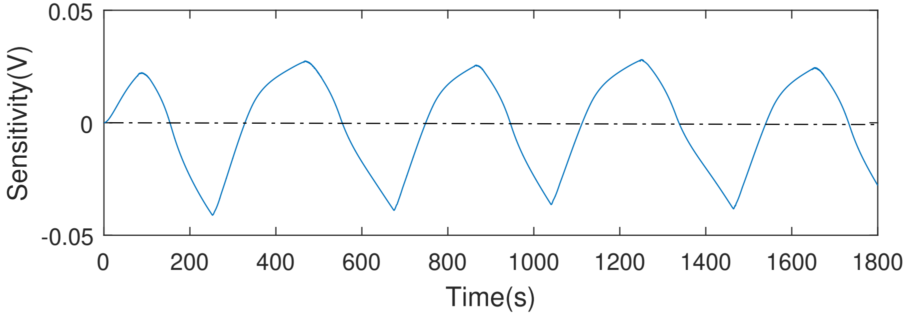

Figure 3.3: Optimized current profile for estimating D_s subject to constant model/measurement bias using new approach

can be explained by the evolution of sensitivity $\frac{\partial y_k}{\partial D_s}$ under the new profile, as shown in Fig 3.3(b). Specifically, the profile obtained based on the new approach gives a near-zero $\sum_k^N \frac{\partial y_k}{\partial D_s} = -0.0625$, while the sensitivity under the FI-based profile is at $\sum_k^N \frac{\partial y_k}{\partial D_s} = -382$.

Therefore, although the (Fisher) information level of the latter is higher, the estimation accuracy is still poor when subject to uncertainty. These results demonstrate the deficiency of the traditional FI-based approach, and the effectiveness of the new approach in rejecting uncertainty by incorporating $\sum_k^N \frac{\partial y_k}{\partial D_s} = 0$. On the other hand, the worst estimation result is given by the FUDS profile, whose error is more than 267 times of the true D_s value. Even though the FUDS has a fairly small $\sum_k^N \frac{\partial y_k}{\partial D_s} = 0.603$, its low Fisher information (0.0411) leads to the poor estimation accuracy. These findings further emphasize the importance of considering both Fisher information and our newly identified data structures for data optimization.

Tab. 3.3 also shows that Eqn. (3.10) can be effectively used for error quantification. For the proposed new optimal, FI-based optimal, CC and pulse profiles, the predicted estimation errors match well with the actual errors. The equation does not quite apply to the FUDS profile, mainly because the estimation result is too far off the actual value, and the derivation of Eqn. (3.10) is based on first-order Taylor expansion around the estimate.

3.3.2.2 Estimating D_s under parameter uncertainty

In this case, D_s is estimated subject to parameter uncertainty in the electrode active material volume fraction ε_s. The procedures of data optimization, simulation data generation, and estimation are similar to those in Section 3.3.1.2, and hence not repeated. For estimation, the assumed value for ε_s was deviated by 10% from the true value (used in simulation for data generation) to emulate the parameter uncertainty. The optimization results using our proposed new method, i.e. solving Eqn. (3.13) with $\alpha = 1$, are shown in Fig. 3.4.

Estimation results using each profile are summarized in Tab. 3.4, along with the actual

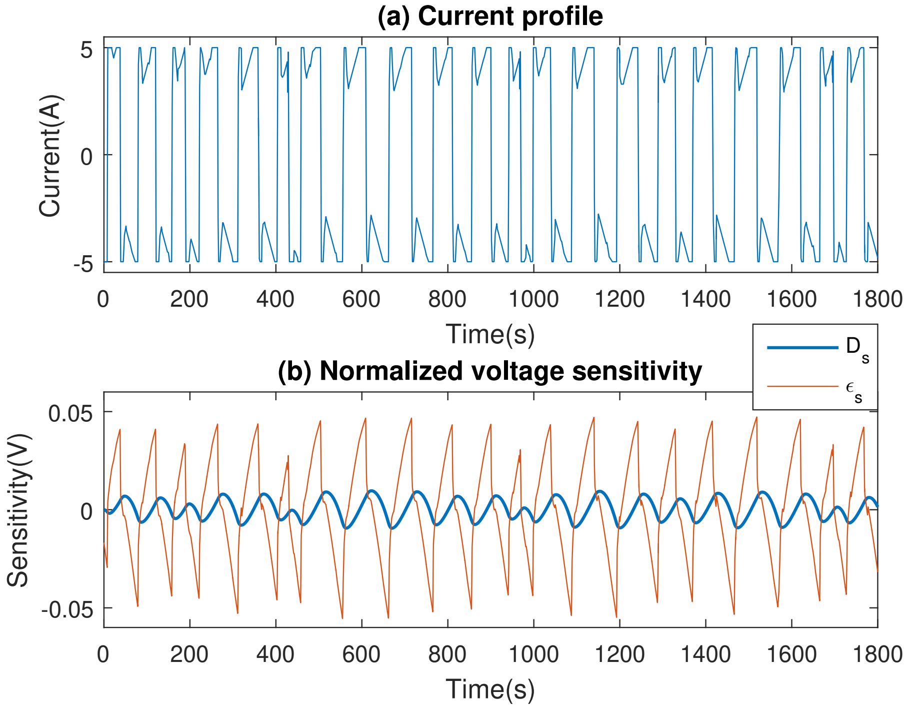

Figure 3.4: Optimized current profile for estimating D_s subject to parameter uncertainty using new approach

and predicted errors calculated based on Eqn. (3.10). It is seen that the profile optimized using the new approach achieves the minimum estimation error at 6.62%, which is better than all other profiles, with the FI-based approach at -42.2% and the pulse profile at 26.4% being the closest. The substantial improvement is attributed to the fact that the new profile is the only one designed to penalize $\left|\sum_k^N \frac{\partial y_k}{\partial D_s}\frac{\partial y_k}{\partial \varepsilon_s}\right|$, i.e. accommodating orthogonal D_s and ε_s sensitivity, as shown in Tab. 3.4. It is also interesting to note from Fig. 3.4(b) that the sensitivity of the uncertain parameter ε_s is much higher than that of the target parameter D_s (by one order of magnitude). Traditionally, estimating weakly sensitive parameters under the shadow of uncertainty in strongly sensitive parameters is extremely difficult if not totally impossible, which is the reason why all other profiles yield significant estimation errors which are one order of magnitude higher. The explanation can be given by our derived error

Table 3.4: Estimation results of D_s under parameter uncertainty in simulation

Profile	Actual error	Predicted error	FI	$\sum_k^N \frac{\partial y_k}{\partial D_s} \cdot \frac{\partial y_k}{\partial \varepsilon_s}$
New Approach	6.62%	6.49%	0.119	-0.0747
FI Optimal	-42.2%	-57.0%	22.8	82.4
Pulse	26.4%	22.9%	0.0249	-0.0697
1C CC	-54.9%	-81.3%	27.8	131
FUDS	-57.3%	-85.2%	1.57	7.67

formula in Eqn. (3.10). Specifically, the equation shows that the parameter uncertainty $\Delta\theta_2$ will propagate to the estimation error through $\sum_k^N \frac{\partial y_k}{\partial \theta_1} \frac{\partial y_k}{\partial \theta_2} \Delta\theta_2$. Therefore, high sensitivity of the uncertain parameter, i.e. $\frac{\partial y_k}{\partial \theta_2}$, will induce large estimation error. It is shown that by leveraging the orthogonal parameter sensitivity design, the weakly sensitive parameter can be estimated with satisfactory estimation accuracy.

3.4 Experimental validation of methodology

In this section, the experimental validation of the proposed new data optimization methodology will be presented in the context of the battery electrochemical parameter estimation problem. Experiments have been performed using an Arbin LBT21084 cycler on a LGM50T INR21700 battery cell. Various current profiles, including the optimized profiles using the new and FI-based approaches and baseline profiles shown in Section 3.3, are applied as input excitation to generate the voltage data, which are then used for parameter estimation based on the least squares algorithm and the SPMe model. The true parameter values for benchmarking the estimation error of the target variable and those of the remaining parameters are adopted from [15], which parameterized an LGM50 INR21700 battery with detailed electrochemical measurements. Some parameter values have been adjusted due to the slight difference in electrochemistry between the LGM50 and LGM50T batteries, i.e. the active material volume fraction. The results are shown for the estimation of the electrode active material volume fraction ε_s subject to different uncertainties under experiment conditions.

3.4.1 Estimating ε_s subject to model uncertainty

First, the case of estimation subject to model/measurement uncertainty is considered. Under experiment conditions, there is intrinsic model/measurement uncertainty with the estimation problem. Specifically, as no model could capture the system dynamics perfectly, there will always be mismatch between the actual and model predicted output, even if all the parameters and measurements are accurate. In the context of the single particle battery model discussed in this dissertation, there are limiting assumptions, such as uniform current density and lithium concentration distribution across the electrode, which could lead to model imperfection [14, 75]. In addition, model reduction procedures, e.g. Padé approximation used to simplify the original PDE-based diffusion equations, would also introduce mismatch between the model and true battery dynamics [13, 54, 76]. Such uncertainty could consist of a constant component, which is essentially the Δy term in Eqn. (3.10), and a varying component, which can be represented by the δy_k term in Eqn. (3.10). It is noted that the total model uncertainty is complicated as it changes over time and operating conditions. Therefore, model uncertainty will be different under different input profiles, which is difficult to know beforehand and hence design to compensate. Here the focus is to demonstrate the effectiveness of the proposed data optimization approach in countering the constant component of the uncertainty. Specifically, the profile designed in Section 3.3.1.1 to minimize the error induced by the constant bias Δy is used to estimate ε_s and compare with the estimates given by other profiles.

The results are summarized in Tab. 3.5. It is seen that the proposed approach gives the best estimation accuracy with an actual error of -3.69%, whereas all other profiles yield at least twice as large error. Compared with the simulation results previously shown in Tab. 3.1, the error of the optimized profile is larger, mainly due to the varying component of the model uncertainty that has not been accommodated in data optimization. Nevertheless, the results still demonstrate the effectiveness of improving the estimation accuracy subject to model uncertainty by countering the constant component. In addition, we have also validated Eqn. (3.10) for uncertainty quantification considering both constant and varying model uncertainty. Specifically, the differences between the measured battery voltage and the model prediction based on true parameter values are obtained for each profile, which are

Table 3.5: Estimation results of ε_s with model/measurement uncertainty in experiment

Profile	ε_s Estimate	Actual error	Predicted error
New Approach	0.582	-3.69%	-3.80%
FI Optimal	0.610	-8.60%	-9.78%
Pulse	0.444	21.0%	14.0%
1C CC	0.645	-14.8%	-16.0%
FUDS	0.526	6.32%	5.42%

then applied to Eqn. 3.10 as Δy and δy_k to compute the predicted estimation error. It can be seen that the predicted errors match well with the actual errors (which are computed as the difference between the estimated and true parameter values) for all profiles, validating the uncertainty propagation mechanisms established by our theoretic derivation.

3.4.2 Estimating ε_s subject to model and parameter uncertainty

In this case, parameter uncertainty in estimating ε_s under experimental conditions is further considered. The data optimization, experiment, and estimation procedures are mostly the same as in the previous case, except that the diffusion coefficient D_s is deviated by 20% in estimation to emulate the parameter uncertainty. The profiles optimized based on the new and FI-based approaches are the same as those in Section 3.3.1.2, as the former accommodates both constant component of the model uncertainty and parameter uncertainty in D_s. The results are summarized in Tab. 3.6, which shows that the profile designed by the new approach outperforms all other profiles and the predicted errors match well with the actual

Table 3.6: Estimation results of ε_s with model/measurement and parameter uncertainty in experiment

Profile	ε_s Estimate	Actual error	Predicted error
New Approach	0.582	-3.69%	-5.52%
FI Optimal	0.587	-4.52%	-5.87%
Pulse	0.442	21.4%	14.0%
1C CC	0.617	-9.94%	-11.3%
FUDS	0.508	9.62%	8.49%

errors. It is interesting to note that some profiles, especially the pulse and FUDS profiles, give better results than in simulation shown in Tab. 3.2. The reason is that the varying model uncertainty could cancel out some of the errors caused by other sources according to Eqn. (3.10), if the signs of relevant terms are opposite. However, such cancellation is unpredictable in practice and cannot be expected/utilized. For example, if any of the error terms switch sign due to change in operating conditions, the errors will be significantly amplified.

Chapter 4

Identification of Full Parameter Set of Single Particle Model

The identifiability and complexity of the nonlinear battery parameter estimation problem depends both on the data used and the number of parameters involved. Recognizing the outstanding challenges, there have been persistent efforts in the battery research community to investigate this topic. For example, several works sought to divide parameters into smaller groups, and then estimate each group sequentially. The grouping is performed based on either the rank and proximity of parameter sensitivity [77, 12, 29], or correlation to the same physical dynamics [21, 51]. This "divide-and-conquer" strategy both reduces the complexity of the estimation algorithm and improves the identifiability and accuracy of estimation for individual parameters, as fewer parameters are being estimated simultaneously.

This chapter aims at establishing a novel framework for identifying the full electrochemical parameter set of lithium-ion battery by integrating the data optimization approach developed in Chapter 3. First, a new parameter ranking and grouping method is proposed based on the Bode plots of the derived parameter sensitivity transfer functions to categorize parameters into different groups, which would enable sequential estimation of smaller parameter groups to facilitate the overall process. Subsequently, the new data optimization approach is applied to generate the optimal current excitations for estimating each group of parameters, considering both the traditional metric of Fisher information and the data structures for mitigating the impacts of system uncertainties. The proposed methodology is applied to estimating the full electrochemical parameter set of the single particle lithium-ion battery model in experiments, showing significantly improved estimation and voltage prediction accuracy compared with the traditional data-based identification approach.

The procedures involve three sequential steps as follows. First, the open circuit voltage (OCV)-related parameters are identified using the measured experiment data under low C rate discharging current. Second, sensitivity analysis is performed for other dynamic parameters, which are ranked and categorized into different groups according to the frequency spectrum of their sensitivity transfer functions (STF). Finally, data optimization is performed for each group of parameters, and the obtained input excitation sequences are used to experimentally generate data for identifying the parameters by group. The flowchart of parameter identification procedure can be seen in Fig 4.1.

Regarding the first step, the voltage response of the battery under low current can be conveniently used as the OCV data for estimating the OCV-related parameters, as the effects of non-OCV-related parameters are minimal under such condition. Identifying the OCV-related parameters first also makes it easier for the estimation of other dynamic parameters, because fewer parameters are involved in the estimation procedure afterwards.

In the second step, the parameter sensitivity transfer functions (STFs) derived in Chapter 2 are used for parameter ranking and grouping. This is different from the existing practice, which perform sensitivity analysis and parameter ranking/grouping based on the data that

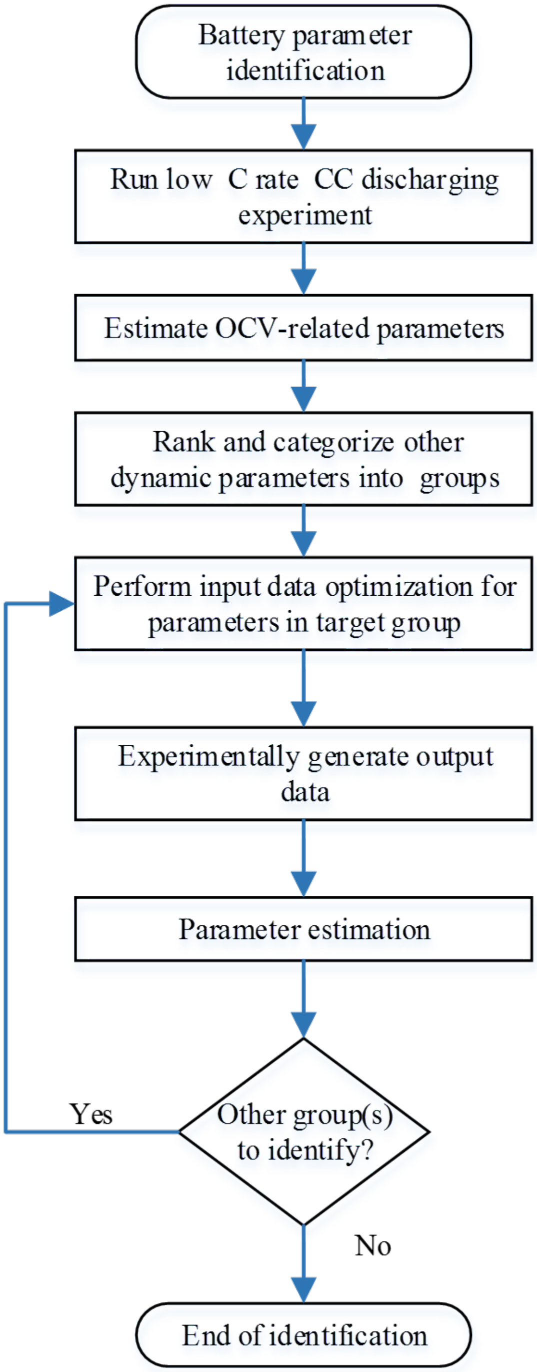

Figure 4.1: Proposed procedures for lithium-ion battery parameter identification

would be used for identification. In our framework, since the data are not available before the data optimization procedures in the subsequent (third) step, the derived STFs, which capture the parameter sensitivity dynamics under generic input, are adopted for serving the purpose. The parameter group with the highest sensitivity would be identified first, followed by less sensitive groups, as the uncertainty in strongly sensitive parameters tend to have higher impact on the weakly sensitive ones [78, 35].

In the third step, data optimization problems are formulated based on the methodology introduced in Chapter 3, aiming at mitigating the estimation error caused by different types of system uncertainties. The obtained current input excitation profiles are applied to parameter identification of each group separately. In particular, the approach looks to minimize the estimation errors of the former groups caused by the uncertainty in parameters of the latter groups by leveraging orthogonal sensitivity design [78, 66].

4.1 Identification of OCV-related parameters

In this step, the OCV-related parameters will be identified using the low current discharging data. When the input current magnitude is small, the voltage components in Eqn. (2.25) related to the electrolyte potential, overpotential, and ohmic resistance can be neglected. Meanwhile, the surface concentration of the particle $c_{se,i}$ is approximately the same as the volume-average concentration $\bar{c}_{s,i}$, due to the quasi-equilibrium condition under slow discharging. Therefore, we can fit the open circuit potential functions of the average concentration, which can be conveniently calculated by Coulomb counting, to the measured low C rate constant current discharging data to determine the OCV-related parameters [$\varepsilon_{s,p}$ $\varepsilon_{s,n}$

$\theta_{p,100}\ \theta_{n,100}]$.

The average concentration in the electrode particle $\bar{c}_{s,i}(t)$ can be calculated using coulomb counting (current integration) as

$$\bar{c}_{s,i}(t) = \frac{c_{s,i}^{max} \int_0^t I(\tau) d\tau}{Q_i}, \tag{4.1}$$

where

$$Q_i = FA\delta_i c_{s,i}^{max} \varepsilon_{s,i}, \tag{4.2}$$

representing the maximum allowed capacity of the electrode. Therefore, the evolution of the stoichiometry number θ_i over time, which is defined as the normalized surface concentration, can be obtained as

$$\begin{aligned} \theta_p(t) &\approx \theta_{p,100} + \frac{\int_0^t I(\tau) d\tau}{FA\delta_i c_{s,p}^{max} \varepsilon_{s,p}} \\ \theta_n(t) &\approx \theta_{n,100} - \frac{\int_0^t I(\tau) d\tau}{FA\delta_i c_{s,n}^{max} \varepsilon_{s,n}} \end{aligned} . \tag{4.3}$$

Subsequently, the battery voltage under low current can be expressed as

$$V(t) \approx U_p(\theta_p(t)) - U_p(\theta_n(t)). \tag{4.4}$$

To find the estimates of $[\varepsilon_{s,p}\ \varepsilon_{s,n}\ \theta_{p,100}\ \theta_{n,100}]$, a discrete-time nonlinear least squares optimization problem is formulated in Eqn. (4.5) to match the measured voltage V_m of N data points with the model prediction in Eqn. (4.4). It is noted that the open circuit potential functions for each electrode U_p and U_n are needed, which can be obtained from manufacturers or measured using half-cell or three-electrode setup [15]. In this work, we adopt the open circuit potential functions from [15], which used the same type of battery chemistry.

$$\underset{[\varepsilon_{s,p},\ \varepsilon_{s,n},\ \theta_{p,100},\ \theta_{n,100}]}{\text{minimize}} \sum_{k=1}^{N} [V(k) - V_m(k)]^2 \tag{4.5}$$

4.2 Ranking and grouping of dynamic parameters

In order to reduce the complexity and improve the well-posedness of the estimation problem, it is desired to divide parameters into smaller groups, and then estimate each group sequentially. Different strategies have been developed to group parameters and determine the order of identification according to the sensitivity ranking [16, 29, 12]. However, current practice is mostly based on the sensitivity computed over the specific data set chosen beforehand for estimation, which is not feasible in our case due to the unavailability of data before the subsequent input optimization step. Therefore, we propose a new ranking and grouping method based on the Bode plots of the parameter sensitivity transfer functions, which reveal the magnitude and dynamics of sensitivity under generic inputs without reliance on any specific data.

The Bode magnitude plots of the sensitivity transfer functions of different parameters are shown in Fig. 4.2. It is interesting to note the difference/similarity of the sensitivity dynamics among parameters. For example, the sensitivity of D_e and D_s are different in magnitude, but they share the same trend as both have a high constant plateau at low frequency and taper down after certain break frequency. This suggests that both are sensitive to low frequency current inputs while insensitive to high frequency ones. On the contrary, the sensitivities of k_p and k_n are independent of frequency with constant magnitude. The magnitude plots of the STFs will be used for parameter ranking, based on the average magnitude of each parameter over a certain frequency range. Parameters with similar average sensitivity magnitude will be placed in the same group and identified together. Meanwhile, frequency response of the STFs can help determine parameters that are fundamentally not distinguish-

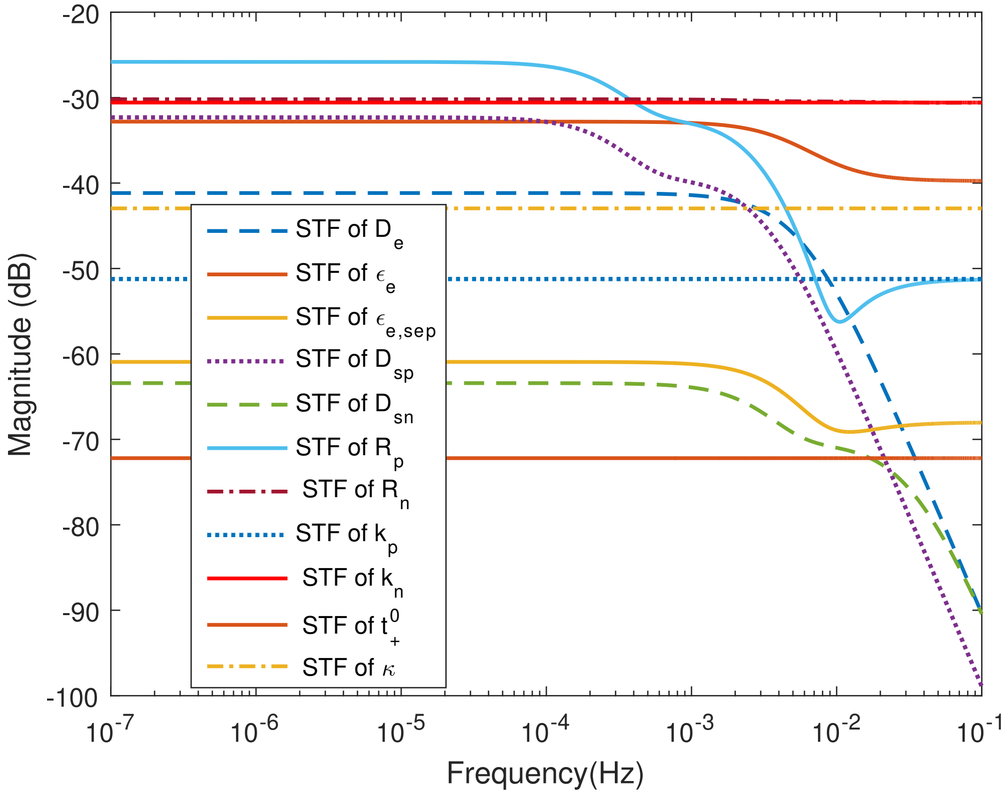

Figure 4.2: Bode magnitude plots of parameter sensitivity transfer functions

able. Specifically, if two parameters show different sensitivity patterns in a certain frequency range, they will have distinctive impacts on the output in that input frequency range. It is hence possible to design input excitation to distinguish and estimate them. On the contrary, similar sensitivity patterns of different parameters indicate similar impact on the output, which makes it difficult/impossible to retrieve/estimate the parameters separately from the output. For example, in Fig. 4.2, the STF curves of k_n and R_n are almost identical over the whole frequency range, which means that they are hardly distinguishable. Therefore, only one of them can be estimated, and the other one needs to be assumed using prior knowledge. These insights show that the Bode magnitude plots of the sensitivity transfer functions are useful tools for parameter ranking and grouping.

4.3 Current profile optimization strategy

In this subsection, data optimization is applied to improve the accuracy of estimating each group of parameters. The main goal is to obtain an optimal current excitation sequence for each group of parameters, which could generate data for estimation that are robust to system uncertainties in measurement, model, and parameter. In Chapter 3, a formula has been derived to quantify the error of estimating a single parameter subject to different types of uncertainties for the commonly used least squares algorithm, shown in Eqn. (3.10). Based on the data structures for mitigating uncertainties indicated by the formula, a new problem formulation can be proposed for input excitation optimization to simultaneously estimate various parameters in a group.

Consider a group of n target parameters, subject to uncertainty in q other parameters (which are either estimated in a later group or not estimated) and measurement/model bias and uncertainty, the problem formulation takes the form,

$$\begin{aligned}\max_{\boldsymbol{u}=[u_1,u_2,...u_N]} & \sum_{l=1}^{n}\left[\sum_{k=1}^{N}\left(\frac{\partial y_k}{\partial \theta_l}(\boldsymbol{u},\hat{\boldsymbol{\theta}})\right)^2\right]-\sum_{\substack{j=1\\ j\neq l}}^{n+q}\sum_{l=1}^{n}\left|\alpha_{j,l}\sum_{k=1}^{N}\frac{\partial y_k}{\partial \theta_l}(\boldsymbol{u},\hat{\boldsymbol{\theta}})\frac{\partial y_k}{\partial \theta_j}(\boldsymbol{u},\hat{\boldsymbol{\theta}})\right| \\ & -\alpha_2\sum_{l=1}^{n}\left|\sum_{k=1}^{N}\frac{\partial y_k}{\partial \theta_l}(\boldsymbol{u},\hat{\boldsymbol{\theta}})\right|-\alpha_3\sum_{l=1}^{n}\left|\sum_{k=1}^{N}\frac{\partial y_k}{\partial \theta_l}(\boldsymbol{u},\hat{\boldsymbol{\theta}})\delta y_k\right|,\end{aligned} \tag{4.6}$$

where the optimization variables are the input sequence $\boldsymbol{u} = [u_1, u_2, ...u_N]$. The cost function aims at minimizing the impacts of each uncertainty source. Specifically, the first term maximizes the summation of the Fisher information of the n target parameters, which is the denominator of the error formula in Eqn. (3.10). The second term minimizes the effects of parameter uncertainty by penalizing the inner products of the sensitivity sequence vectors between the target parameters and the uncertain parameters, as well between the target parameters themselves. The grouping-based parameter estimation strategy intrinsically introduces a source of estimation error due to parameter uncertainty. That is, when performing model fitting for a certain group of parameters, those from other groups, which also need to be used in the model, are not known exactly and need to be assumed with *a priori* values. The mismatch between the assumed and the (unknown) true values would propagate to induce estimation error in the form of parameter uncertainty [35, 78]. The third term minimizes the impact of constant model/measurement bias by penalizing the sum of sensitivity of each target parameter. The fourth term minimizes the inner products of the sensitivity sequence vector of the target parameter with that of varying model/measurement uncertainty (if somehow characterized). The factors $\alpha_{j,l}$, α_2, and α_3 are the weights assigned to different types of uncertainty, whose values can be tuned based on rough prior knowledge of the magnitude of respective uncertainties.

The estimation results using the current profiles optimized by our new approach will be compared with those using other profiles, including ones optimized using the conventional FI-based approach. The cost function of the FI-based approach aims at optimizing a certain metric of the Fisher information matrix for the n target parameters (under i.i.d. Gaussian output noises)[37, 66],

$$\mathbf{F} = \begin{bmatrix} \sum_{k=1}^{N} \left(\frac{\partial y_k}{\partial \theta_1}\right)^2 & \sum_{k=1}^{N} \frac{\partial y_k}{\partial \theta_1}\frac{\partial y_k}{\partial \theta_2} & \cdots & \sum_{k=1}^{N} \frac{\partial y_k}{\partial \theta_1}\frac{\partial y_k}{\partial \theta_n} \\ \sum_{k=1}^{N} \frac{\partial y_k}{\partial \theta_2}\frac{\partial y_k}{\partial \theta_1} & \sum_{k=1}^{N} \left(\frac{\partial y_k}{\partial \theta_2}\right)^2 & \cdots & \sum_{k=1}^{N} \frac{\partial y_k}{\partial \theta_2}\frac{\partial y_k}{\partial \theta_n} \\ \vdots & \vdots & \vdots & \vdots \\ \sum_{k=1}^{N} \frac{\partial y_k}{\partial \theta_n}\frac{\partial y_k}{\partial \theta_1} & \sum_{k=1}^{N} \frac{\partial y_k}{\partial \theta_n}\frac{\partial y_k}{\partial \theta_2} & \cdots & \sum_{k=1}^{N} \left(\frac{\partial y_k}{\partial \theta_n}\right)^2 \end{bmatrix}. \tag{4.7}$$

The commonly used metrics include the determinant (D-optimality), trace (A-optimality) and the largest eigenvalue (E-optimality) of the Fisher information matrix [16, 30]. It is noted that Fisher information is included in the objective function of our new approach shown in Eqn. (4.6). Specifically, the first term in Eqn. (4.6) is exactly the trace of the Fisher information matrix (sum of the diagonal elements), and the determinant of the Fisher information is approximately contained in the first two terms (to be exact if the absolute value operation is replaced by the squared operation for the components between the target parameters themselves in the second term). The new approach further addresses the uncertainties from the unestimated parameters as well as the model/measurement, which are the main advantages not available from the conventional FI-based approach [16, 30].

4.4 Experiment results

In this section, the proposed system identification procedures will be applied to estimating the parameter set of a LGM50T INR21700 lithium-ion battery. Experiments are performed using an Arbin LBT21084 cycler. The estimates of (dynamic) parameters will be compared with the benchmark obtained using the measurement-based techniques in [15] as well as with the estimation results using the conventional data-based identification approach. Moreover, the voltage prediction accuracy of the parameterized model will also be validated and compared based on new data not used in estimation.

4.4.1 Estimation results of OCV-related parameters

The estimation results of the OCV-related parameters are shown in Tab. 4.1, which are obtained by solving the optimization problem in Eqn. (4.5) using voltage measured under a C/40 constant-current profile. The profile discharges the fully charged battery to the

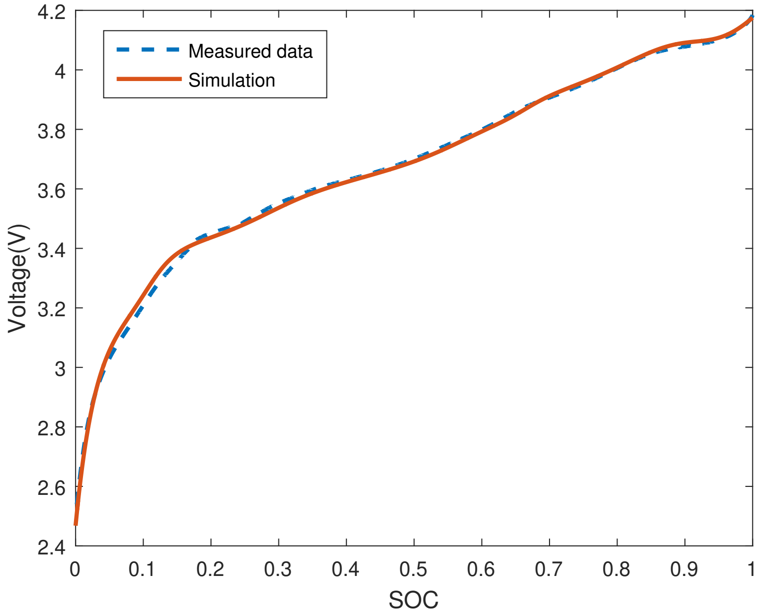

Figure 4.3: Fitting of OCV based on estimated parameters

minimum cut-off voltage. The values of $\theta_{p,0}$ and $\theta_{n,0}$ are calculated using the current integral over the whole discharging period based on Eqn. (4.3) given the estimated $\theta_{p,100}$ and $\theta_{n,100}$. The good match between the model voltage output V and the measured voltage data V_m, shown in Fig. 4.3, indicates the fidelity of the estimated OCV-related parameters.

Table 4.1: Identified OCV-Related Parameters

Parameter	Estimated value
$\varepsilon_{s,p}$	0.570
$\varepsilon_{s,n}$	0.721
$\theta_{p,100}$	0.272
$\theta_{p,0}$	0.926
$\theta_{n,100}$	0.901
$\theta_{n,0}$	0.0273

4.4.2 Ranking and grouping results of dynamic parameters

The ranking and grouping are performed based on the Bode magnitude plots of the parameter sensitivity transfer functions (STFs) as discussed in Section 4.2. Simplification and reformulation are needed to construct the STFs for some parameters. Specifically, linearization is applied to nonlinear functions such as the overpotential, which is simplified to

$$\eta \approx \frac{RTR_s \cdot I}{3\varepsilon_s FA\delta i_0}. \tag{4.8}$$

The slope of the open circuit potential is set equal to the average value in the SOC range from 25% to 75% to obtain the STFs of parameters related to the solid-phase lithium diffusion, given that the current profile used for estimation will be optimized with the initial SOC at 50%. The electrolyte concentration on the cathode boundary is set to 1100 mol/m^3 and that on the anode boundary is set to 900 mol/m^3 to obtain the STFs of parameters related to the electrolyte-phase li-ion diffusion. In addition, $\frac{\partial \eta}{\partial c_{se}}$ is neglected due to its minimal contribution to the sensitivity. It is also noted that the numerical computation of STFs needs to use the values of the parameters. Since the parameters remain unknown before being estimated, their values are randomly generated in a range of [-25%, +25%] deviation from the benchmark parameter values adopted from [15]. Such deviation can be significant, as, for example, the deviation in the active material volume fraction translates to the same amount of mismatch in battery capacity. Besides, the sensitivity magnitude is analyzed in the input frequency range from $10^{-7}Hz$ to $10^{-1}Hz$, since the parameters are most sensitive in this range according to Fig. 4.2. Moreover, the parameter sensitivities used in ranking, grouping, and subsequent data optimization, are normalized by multiplying with the (assumed) parameter values, in order to account for the significant disparity in value range among parameters.

The parameter ranking and grouping results based on the average magnitude of the STFs are shown in Tab. 4.2. It is noted that the grouping considers both the proximity of sensitivity magnitude among parameters and their potential correlation. For example, κ and ε_e, which both have significant impacts on voltage through the electrolyte resistance, may have inherent mutual dependence on sensitivity, and are hence assigned into different groups albeit with similar sensitivity mangitude. For the same reason, D_e is placed in Group 4 rather than Group 3. Meanwhile, since k_n and R_n are hardly distinguishable due to similarity in sensitivity over the whole frequency range, R_n is not estimated and set equal to the value found in literature for similar battery chemistry. Same applies to k_p and R_p.

Table 4.2: Dynamic parameter ranking and grouping

Group assigned	Parameter	Average sensitivity magnitude (dB)
Group 1	k_n	-30.6
	ε_e	-39.1
Group 2	κ	-43.0
	k_p	-51.2
Group 3	ε_{sep}	-68.0
	t_+^0	-72.2
Group 4	D_e	-74.5
	$D_{s,n}$	-79.9
	$D_{s,p}$	-82.3

4.4.3 Input optimization and estimation results of dynamic parameters

Based on the grouping, estimation proceeds from the parameters in Group 1, which are the most sensitive, to Group 4, which are the least. The current profile used for estimating parameters in Group 1 is optimized by solving Eqn. (4.6), with the first term maximizing the Fisher information of parameters in Group 1 and the second term penalizing the uncertainty of parameters in both Group 1 and Group 2. The uncertainty of parameters in Group 3 and Group 4 are neglected to simplify the optimization problem, since they are much less sensitive. Similarly, when optimizing current profiles for Group 2 and Group 3, we penalize the uncertainty of parameters in the target group and the next group based on the ranking shown in Tab. 4.2. For Group 4, which is the last group, only uncertainties in parameters within the group are penalized but not those from other groups, since other parameters are already identified and hence the impact of their uncertainty is considered minimal. In addition, the current profile optimization in this work does not consider the constant and varying model/measurement uncertainty Δy_k and δy_k, i.e. the third and fourth terms in Eqn. (4.6), because these two types of uncertainties are model and battery chemistry-dependent, which remains an interesting topic for future study.

The current profiles optimized using the new strategy and the FI-based approach for estimating parameters in Group 1 are shown in Fig. 4.4 as an example for illustration. The estimation results of dynamic parameters in each group using the optimized current profiles are compared with those obtained using other profiles to demonstrate the effectiveness of the new data optimization methodology. The current profiles used for comparison include the one optimized by the FI-based approach, and several heuristic profiles commonly used for

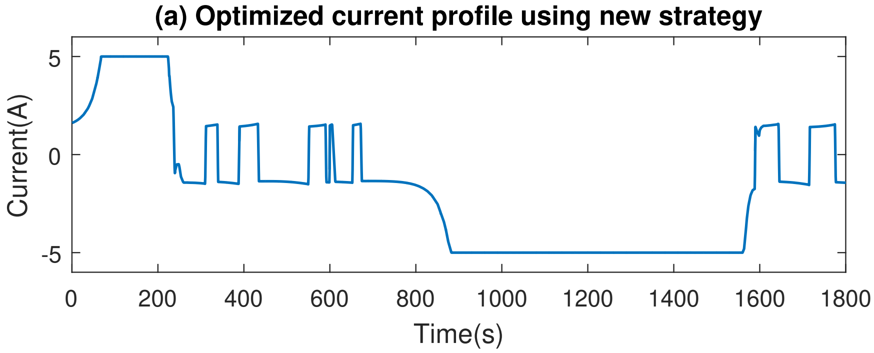
(a) Optimized current profile using new strategy

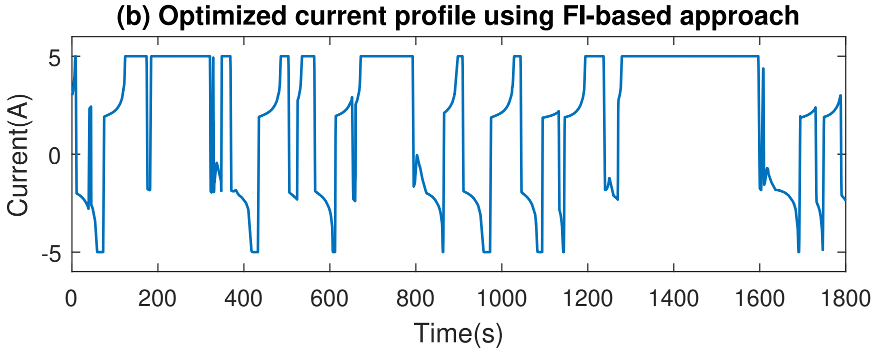
(b) Optimized current profile using FI-based approach

Figure 4.4: Optimized current profile of (a) new strategy and (b) FI-based approach for estimating parameters in Group 1

estimation in literature, including constant current (CC) discharging at 1 C, a pulse profile (with alternating 25 s 1 C charge and discharge), and a dynamic drive cycle, i.e. Federal Urban Driving Schedule (FUDS). All profiles are of the same length (30 min) and number of data points (6000) to ensure fair comparison. To benchmark the estimation accuracy, the difference between the parameter estimates and the values obtained using measurement techniques in the aforementioned reference [15] are computed. It is noted that the parameter values obtained in [15] may not be completely accurate for two reasons. First, the chemistry of the battery used in this paper is not exactly the same as that in [15], i.e. LGM50T versus LGM50. Second and more importantly, in [15], several parameters , e.g. $D_{s,n}$, still need to be hand tuned to make the model prediction match with the experimental data under different current profiles. Nevertheless, the results in [15] still provide a good reference to approximately check the validity of the parameter estimates in this work. Further validation of the parameter estimates will be performed in the next subsection based on the voltage prediction accuracy.

The estimation results for each parameter group are summarized and compared in Tab. 4.3-4.6. It can be seen that current profiles optimized using the new approach produce

Table 4.3: Group 1 parameter estimation results

Profile	$\hat{k}_n$ ($\times 10^{-12}$)	Deviation from measurement in [15]	$\hat{\varepsilon}_e$	Deviation from measurement in [15]
New approach	6.70	0.201%	0.356	-21.7%
FI-based approach	7.86	-17.0%	0.241	17.6%
1 C CC	4.18	37.8%	0.847	-190%
Pulse	3.72	44.7%	0.474	-62.0%
FUDS	8.08	-20.3%	0.212	27.5%

Table 4.4: Group 2 parameter estimation results

Profile	$\hat{k}_p$ ($\times 10^{-11}$)	Deviation from measurement in [15]	$\hat{\kappa}$	Deviation from measurement in [15]
New approach	3.65	-2.87%	1.07	-13.1%
FI-based approach	1.25	64.6%	1.30	-37.5%
1 C CC	3.31	6.62%	1.31	-38.4%
Pulse	2.12	40.2%	0.677	28.7%
FUDS	9.42	-166%	0.391	58.8%

Table 4.5: Group 3 parameter estimation results

Profile	$\hat{\varepsilon}_{sep}$	Deviation from measurement in [15]	$\hat{t}_+^0$	Deviation from measurement in [15]
New approach	0.482	-2.53%	0.202	22.3%
FI-based approach	1.38	-193%	1.29	-398%
1 C CC	0.541	-15.1%	0.374	-44.1%
Pulse	0.0910	80.7%	0.480	-85.0%
FUDS	0.409	12.9%	0.0540	79.2%

Table 4.6: Group 4 parameter estimation results

Profile	$\hat{D}_e$ $(\times 10^{-10})$	Deviation from measurement in [15]	$\hat{D}_{s,p}$ $(\times 10^{-15})$	Deviation from measurement in [15]	$\hat{D}_{s,n}$ $(\times 10^{-14})$	Devia -tion
New approach	2.51	-41.7%	4.06	-1.57%	66.8	-
FI-based approach	0.173	90.2%	1.13	71.7%	0.0608	-
1 C CC	10.2	-474%	2.88	28.0%	3.42	-
Pulse	5.38	-204%	17.1	-327%	67.7	-
FUDS	3.65	-106%	2.11	47.2%	1.04	-

estimation results closest to the measurement values from [15] for all but one parameters. For example, the estimate of k_n under the optimized current profile has a deviation of only 0.20%, which is two order of magnitude better than all other profiles. For k_p, ε_{sep}, and $D_{s,p}$, the deviations are all within 3%, while those of most other profiles are above 20%. The only exception is ε_e, for which the deviation of the profile optimized using the new approach is slightly larger than that of the FI-based profile (-21.7% versus 17.6%). Another noteworthy parameter is $D_{s,n}$, of which the deviations from measurement are not specified. The reason is that the work in [15] could not find a single deterministic value for $D_{s,n}$, which would match the voltage prediction under different C-rates. Again, as mentioned previously, the measurement values from [15] do not necessarily provide the absolutely accurate benchmark for rigorously evaluating the estimation accuracy, but they can still be used as good references for comparing the results of different current profiles. The closer match of the estimation results produced by our proposed new approach demonstrates its effectiveness in achieving accurate estimation of large battery parameter set compared with existing practices which primarily rely on heuristic or FI-based optimal current profiles.

4.4.4 Validation of parameterized model

In this subsection, the parameterized model will be tested under various input profiles not used for identification, including driving cycles and constant current (CC) profiles. The voltage prediction of the model is simulated under these inputs and compared with the experimental measurement to quantify the estimation error. The error statistics, including the root mean squared error (RMSE) and peak error, are used to validate the model fidelity against the models parameterized using other approaches.

First, regarding the drive cycle testing, 3 cycles from real-world electric vehicle operation with distinctive dynamics are considered, namely the dynamic stress test (DST), US06 highway driving schedule, and Beijing dynamic stress test (BJDST). The purpose of drive cycle testing is to evaluate the model fidelity subject to random and fast-varying current/power demand. All tests are performed with initial SOC=70%. The voltage prediction result is compared with that of the model parameterized using the profiles optimized based on the conventional FI-based approach. Tab. 4.7 compares the RMSE of the models identified by the proposed and the FI-based approaches under different drive cycles. It is seen that the proposed approach substantially outperforms the conventional approach, reducing voltage prediction errors by 77.3% for DST, 81.4% for US06, and 84.0% for BJDST. The comparison of the voltage prediction for the two models against measurement data under US06 drive cycle is shown in Fig. 4.5 as an example to demonstrate the model fidelity over the whole cycle and superior performance of the new approach.

Table 4.7: RMSE between model prediction and experimental measurement under drive cycle testing

Testing profile	Errors of new framework (mV)	Errors of FI-based approach (mV)
DST	18.0	79.4
US06	18.5	99.2
BJDST	15.0	93.8

Second, constant-current discharging testings are performed under various C rates of 0.5, 1, and 1.5 C, which discharge the battery from SOC=100% to the minimum cut-off voltage followed by a 2-hour relaxation period. The purpose is to evaluate the model fidelity over the whole SOC range under different current input magnitude. The voltage prediction of the parameterized model is compared with that in the aforementioned work [15], where the parameters of a battery with very similar chemistry were determined using invasive measurement-based techniques that require electrochemical characterization, and voltage

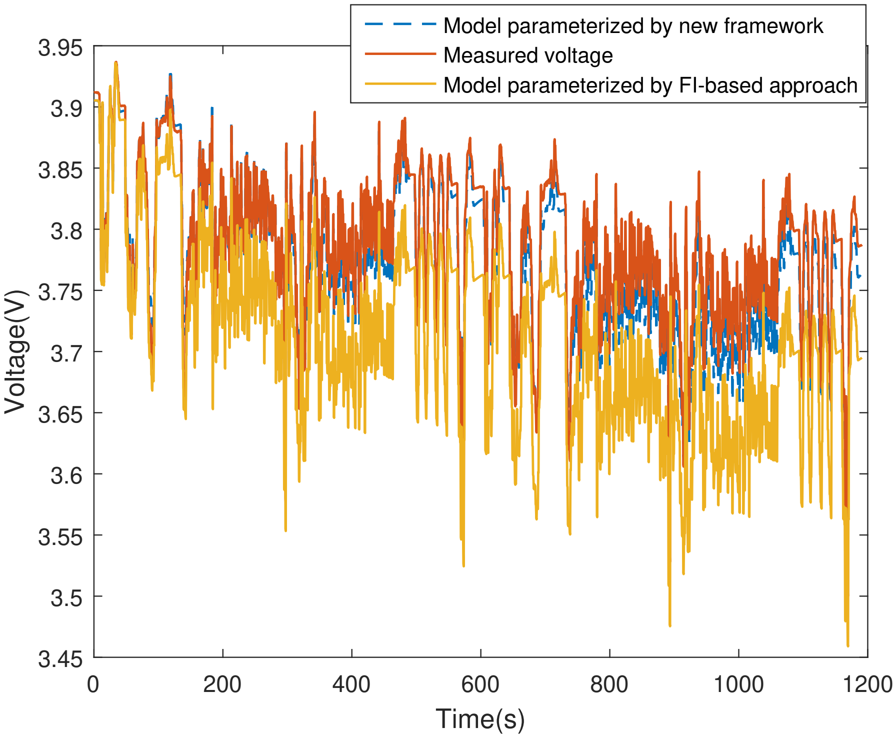

Figure 4.5: Comparison of model prediction and measured voltage under US06 driving schedule

predictions were generated under the same conditions based on a full order DFN model using the obtained parameters. Tab. 4.8 compares the RMSE and peak errors of the two models under the various C rates, and Fig. 4.6 shows the comparison of model prediction and experimental measurement over the whole profiles. It is seen that the voltage prediction of

Table 4.8: RMSE and peak errors under CC discharging profiles with 2-hour relaxation

Testing profile	RMSE (mV)		Peak error (mV)	
	New framework	[15]	New framework	[15]
0.5C CC	43.2	46	296	302
1C CC	33.7	41	239	271
1.5C CC	28.9	36	180	272

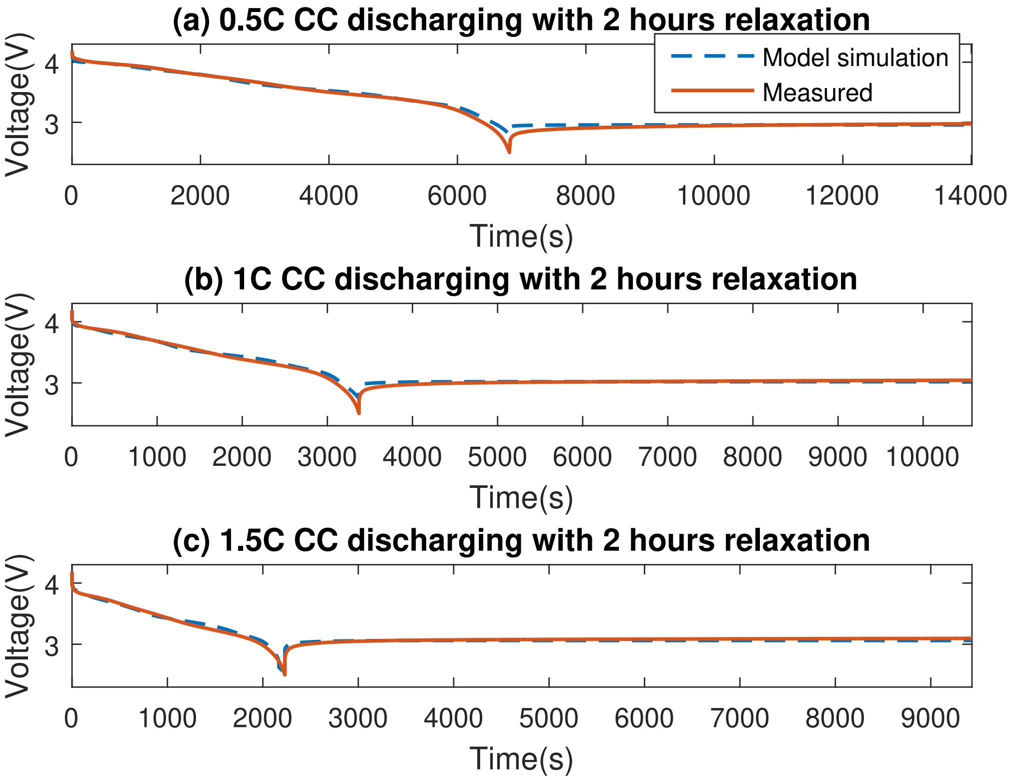

Figure 4.6: Comparison of model prediction and measured voltage under CC discharging of different C rates with 2-hour relaxation

the model parameterized from the non-invasive data-based approach in this work is in general more accurate. Specifically, the voltage prediction RMSEs of the model parameterized by the new approach are 43.2 mV, 33.7 mV, and 28.9 mV respectively under different C rates while those in [15] are 46 mV, 41 mV, and 36 mV respectively under the same profiles.The voltage prediction peak errors of the model parameterized by the new approach are also smaller than those of the P2D model parameterized in [15] under the same profiles. The peak errors occur when the battery reaches the extreme tail of the discharging voltage curve, as shown at 6809 second of Fig. 4.6 (a), similar to the observations from [16, 15]. The large values of the peak errors are caused by the steep slope of the open circuit potential at the battery low voltage limit, where a small mismatch in battery SOC could lead to a significant deviation of voltage. More importantly, it is noted that for the model parameterized in [15], the values of several parameters need to be hand tuned and treated as current dependent in order to provide the voltage prediction accuracy shown in Tab. 4.8. For example, the anode diffusion coefficient $D_{s,n}$ is calibrated as 1.3×10^{-14} m^2s^{-1} for the 0.5 C constant current profile, 3.3×10^{-14} m^2s^{-1} for the 1C profile, and 6.3×10^{-14} m^2s^{-1} for the 1.5 C current profile, varying by a lot over the current range. On the contrary, for the model parameterized in this work, only a single deterministic value of $D_{s,n}$ is needed to match all current input magnitude. In addition, it is also encouraging to see that the parameterization framework in this work enables the single particle model to produce comparable or even better accuracy than the full order P2D model in [15]. It is noted though that the formulated objective function for data optimization (and the resultant current profile) is dependent on the model parameters, which are unknown and need to be assumed with *a priori* values when performing the data optimization. The results will be affected by the assumed parameter values, and large deviation could lead to degraded performance of the obtained profiles.

Chapter 5

Summary and Recommendations

5.1 Summary

This dissertation is dedicated to developing a novel data optimization framework to improve the electrochemical parameter identification accuracy of lithium-ion battery. First, analytic derivation and analysis of the sensitivity of battery electrochemical parameters are performed. It is shown that different parameters are associated with distinctive sensitivity dynamics, and the parameter sensitivity typically consists of different terms featuring linear/nonlinear and dynamic/non-dynamic properties due to the physics underlying different voltage components. A method is proposed to derive different sensitivity terms based on assumptions and model reduction/reformulation techniques. The derived analytic expressions have been verified through comparison with the numerical simulation based on a full-order P2D model, showing satisfactory fidelity under typical operating scenarios. The analytic expressions could significantly benefit the emerging research on data optimization for battery state and parameter estimation, e.g. enabling direct optimization of the input excitation for off-line parameter identification, which was previously intractable due to the computational complexity.

Second, a new data analysis and optimization methodology for dynamic system parameter estimation is formulated, which is capable of achieving excellent estimation accuracy subject to uncertainties in measurement, model, and parameters. A formula for quantifying the errors of the least squares estimation algorithm has been derived first. Based on the formula, several desirable data structures are identified that could mitigate the propagation of uncertainties to the estimation error. For example, to counter constant measurement/-model bias, it is desirable to have the sum of sensitivity of the target parameter equal to zero over the whole data sequence. Meanwhile, to counter parameter uncertainty, it is desirable to have the sensitivity (vector) of the target parameter orthogonal to that of the uncertain parameter. The new methodology is then established by incorporating these data structures into the objective function (or constraints) of data optimization to supplement the traditional Fisher information criterion and leveraging the efficient sensitivity computation technique developed previously. Finally, the methodology is applied to the single-variate estimation of battery electrochemical parameter in simulation and experiments subject to model and measurement uncertainties, and demonstrates superior uncertainty rejection capability over the traditional Fisher-information-based approach and other baselines. For example, by utilizing orthogonal sensitivity design, the new methodology enables accurate estimation of weakly sensitive parameters under the shadow of uncertainty in strongly sensitive parameters, which has previously been extremely difficult. Using the generated input excitation for estimation reduces the estimation error by up to two orders of magnitude compared to the Fisher-information-based approach.

Third, the problem of identifying the full battery electrochemical parameter set is investigated. The data optimization capability is incorporated to the system identification procedures, while most existing research relies on empirical data. One key step of the procedures is to rank and group the parameters based on their sensitivity to facilitate the estimation process. As opposed to previous works which performed sensitivity analysis on a specific data set, the proposed parameter ranking and grouping in this work is based on the Bode magnitude plots of the derived sensitivity transfer functions, which reveal the fundamental sensitivity dynamics and do not rely on specific data. The method is more generic and applicable, and fits with our framework since the ranking and grouping precedes the step of data optimization. Data optimization using the methodology formulated in Chapter 3 is then performed to generate the optimal input excitation for estimating each parameter group. The proposed framework integrates parameter ranking/grouping and data optimization to present a new solution for identification of the full parameter set. The framework is applied to estimate the battery electrochemical parameters in experiments and demonstrates superior performance over the traditional Fisher-information-based approach and other baselines.

5.2 Recommendations for future work

One area worthy of investigation is to further expand the data optimization framework to enable mitigation of the estimation error caused by varying modeling/measurement uncertainty. Since no model can precisely capture all the dynamics of a system, especially for the complicated ones, model uncertainty will inevitably induce estimation errors in practice. The error formula Eqn. (3.10) derived in Chapter 2 shows how such uncertainty, represented by δy_k as an additive part of the model output, would induce the estimation error for the least squares algorithm, as well as indicates the data structure for reducing such error, i.e.

making $\sum_k^N \frac{\partial y_k}{\partial \theta_1} \delta y_k = 0$. Therefore, if the uncertainty can be characterized in whole or in part, it is then possible to design the input excitation to mitigate its impact by leveraging the sensitivity orthogonality. Model uncertainty characterization is hence an interesting future research direction, which can be combined with our framework to further improve estimation accuracy. In the meantime, if there is completely no knowledge of the model uncertainty, model-free methods for input design can be exploited, e.g. reinforcement learning, which does not need to explicitly know/predict the dynamics of uncertainty, but rather explore and learn through interactive experiments with the real battery. Furthermore, it is possible to use the proposed data optimization approach for estimating the model uncertainty itself as well. For example, if the uncertainty can be characterized by a model with certain unknown parameters, the method can be used to design optimal input excitation for parameterizing the uncertainty model.

Another relevant future direction is to explore data selection for estimation based on existing data. This scenario refers to the case of estimation with no data design/generation capability, e.g. online estimation based on random data stream or parameter identification from existing database. Under these circumstances, it would be interesting to look at the selection of desirable data from existing data stream/set to optimize the estimation accuracy. The idea is inspired by the results in Chapter 3, which show that it is not always the more data the better for estimation, and data with undesirable structures could degrade estimation accuracy due to uncertainties. Efforts can be made to establish the criteria for rating the data quality based on the data structures identified in Chapter 3, and formulate mechanisms for data selection that could be integrated with recursive or batch estimation algorithms.

References

[1] G. E. Blomgren, "The development and future of lithium ion batteries," *Journal of The Electrochemical Society*, vol. 164, no. 1, p. A5019, 2016.

[2] G. Pistoia, *Lithium-ion batteries.* Elsevier, 2013.

[3] G. Zubi, R. Dufo-López, M. Carvalho, and G. Pasaoglu, "The lithium-ion battery: State of the art and future perspectives," *Renewable and Sustainable Energy Reviews*, vol. 89, pp. 292–308, 2018.

[4] M. Broussely, "Lithium-ion batteries for ev, hev and other industrial applications," *Lithium Batteries*, pp. 645–685, 2009.

[5] C.-H. Chung, S. Jangra, Q. Lai, and X. Lin, "Optimization of electric vehicle charging for battery maintenance and degradation management," *IEEE Transactions on Transportation Electrification*, vol. 6, no. 3, pp. 958–969, 2020.

[6] N. Michel, A. K. Sinha, Z. Kong, and X. Lin, "Multiphysical modeling of energy dynamics for multirotor unmanned aerial vehicles," in *2019 International Conference on Unmanned Aircraft Systems (ICUAS)*, pp. 738–747, IEEE, 2019.

[7] X. Lin, Y. Kim, S. Mohan, J. B. Siegel, and A. G. Stefanopoulou, "Modeling and estimation for advanced battery management," *Annual Review of Control, Robotics, and Autonomous Systems*, vol. 2, pp. 393–426, 2019.

[8] Y. Wang, J. Tian, Z. Sun, L. Wang, R. Xu, M. Li, and Z. Chen, "A comprehensive review of battery modeling and state estimation approaches for advanced battery management systems," *Renewable and Sustainable Energy Reviews*, vol. 131, p. 110015, 2020.

[9] X. Lin, A. Stefanopoulou, P. Laskowsky, J. Freudenberg, Y. Li, and R. D. Anderson, "State of charge estimation error due to parameter mismatch in a generalized explicit lithium ion battery model," in *Dynamic Systems and Control Conference*, vol. 54754, pp. 393–400, 2011.

[10] X. Lin, Y. Kim, S. Mohan, J. B. Siegel, and A. G. Stefanopoulou, "Modeling and estimation for advanced battery management," *Annual Review of Control, Robotics, and Autonomous Systems*, vol. 2, pp. 393–426, 2019.

[11] J. C. Forman, S. J. Moura, J. L. Stein, and H. K. Fathy, "Genetic identification and fisher identifiability analysis of the doyle–fuller–newman model from experimental cycling of a lifepo4 cell," *Journal of Power Sources*, vol. 210, pp. 263–275, 2012.

[12] L. Zhang, C. Lyu, G. Hinds, L. Wang, W. Luo, J. Zheng, and K. Ma, "Parameter sensitivity analysis of cylindrical lifepo4 battery performance using multi-physics modeling," *Journal of The Electrochemical Society*, vol. 161, no. 5, p. A762, 2014.

[13] Q. Lai, S. Jangra, H. J. Ahn, G. Kim, W. T. Joe, and X. Lin, "Analytical derivation and analysis of parameter sensitivity for battery electrochemical dynamics," *Journal of Power Sources*, vol. 472, p. 228338, 2020.

[14] D. Di Domenico, A. Stefanopoulou, and G. Fiengo, "Lithium-ion battery state of charge and critical surface charge estimation using an electrochemical model-based extended kalman filter," *Journal of dynamic systems, measurement, and control*, vol. 132, no. 6, 2010.

[15] C.-H. Chen, F. B. Planella, K. O'regan, D. Gastol, W. D. Widanage, and E. Kendrick, "Development of experimental techniques for parameterization of multi-scale lithium-ion battery models," *Journal of The Electrochemical Society*, vol. 167, no. 8, p. 080534, 2020.

[16] S. Park, D. Kato, Z. Gima, R. Klein, and S. Moura, "Optimal experimental design for parameterization of an electrochemical lithium-ion battery model," *Journal of The Electrochemical Society*, vol. 165, no. 7, p. A1309, 2018.

[17] X. Lin and A. G. Stefanopoulou, "Analytic bound on accuracy of battery state and parameter estimation," *Journal of The Electrochemical Society*, vol. 162, no. 9, p. A1879, 2015.

[18] Z. Shen, L. Cao, C. D. Rahn, and C.-Y. Wang, "Least squares galvanostatic intermittent titration technique (ls-gitt) for accurate solid phase diffusivity measurement," *Journal of The Electrochemical Society*, vol. 160, no. 10, p. A1842, 2013.

[19] P. Shearing, Y. Wu, S. J. Harris, and N. Brandon, "In situ x-ray spectroscopy and imaging of battery materials," *The Electrochemical Society Interface*, vol. 20, no. 3, p. 43, 2011.

[20] S. Kim, J. Wee, K. Peters, and H.-Y. S. Huang, "Multiphysics coupling in lithium-ion batteries with reconstructed porous microstructures," *The Journal of Physical Chemistry C*, vol. 122, no. 10, pp. 5280–5290, 2018.

[21] J. Li, L. Wang, C. Lyu, H. Wang, and X. Liu, "New method for parameter estimation of an electrochemical-thermal coupling model for licoo2 battery," *Journal of Power Sources*, vol. 307, pp. 220–230, 2016.

[22] Z. Chen, C. C. Mi, Y. Fu, J. Xu, and X. Gong, "Online battery state of health estimation based on genetic algorithm for electric and hybrid vehicle applications," *Journal of Power Sources*, vol. 240, pp. 184–192, 2013.

[23] A. Malik, Z. Zhang, and R. K. Agarwal, "Extraction of battery parameters using a multi-objective genetic algorithm with a non-linear circuit model," *Journal of Power Sources*, vol. 259, pp. 76–86, 2014.

[24] Z. Khalik, M. Donkers, J. Sturm, and H. J. Bergveld, "Parameter estimation of the doyle–fuller–newman model for lithium-ion batteries by parameter normalization, grouping, and sensitivity analysis," *Journal of Power Sources*, vol. 499, p. 229901, 2021.

[25] H. Arunachalam and S. Onori, "Full homogenized macroscale model and pseudo-2-dimensional model for lithium-ion battery dynamics: comparative analysis, experimental verification and sensitivity analysis," *Journal of The Electrochemical Society*, vol. 166, no. 8, p. A1380, 2019.

[26] L. Zhang, L. Wang, G. Hinds, C. Lyu, J. Zheng, and J. Li, "Multi-objective optimization of lithium-ion battery model using genetic algorithm approach," *Journal of Power Sources*, vol. 270, pp. 367–378, 2014.

[27] N. Tian, H. Fang, J. Chen, and Y. Wang, "Nonlinear double-capacitor model for rechargeable batteries: Modeling, identification, and validation," *IEEE Transactions on Control Systems Technology*, vol. 29, no. 1, pp. 370–384, 2020.

[28] N. Tian, Y. Wang, J. Chen, and H. Fang, "One-shot parameter identification of the thevenin's model for batteries: Methods and validation," *Journal of Energy Storage*, vol. 29, p. 101282, 2020.

[29] N. Jin, D. L. Danilov, P. M. Van den Hof, and M. Donkers, "Parameter estimation of an electrochemistry-based lithium-ion battery model using a two-step procedure and a parameter sensitivity analysis," *International Journal of Energy Research*, vol. 42, no. 7, pp. 2417–2430, 2018.

[30] M. J. Rothenberger, D. J. Docimo, M. Ghanaatpishe, and H. K. Fathy, "Genetic optimization and experimental validation of a test cycle that maximizes parameter identifiability for a li-ion equivalent-circuit battery model," *Journal of Energy Storage*, vol. 4, pp. 156–166, 2015.

[31] S. Mohan, Y. Kim, and A. G. Stefanopoulou, "Estimating the power capability of li-ion batteries using informationally partitioned estimators," *IEEE Transactions on Control Systems Technology*, vol. 24, no. 5, pp. 1643–1654, 2015.

[32] X. Lin, H. E. Perez, S. Mohan, J. B. Siegel, A. G. Stefanopoulou, Y. Ding, and M. P. Castanier, "A lumped-parameter electro-thermal model for cylindrical batteries," *Journal of Power Sources*, vol. 257, pp. 1–11, 2014.

[33] Z. Song, H. Wang, J. Hou, H. F. Hofmann, and J. Sun, "Combined state and parameter estimation of lithium-ion battery with active current injection," *IEEE Transactions on Power Electronics*, vol. 35, no. 4, pp. 4439–4447, 2019.

[34] H. E. Perez, J. B. Siegel, X. Lin, A. G. Stefanopoulou, Y. Ding, and M. P. Castanier, "Parameterization and validation of an integrated electro-thermal cylindrical lfp battery model," in *Dynamic Systems and Control Conference*, vol. 45318, pp. 41–50, American Society of Mechanical Engineers, 2012.

[35] Q. Lai, H. J. Ahn, Y. Kim, Y. N. Kim, and X. Lin, "New data optimization framework for parameter estimation under uncertainties with application to lithium-ion battery," *Applied Energy*, vol. 295, p. 117034, 2021.

[36] X. Lin, “Analytic analysis of the data-dependent estimation accuracy of battery equivalent circuit dynamics,” *IEEE Control Systems Letters*, vol. 1, no. 2, pp. 304–309, 2017.

[37] X. Lin and A. G. Stefanopoulou, “Analytic bound on accuracy of battery state and parameter estimation,” *Journal of The Electrochemical Society*, vol. 162, no. 9, p. A1879, 2015.

[38] J. C. Forman, S. J. Moura, J. L. Stein, and H. K. Fathy, “Optimal experimental design for modeling battery degradation,” in *Dynamic Systems and Control Conference*, vol. 45295, pp. 309–318, American Society of Mechanical Engineers, 2012.

[39] Q. Lai, S. Jangra, H. J. Ahn, G. Kim, W. T. Joe, and X. Lin, “Analytical sensitivity analysis for battery electrochemical parameters,” in *2019 American Control Conference (ACC)*, pp. 890–896, IEEE, 2019.

[40] A. P. Schmidt, M. Bitzer, Á. W. Imre, and L. Guzzella, “Experiment-driven electrochemical modeling and systematic parameterization for a lithium-ion battery cell,” *Journal of Power Sources*, vol. 195, no. 15, pp. 5071–5080, 2010.

[41] X. Lin, “A data selection strategy for real-time estimation of battery parameters,” in *2018 Annual American Control Conference (ACC)*, pp. 2276–2281, IEEE, 2018.

[42] J. B. Fogelquist and X. Lin, “Uncertainty-aware data selection framework for parameter estimation with application to li-ion battery,” in *2022 Annual American Control Conference (ACC).* Submitted.

[43] J. C. Forman, *Minimally Invasive Characterization of Lithium Iron Phosphate Battery Electrochemical and Health Models using Fisher Information and Optimal Experimental Design.* PhD thesis, University of Michigan, 2012.

[44] A. F. Emery and A. V. Nenarokomov, “Optimal experiment design,” *Measurement Science and Technology*, vol. 9, no. 6, p. 864, 1998.

[45] A. Shahmohammadi and K. B. McAuley, “Sequential model-based a-optimal design of experiments when the fisher information matrix is noninvertible,” *Industrial & Engineering Chemistry Research*, vol. 58, no. 3, pp. 1244–1261, 2018.

[46] P. Zegers, “Fisher information properties,” *Entropy*, vol. 17, no. 7, pp. 4918–4939, 2015.

[47] D. Zachariah and P. Stoica, “Cramér-rao bound analog of bayes’ rule [lecture notes],” *IEEE Signal Processing Magazine*, vol. 32, no. 2, pp. 164–168, 2015.

[48] A. Sharma and H. K. Fathy, “Fisher identifiability analysis for a periodically-excited equivalent-circuit lithium-ion battery model,” in *2014 American control conference*, pp. 274–280, IEEE, 2014.

[49] S. Mendoza, J. Liu, P. Mishra, and H. Fathy, “On the relative contributions of bias and noise to lithium-ion battery state of charge estimation errors,” *Journal of Energy Storage*, vol. 11, pp. 86–92, 2017.

[50] M. Doyle, J. Newman, A. S. Gozdz, C. N. Schmutz, and J.-M. Tarascon, "Comparison of modeling predictions with experimental data from plastic lithium ion cells," *Journal of the Electrochemical Society*, vol. 143, no. 6, p. 1890, 1996.

[51] J. Marcicki, M. Canova, A. T. Conlisk, and G. Rizzoni, "Design and parametrization analysis of a reduced-order electrochemical model of graphite/lifepo4 cells for soc/soh estimation," *Journal of Power Sources*, vol. 237, pp. 310–324, 2013.

[52] S. J. Moura, F. B. Argomedo, R. Klein, A. Mirtabatabaei, and M. Krstic, "Battery state estimation for a single particle model with electrolyte dynamics," *IEEE Transactions on Control Systems Technology*, vol. 25, no. 2, pp. 453–468, 2016.

[53] J. C. Forman, S. Bashash, J. L. Stein, and H. K. Fathy, "Reduction of an electrochemistry-based li-ion battery model via quasi-linearization and pade approximation," *Journal of the Electrochemical Society*, vol. 158, no. 2, pp. A93–A101, 2011.

[54] J. Marcicki, M. Canova, A. T. Conlisk, and G. Rizzoni, "Design and parametrization analysis of a reduced-order electrochemical model of graphite/lifepo4 cells for soc/soh estimation," *Journal of Power Sources*, vol. 237, pp. 310–324, 2013.

[55] S. Moura, "Single particle model with electrolyte and temperature: An electrochemical battery model." `https://github.com/scott-moura/SPMeT`. Accessed: 2019-08-20.

[56] T. F. Fuller, M. Doyle, and J. Newman, "Simulation and optimization of the dual lithium ion insertion cell," *Journal of the Electrochemical Society*, vol. 141, no. 1, p. 1, 1994.

[57] S. Alavi, C. Birkl, and D. Howey, "Time-domain fitting of battery electrochemical impedance models," *Journal of Power Sources*, vol. 288, pp. 345–352, 2015.

[58] J. Song and M. Z. Bazant, "Effects of nanoparticle geometry and size distribution on diffusion impedance of battery electrodes," *Journal of The Electrochemical Society*, vol. 160, no. 1, pp. A15–A24, 2013.

[59] K. B. Hatzell, A. Sharma, and H. K. Fathy, "A survey of long-term health modeling, estimation, and control of lithium-ion batteries: Challenges and opportunities," in *2012 American Control Conference (ACC)*, pp. 584–591, IEEE, 2012.

[60] S. Jangra, "A framework for lithium-ion battery simulation and sensitivity analysis," 2019. Master thesis, University of California, Davis.

[61] H. K. Khalil and J. W. Grizzle, *Nonlinear systems*, vol. 3. Prentice hall Upper Saddle River, NJ, 2002.

[62] J. Andersson, "A general-purpose software framework for dynamic optimization," 2013. PhD thesis, KU Leuven.

[63] A. C. Hindmarsh, P. N. Brown, K. E. Grant, S. L. Lee, R. Serban, D. E. Shumaker, and C. S. Woodward, "Sundials: Suite of nonlinear and differential/algebraic equation solvers," *ACM Transactions on Mathematical Software (TOMS)*, vol. 31, no. 3, pp. 363–396, 2005.

[64] G. Fan, K. Pan, and M. Canova, "A comparison of model order reduction techniques for electrochemical characterization of lithium-ion batteries," in *2015 54th IEEE Conference on Decision and Control (CDC)*, pp. 3922–3931, IEEE, 2015.

[65] L. L. Scharf and L. T. McWhorter, "Geometry of the cramer-rao bound," *Signal Processing*, vol. 31, no. 3, pp. 301–311, 1993.

[66] X. Lin, "On the analytic accuracy of battery soc, capacity and resistance estimation," in *2016 American Control Conference (ACC)*, pp. 4006–4011, IEEE, 2016.

[67] Q. Lai, H. J. Ahn, G. Kim, W. T. Joe, and X. Lin, "Optimization of current excitation for identification of battery electrochemical parameters based on analytic sensitivity expression," in *2020 American Control Conference (ACC)*, pp. 346–351, IEEE, 2020.

[68] X. Lin, "Theoretical analysis of battery soc estimation errors under sensor bias and variance," *IEEE Transactions on Industrial Electronics*, vol. 65, no. 9, pp. 7138–7148, 2018.

[69] X. Lin, A. Stefanopoulou, P. Laskowsky, J. Freudenberg, Y. Li, and R. D. Anderson, "State of charge estimation error due to parameter mismatch in a generalized explicit lithium ion battery model," in *ASME 2011 Dynamic Systems and Control Conference and Bath/ASME Symposium on Fluid Power and Motion Control*, pp. 393–400, American Society of Mechanical Engineers Digital Collection, 2012.

[70] P. P. Mishra, M. Garg, S. Mendoza, J. Liu, C. D. Rahn, and H. K. Fathy, "How does model reduction affect lithium-ion battery state of charge estimation errors? theory and experiments," *Journal of The Electrochemical Society*, vol. 164, no. 2, p. A237, 2016.

[71] S. Park, D. Zhang, and S. Moura, "Hybrid electrochemical modeling with recurrent neural networks for li-ion batteries," in *2017 American Control Conference (ACC)*, pp. 3777–3782, IEEE, 2017.

[72] S. Yuan, H. Wu, X. Ma, and C. Yin, "Stability analysis for li-ion battery model parameters and state of charge estimation by measurement uncertainty consideration," *Energies*, vol. 8, no. 8, pp. 7729–7751, 2015.

[73] S. A. Channagiri, S. C. Nagpure, S. Babu, G. J. Noble, and R. T. Hart, "Porosity and phase fraction evolution with aging in lithium iron phosphate battery cathodes," *Journal of Power Sources*, vol. 243, pp. 750–757, 2013.

[74] R. Fu, S.-Y. Choe, V. Agubra, and J. Fergus, "Modeling of degradation effects considering side reactions for a pouch type li-ion polymer battery with carbon anode," *Journal of Power Sources*, vol. 261, pp. 120–135, 2014.

[75] A. Bartlett, J. Marcicki, S. Onori, G. Rizzoni, X. G. Yang, and T. Miller, "Electrochemical model-based state of charge and capacity estimation for a composite electrode lithium-ion battery," *IEEE Transactions on control systems technology*, vol. 24, no. 2, pp. 384–399, 2015.

[76] R. Yang, R. Xiong, W. Shen, and X. Lin, "Extreme learning machine-based thermal model for lithium-ion batteries of electric vehicles under external short circuit," *Engineering*, 2020.

[77] A. P. Schmidt, M. Bitzer, Á. W. Imre, and L. Guzzella, "Experiment-driven electrochemical modeling and systematic parameterization for a lithium-ion battery cell," *Journal of Power Sources*, vol. 195, no. 15, pp. 5071–5080, 2010.

[78] Q. Lai, W. T. Joe, G. Kim, and X. Lin, "Data optimization for parameter estimation under system uncertainties with application to li-ion battery," in *2021 American Control Conference (ACC)*, pp. 4408–4413, IEEE, 2021.